

Ion-Solid Interaction in Semiconductor Nanowires

Dissertation

zur Erlangung des akademischen Grades

doctor rerum naturalium (Dr. rer. nat.)

vorgelegt dem Rat der Physikalisch-Astronomischen Fakultät
der Friedrich-Schiller-Universität Jena

von

Diplom-Physiker Christian Michael Borschel
geboren am 19.10.1983 in Hamburg

Gutachter:

1. Prof. Dr. Carsten Ronning, Friedrich-Schiller-Universität Jena
2. Prof. Dr. Wolfhard Möller, Helmholtz-Zentrum Dresden-Rossendorf
3. PD Dr. Jan Meijer, Ruhr-Universität Bochum

Tag der Disputation: 26.01.2012

Contents

1	Introduction	3
2	Experimental Methods	8
2.1	Nanowire growth	8
2.2	Ion beam irradiation	9
2.3	Characterization	10
3	Monte Carlo Simulations	12
3.1	Motivation	12
3.2	Program description	13
3.2.1	Target definition	14
3.2.2	Ion transport simulation	14
3.3	Simulation results and discussion	18
3.3.1	Comparison to TRIM	18
3.3.2	Sputtering	18
3.3.3	Irradiation of nanowires	21
3.3.4	Sputtering of nanoparticles	22
3.3.5	Limitations of the simulation	26
3.4	Summary and conclusion	28
4	Ion Beam Induced Bending of Nanowires	30
4.1	Motivation and background	30
4.2	Irradiation experiments	33
4.2.1	Ensemble irradiation	33
4.2.2	Single nanowire irradiation	34
4.2.3	Subsequent annealing	35
4.2.4	High temperature implantation	35
4.3	Results on bending and alignment	35
4.3.1	GaAs nanowires	35
4.3.2	ZnO nanowires	38
4.4	Discussion with qualitative model	42
4.4.1	Simulations and ion beam induced defects	42
4.4.2	Bending and alignment of GaAs nanowires	45
4.4.3	Bending and alignment of ZnO nanowires	46
4.5	Impact of ion irradiation on the crystal structure and the influence of temp.	47
4.6	Dynamic bending calculations in the linear elastic regime	50

4.6.1	Modeling the nanowire	50
4.6.2	Calculation of bending	52
4.6.3	The dynamics of the bending	53
4.6.4	Bending of ZnO nanowires	54
4.6.5	Bending of GaAs nanowires	58
4.7	Summary and conclusion	61
5	Manganese Doping of GaAs Nanowires	63
5.1	Motivation - diluted magnetic semiconductors for spintronics	63
5.2	Experiments	66
5.2.1	Ion beam implantation	66
5.2.2	Post-implantation annealing	68
5.2.3	Implantation at elevated temperatures	68
5.3	Results and discussion	69
5.3.1	Room temperature implantation	69
5.3.2	Subsequent annealing	71
5.3.3	Implantation at elevated temperatures	74
5.4	Magnetotransport properties	77
5.4.1	Sample preparation and measurements	77
5.4.2	Results and discussion	77
5.5	Summary and outlook	80
6	Summary and Conclusion	82
	Bibliography	87
A	List of Publications	99
B	Details Regarding The MC Simulations	101
B.1	The database method for scattering angles	101
B.2	Computing flow of ion transport	102
B.3	Additional comparisons between iradina and TRIM	104
B.4	Distribution of single ion sputter yields	105
C	Details for the dynamic bending calculation	106

Chapter 1

Introduction

When shrinking down material from macroscopic (bulk) toward microscopic scales, the properties of the material will begin to deviate from bulk properties at some size before the scale of single atoms is reached. Typically, this happens at length scales from a few nanometers to several 100 nanometers, resulting in the term “nano” to describe structures at this mesoscopic length scale. The properties of such nanosized materials or nanostructures can differ quite strongly from the respective bulk properties; for example these can be different elastic constants [Che07a, Die11], optical [Flo11] as well as electrical [Wan09] properties and also thermal properties as for instance lower melting points [Gui07]. Furthermore, new effects occur in nanostructures, which can be due to quantization [Naw10], reduced dimensionality [Che07b] or the large surface-to-volume ratio [Sti07]. On the one hand, these aspects have to be accounted for in the on-going miniaturization of conventional devices and technology. On the other hand these different properties and new effects also allow completely new device concepts and applications beyond “simply being smaller”.

One class of nanosized materials are *nanowires* (NWs). These have an approximate shape of a long cylinder and are thus reduced in two dimensions but not in the third dimension. Typical diameters range from a few to several hundred nanometers. Very thin nanowires can appear quasi one-dimensional for electrons or show quantum confinement effects, while thicker nanowires appear as bulk material toward electrons. Nevertheless, also these somewhat thicker nanowires exhibit a very large surface-to-volume ratio compared to bulk material, and they can strongly confine visible light when their diameter is comparable to the wave length. The large surface-to-volume ratio as well as the confinement can be utilized, leading to a number of different nanowire based devices that have been demonstrated. In these devices, the nanowires (usually consisting of some semiconductor material) can act as the functional element as well as the electric or optic wire to access the device.

Examples are nanowire field effect transistors (FETs) [Cui03b], where the NWs constitute the channel and can for instance be wrapped with an all-around gate [Tan10]; nanowire based solar cells [Weh08, Pet09, Hoc10], where the absorption is largely increased over bulk material; or nanowire FET based sensors [Yeh09], where the large surface-to-volume ratio is made use of. Nanowires can further be used for light emission or photonic applications [Aga06, Wil09], for instance as nanowire LEDs [Yan08], where the NWs act as electrical wire, light emitter and waveguide for the light [Vos07]; as nanowire lasers [Joh03, Aga05, Hua07, Zim08, Gar09, Zim10], where the nanowires form the cavity/resonator as well as the active laser medium; or as ultra-small/extremely confined light sources, where the light is actually not guided within the nanowire itself, but in an extremely small volume between the nanowire and the substrate [Oul08].

One big advantage of nanowires is that they can be produced in large numbers in parallel using self-organized growth (“bottom-up”), which means that they do not need to be “carved out” from bulk material (which would be called “top-down”) [Cui03a]. There exists a variety of chemical and physical growth methods to create nanowires of different semiconductor materials, ranging from growth in solution [Zha00], vapor transport [Bor06] and metal-organic vapor phase epitaxy (MOVPE) [Mik04, Gut09] to molecular beam epitaxy (MBE) [Ihn07]. A widely employed growth mechanism is the vapor-liquid-solid growth [Wag64], which will be explained later in section 2.1.

A further advantage during nanowire growth is their small footprint, which allows growing nanowires of one semiconductor material heteroepitaxially on a wafer of another semiconductor material: while lattice mismatch causes stress and fracture in heteroepitaxial thin film growth, such stress can quickly relax laterally in nanowires, allowing growth with very high crystal quality [Man06].

Apart from the advantages and useful properties of nanowires, they also pose several problems regarding applications. The most important property for the technological success of semiconductors is the possibility to adjust their properties by doping; however, doping is a major obstacle for semiconductor nanowires because the chemistry and complex microscopic physical processes at work in the growth process make doping during growth very difficult. Dopants may segregate in secondary phases [Sad07], may accumulate at the surface [Xie09] or may disrupt the growth and cause morphological changes [Wha07]. If incorporation of dopants is possible, it is often difficult to control the exact amount; only for a few materials and dopants, successful and controlled doping during growth has been achieved [Li07, Cao08, Gut09]. Another problem

for a number of nanowire based devices (FETs, sensors, lasers) is that great effort or many processing steps are required to manipulate a single nanowire and to create a single functional device from a nanowire.

Doping by ion implantation or simply “ion beam doping” is a widely used technique to dope semiconductor materials [Zie92]. As a hyperthermal doping method, ion beam doping is not bound by solubility limits and in principle any element can be ionized, accelerated and implanted into any target. The dopant concentration and the implantation depth can be well controlled via the ion fluence and the ion energy, and furthermore, homogeneous doping of wafer scale targets is possible. The most important drawback of ion beam implantation is the high concentration of defects created by the ions, making post-implantation annealing a necessity. Nevertheless, appropriate annealing techniques have been developed for most semiconductor materials and ion beam doping has been widely used in industry for decades.

In combination with nanostructures, ion beams have not only been used for doping [Ell08], but also for manipulation (e.g. the “ion hammering” effect [Sno00]) or even production of nanostructures, for example nanoscale pattern formation on surfaces (“ripples”, [Hab99]), or “carving” of nanostructures using focused ion beams [Ink04], or ion-beam induced nanostructure growth [Ell08, Bet09], see also the reviews [Dha07, Kra10].

Specifically concerning nanowires, ion beam implantation can address both problems mentioned earlier (doping and manipulation): first, it can be used to force dopants into the nanowires after growth, independent of the growth method, and second, as a wafer-scale method it allows to manipulate large numbers of nanowires simultaneously. Doping of nanowires by ion beam implantation has been achieved in recent years for several nanowire materials [Col08, Ron10a, Ron10b, DK11] and for electrically [Sti08b], optically [Geb08b], as well as magnetically [Zha09] active dopants. Furthermore, pn-junctions created by ion beam doping of nanowires were reported [Hof09, Kan10].

Despite the advantages of ion beam doping, several new problems arise when implanting ions into semiconductor nanostructures compared to implantation into bulk material: an important issue are the lower melting points of nanostructures [Gui07] prohibiting direct adoption of established annealing methods from bulk materials. Furthermore, the heat introduced into the target by the ion beam is dissipated much slower in some nanostructures than in bulk, giving rise to different thermal conditions during implantation. In some cases, ion beams are observed to drive changes in structure and morphology of nanostructures, not known from bulk

irradiation. Additionally, it is more difficult to calculate the concentrations of implanted ions and ion beam induced damage in nanostructures. The reason is that conventional simulation codes for ion beam irradiation can only take into account flat or bulk targets, which may pose severe problems: for example, ions can leave nanostructured targets laterally and not contribute to doping, which frequently leads to overestimation of doping concentrations in ion beam implanted nanostructures.

This thesis reports three approaches, which address – from different points of view – several of the issues raised above; in particular how the ions interact with nanostructures as compared to bulk, the influence of ion beam implantation on the structure and morphology of nanowires, how damage created during ion beam doping of nanowires can be annealed or avoided and how ion beam implantation into nanostructures can be simulated. Detailed motivations for each approach are provided at the beginnings of the respective chapters:

(i) Simulating ion beam irradiation of nanostructures:

In the scope of this thesis, a Monte Carlo ion beam simulation program called *iradina* (**ion range and damage in nanostructures**) was developed. The transport of the ions through the solid works in principle similar to other conventional Monte Carlo ion beam simulations programs employing a binary collision model. However, the flexible three dimensional target definition allows accurate representation of nanostructured targets, and the use of fast look-up algorithms allows reduction of calculation times by up to two orders of magnitude. The program is described in detail in chapter 3.

(ii) Ion beam induced bending of nanowires:

In chapter 4, the ion beam induced bending and alignment of semiconductor nanowires is discussed. Experimental results are presented for the irradiation of ZnO and GaAs nanowires. Irradiations of single nanowires as well as “ensembles” of nanowires are investigated. A basic (qualitative) model for the bending is presented in section 4.4, showing that defect production by the ion beam is the key mechanism. For a better and more quantitative understanding of the bending dynamics, a linear elastic nanowire model was developed, which is described in section 4.6. In combination with the ion beam simulation program *iradina* it allows *dynamic* simulations of the bending of nanowires under ion beam irradiation.

(iii) Ion beam doping of nanowires:

Diluted magnetic semiconductors (DMS) are interesting materials in order to control the spin-polarization of electrons, which is necessary for prospective spintronic devices. One such DMS material is highly Mn doped GaAs, which can be grown as a thin film by low temperature MBE [Ohn96]. When one wants to create highly Mn doped GaAs nanowires however, it turns out that incorporation of sufficient Mn during growth of the GaAs nanowires is not possible due to the low solubility of Mn. A possible solution to this problem is ion beam implantation of as-grown GaAs nanowires with Mn, which is discussed in chapter 5.

Chapter 2

Experimental Methods

2.1 Nanowire growth

As mentioned in the introduction, a variety of growth methods is available for semiconductor nanowires, where the most suitable depends on the desired nanowire material. Nanowires are often grown via the so-called vapor-liquid-solid (VLS) mechanism first described by Ellis and Wagner in 1964 [Wag64]: In order to grow wires of material B , a catalyst material A is needed, which has a lower melting point than B and which forms an eutectic system with B . The catalytic particles of material A (typically gold) with diameters in the range of the desired wire diameter are deposited onto a substrate. The substrate is heated to a temperature between the two melting points of A and B . The catalyst particles become liquid droplets. The material B is provided from the vapor phase, absorbed at the droplet surface and dissolved in the liquid droplet. The concentration of B within the droplet increases, until the droplet becomes saturated and B starts to segregate. In most cases, this happens at the interface of substrate and droplet. Providing more of material B in the vapor phase leads to further absorption and further segregation at the interface: a wire with the diameter of the particle grows and lifts up the droplet. The solid-phase solubility¹ of A in B is usually very low and hardly any catalyst is incorporated in the growing wire. This simple model does not fully explain growth of compound semiconductor nanowires, where ternary phase diagrams must be taken into account [Bor06]. Furthermore, generalizations of this growth model have been discussed in the literature [Wac09].

In the scope of this work, semiconductor nanowires consisting of ZnO and GaAs were investigated. Growth of ZnO nanowires was performed at the IFK/Jena within a horizontal tube furnace. As the source material, ZnO powder is evaporated at 1350 °C and transported with

¹“Randlöslichkeit”

an argon gas flow to the substrates covered with gold particles, where the ZnO nanowires grow at temperatures between 1000 °C and 1200 °C. Depending on the substrate, the nanowires grow in random direction on Si (covered with SiO₂), or homo-epitaxially on single crystalline ZnO, or hetero-epitaxially on AlN. Nanowires mostly grow in c-direction of ZnO. The influence of the various growth parameters (temperature, pressure, transport gas flow, etc. ...) and their optimum values have been discussed in detail in several previous theses and publications [Sti05, Mü105, Bor06, Koz09, Gna10, Mil10, Spi11]. Growth of GaAs nanowires was performed at the Lund Nano Lab (Sweden)², and at the Institute for Semiconductor Technology, University of Duisburg-Essen³, in both cases using metal-organic vapor phase epitaxy (MOVPE). Arsine and trimethylgallium are used as sources and are transported by an H₂ or N₂ carrier gas to GaAs substrates covered with Au particles. At ≈ 450 °C, the nanowires grow homo-epitaxially in [111]-direction, details in [Bor04, Mik04, Gut09].

2.2 Ion beam irradiation

In order to irradiate samples with energetic ions, an ion source and an ion accelerator are required. Depending on the desired ion species, the source material can be gaseous, or the source material may be in a condensed state. The first case allows simple ionization using electrons or a discharge process, while in the second case, the material must be evaporated or sputtered and then ionized.

The ions are usually extracted from the source by a defined extraction voltage, then pre-accelerated by a static electric field and mass-separated for example by a magnetic dipole field. Finally, the selected ions are accelerated to the desired energy. This can be performed with static electric fields for energies up to a few MeV. In a tandem accelerator, the electric potential is used twice (or more often) by changing the ion charge from negative to positive using an electron stripper after half the acceleration distance [Wit88].

Two types of ion beam accelerators were used in the scope of this work. The first one is the general purpose implanter ROMEO of the IFK/Jena. Almost all chemical elements are available as ion species and the energy can be selected between 10 keV and 380 keV. The

²see <http://www.nano.lth.se/lundnanolab>, NWs were grown by Magnus Borgström and Jesper Wallentin from the group of Lars Samuelson.

³Growth of GaAs NWs in Duisburg was performed by Christoph Gutsche and Ingo Regolin from the group of Werner Prost and Franz-Josef Tegude.

implanter provides an unfocused broad beam, which can be used to irradiate areas of several cm^2 . The targets can be heated to several hundred $^\circ\text{C}$.

The other type are Focused Ion Beam (FIB) systems. They provide an ion beam, which can be focused down to a few nm; but the energy as well as the choice of ion species is limited. The reason is that the ion source must be small to obtain a good focus, thus, special sources are required: typically, a “liquid metal ion source” (LMIS) is used, where a liquid metal wets an ultrasharp tungsten tip (radius ≈ 2 nm). A high electric field at the tip ($> 10^8$ V/m) ionizes metal atoms which are then extracted and accelerated. Most proprietary systems only provide Ga^+ ions. The big advantages of the FIB are (a) that the ion beam has a small focus (few nm) and can be scanned or set to defined positions on the sample with nm resolution, and (b) setups often combine a FIB with a SEM (see section 2.3), which allows *in-situ* imaging and characterization with electrons. In the scope of this work, two machines were used: a Tescan Lyra XMU including a SEM column with a thermal tungsten source and a FEI DualBeam FIB Helios Nanolab 600i including an electron column with a field emission gun for high resolution SEM imaging. Both machines are limited to an ion energy of 30 keV and the use of Ga^+ ions.

2.3 Characterization

Characterization of nanostructures requires techniques with resolutions beyond optical microscopy. Imaging of the structures is typically done using scanning electron microscopes (SEM): A focused electron beam is scanned over the sample, a type of sample response (for example backscattered electrons) is detected and the intensity of that signal is plotted as a function of scanning location on the sample. Due to the small DeBroglie wavelengths of energetic electrons (30 keV), the electron beam can be focused down below a nm; however, the imaging resolution is not only limited by the beam focus, but also by the lateral extension of the sample’s response function. Other responses than secondary electrons can be detected, for example backscattered electrons, electron beam induced current (EBIC), X-rays, cathodoluminescence (CL) The energy of X-rays can be analyzed to obtain information on chemical composition in the sample via characteristic X-ray emission (energy dispersive X-ray spectroscopy, EDX). More details can be found in [Rei98].

In the scope of this work, a Jeol JSM 6490 with a thermal LaB_6 electron gun and equipped with EDX and CL (imaging and spectroscopy) was used, as well as the field emission SEM column of the FEI DualBeam FIB.

Imaging with sub-nm resolution and structural analysis of nanostructures can be performed with a transmission electron microscope (TEM). Here, the image is not created by scanning; instead, a parallel electron beam with higher energy (for example 300 keV) illuminates the sample. There are various possibilities how images are created in the TEM and different mechanisms generate contrast. Very short and simplified explanations of the most used imaging modes follow, details can be found in relevant text books [Wil96, Ful08]. In the bright field (BF) mode the image is mainly formed by transmitted, non-scattered electrons and contrast is achieved by occlusion and absorption of electrons by the sample (“mass-thickness contrast”). The image is projected and enlarged to a screen or to a CCD camera for recording. In dark field (DF) mode, the image is formed only by electrons diffracted to a certain direction and structures that diffract into that particular direction appear bright (“diffraction contrast”). High resolution TEM images (HR-TEM), where single columns of atoms become visible, are achieved by phase contrast imaging: an interference pattern of transmitted (non-diffracted, forward-scattered) electron reference wave and diffracted electron wave forms the image. The crystallinity can be analyzed from Fourier transformations (FFT, “fast Fourier transform”) of these HR-TEM images. Furthermore, electron diffraction patterns (DPs) can be recorded in the TEM, which allow conclusions on the crystal structure. These DPs can also be recorded of confined areas of the sample (SAED, “selected area electron diffraction”). Apart from imaging and recording diffraction patterns, the electron beam can be focused to specific points on the sample and the emitted X-rays can be analyzed (EDX), allowing elemental characterization with high spatial resolution. For this work, TEM images were recorded with a Jeol JEM 3010 (IMT/Jena) or in some cases with a Jeol JEM 3000F by Dr. Maria Messing at Lund University, Sweden. Since samples must be very thin to allow electron transmission (typically < 100 nm), preparation of TEM specimen from bulk or thin films is not trivial. However, the preparation of nanowires for the TEM is rather simple, because they are usually thin enough to allow sufficient transmission of electrons. The nanowires are transferred to a copper mesh covered with an ultrathin carbon foil by pressing the mesh face down onto the nanowire growth substrate. The mesh can then be mounted in the TEM.

Chapter 3

Monte Carlo Simulations

A Monte Carlo code for the simulation of ion beam irradiation of nanostructures was developed within the scope of this thesis. Parts of this chapter are published in [Bor11b]; however, the code has been improved since then and the current version is described here. The latest version of the source code and a user manual are available from the internet¹.

3.1 Motivation

Ion beam irradiation experiments are often accompanied by computer simulations of the experiment, because from these simulations it is possible to determine the distribution of the implanted ions as well as the ion beam induced damage in the target material. These simulations are frequently done using Monte Carlo (MC) codes and a number of different MC programs have been presented and successfully applied in the past decades [Bie80, Möl84, Hau84, Pos86, Möl88, Hob95, Lee95, Ber97]; one of the most widely used being TRIM [Zie85, Zie11]. These TRIM-like codes usually represent the target by a number of flat layers, where each layer consists of a homogeneous material. It is possible to obtain a three-dimensional distribution of implanted ions, but still the target is always flat and layered. Thus, the irradiation of nanostructures cannot be accurately simulated. A few specialized TRIM-like Monte Carlo codes have been used, which can take into account the full 3d geometry, but these codes are specialized for their respective applications and are not widely available [Sch09b, Bor09].

There exist several advanced MC codes intended and optimized to simulate the ion implantation of semiconductor devices, for example MCIMPL [Hob89] or TOMCAT [Li01]. These codes can take into account 3d target geometries and additionally effects like channeling. They

¹<http://www.iradina.de>

employ advanced techniques to save computation time, e.g. trajectory replication, spatial octree division [Sti93, Obr98] or convolution of point response functions [Bur99].

There exists another group of programs which are optimized to calculate the evolution of a target surface in FIB-milling [Box01, Kim07, Kun10, Hob11]. These codes can simulate sputtering effects for non-flat targets and they take into account effects like redeposition of sputtered atoms. However, these “FIB-codes” focus on the evolution of the target surface, which they represent as a height value for each lateral position. Additionally, they are optimized for the high fluencies, where sputtering is the dominant process. They are not suitable to obtain distribution of implanted ions and implantation damage in nanostructures.

Ion beam irradiation of nanostructures can also be done by molecular dynamic (MD) simulations, which attempt to solve the equations of motion for the ion and all atoms within in target, thus avoiding a number of simplifying approximations made in the MC approaches. However, MD simulations require computation times orders of magnitude larger than MC simulations making these MD simulations far too time-consuming for simulation of nanostructures larger than a few tens of nm and with more than a few 100 ions [Jär08, Hoi11].

In order to simulate the ion irradiation of nanostructures, it would be desirable to have a relatively simple and fast MC code similar to TRIM, but which can accurately represent nanostructured targets and thus bridge this gap between the “non-3D” TRIM-like MC codes, the comparatively complex semiconductor device codes, the high fluence “FIB-sputter-codes” and the MD codes. For this reason, a new MC code named *iradina* (**i**on **r**ange and **d**amage in **n**anostructures) was developed in the scope of this thesis. It should be noted that a version of TRIDYN supporting 3d target geometry is currently being developed [Möl11].

3.2 Program description

Irادina simulates the ion beam irradiation of a target by letting a large number of ions impinge subsequently on the target and following each ion’s path in detail through the target material by means of a MC transport algorithm. It works similar to other MC programs like TRIM, but with a different target definition. Some calculation routines are adapted from the open source simulation code *corteo* published by F. Schiettekatte [Sch07, Sch08]. The purpose of *corteo* is different from *irادina*, as it is intended for the simulation of ion beam analysis spectra. Nevertheless, it uses a MC transport algorithm and provides some very fast functions to calculate scattering angles and stopping powers, which are useful for *irادina* as well.

3.2.1 Target definition

In *iradina*, the simulation volume is a rectangular box with arbitrary dimensions. The box is divided into a possibly large number of equal-sized rectangular cells. The number of cells and the cell size can be defined independently for each direction. A list of materials that are present in the target is defined. Each material can contain different elements and for each element a lattice binding energy E_b , a displacement energy E_D and a surface binding energy E_S must be defined. Each cell contains one of the defined materials, or alternatively no material at all, setting it to vacuum. By selecting appropriate cell sizes and materials, almost any three-dimensional structure can be approximated.

The cell size and contents remain constant throughout the complete simulation, which makes *iradina* a static MC code. No dynamic composition variations are possible in the current implementation.

Periodic boundary conditions (PBC) can be defined in any of the three spatial directions, allowing to simulate irradiation of periodic structures. Furthermore, PBC often allow to reduce the simulation volume for large targets, if the target exhibits translational symmetry.

3.2.2 Ion transport simulation

Very detailed discussions of MC ion transport can be found in various textbooks [Zie85,Eck91,Sch07]. A more compact description will be given here, not discussing each point in detail. A simplified schematic flow-chart of the transport algorithm is illustrated in appendix B.2.

The basic idea of the transport algorithm is to follow a projectile through the material in small steps, where each step corresponds to a collision with a target nucleus, until the projectile has lost all its energy or left the target. The projectile is assumed to interact with only one target nucleus at a time, which is known as the binary collision approximation (BCA). Several random numbers are used in each step which account for the name “Monte Carlo” code².

At any moment, a projectile is described by its momentary position in space, by its velocity vector (reduced to unit length) and its kinetic energy. Each step begins with the “free path”: the projectile is assumed to proceed on a straight line before it collides with a target nucleus. Along this straight line, the projectile loses energy due to a constant non-local electronic stopping. The values for electronic stopping are obtained from tables calculated with the SRIM package

²Conventional computers actually cannot generate true random numbers, because they are deterministic machines (although they may sometimes appear to do random things). *Irada* uses the same pseudo random number generator (PRNG) as *corteo*, suggested by L’Ecuyer [L’E88].

(`SRModule.exe`, see [Zie11]) and the fast table-look-up function from *corteo* is used for this purpose. Electronic energy loss straggling is taken into account by randomly varying the electronic stopping. The straggling values are calculated using the empirical formulas proposed by Yang *et al.* [Yan91]. The length of the free path l is selected randomly according to a poisson distribution with the mean free path corresponding to the interatomic distance. Alternatively, the free path can be constant and set to the interatomic distance. TRIM-like programs can employ much longer path lengths to save computation time. This approximation, which saves a lot of time for high energy ions, is not made in *iradina*. First, this is not very useful for small nanostructures and second, on modern fast computers and with the fast calculation routines from *corteo*, it is not necessary. Furthermore, short path lengths simplify the calculation of electronic stopping: when using long path lengths as in TRIM, one must check if the material has changed along the path and one must correct electronic stopping accordingly. But when path lengths are comparable with inter-atomic distances, this correction can be neglected.

Next, an impact parameter is selected for the collision happening at the end of the free path. The maximum impact parameter p_{\max} is related to the free path l in such a way that a cylinder of length l and radius p_{\max} contains on average one target atom. This ensures an appropriate frequency of collisions to occur. The actual impact parameter p is selected randomly between 0 and p_{\max} with a square distribution, details in [Sch07]. In addition to the impact parameter, the azimuthal angle ϕ is required in order to determine the direction into which the projectile is scattered (and to determine the exact position of the target nucleus). This azimuthal angle is selected randomly between 0 and 2π . The random selection of target nuclei positions account for the so-called random phase approximation (RPA). Thus, subsequent collisions are not correlated at all, rendering these kind of MC codes unable to simulate ion beam irradiation along channeling directions in crystalline targets. In case the material at the target position contains different elements, the collision partner of the projectile is randomly selected according to the stoichiometry.

The collision itself involves the calculation of the energy transfer from the projectile to the target nucleus and the deflection of the projectile. These can be calculated knowing the interaction potential, the projectile energy and the impact parameter. The universal potential proposed by Ziegler, Biersack and Littmark is used [Zie85]. The so-called “scattering integral”, from which the scattering angle is calculated, cannot be solved analytically for the universal potential. One way to avoid the lengthy numerical calculation is to use the so-called MAGIC algorithm [Bie80], which is employed by TRIM and related programs. Even faster is the use of a database with

precalculated scattering angles and a neat indexing mechanism to access the entries, which was proposed by Yuan *et al.* [Yua93]. The scattering angles as a function of reduced energy and reduced impact parameter are stored in a large two-dimensional logarithmically scaled table. *Iradina* uses the database from *corteo*, which is explained in detail in [Sch07], see also appendix B.1.

To simulate the collision, the velocity unit vector of the projectile is rotated according to the scattering angle and the azimuthal angle. The energy transfer T to the target nucleus is calculated from conservation of momentum and energy, and T is subtracted from the projectile's kinetic energy. Then the projectile can proceed to the next step.

It is important to consider also the fate of the target nucleus, in order to calculate the ion beam induced damage. If the target nucleus gains more energy than its displacement energy E_D , it is permanently displaced from its lattice site, leaves a vacancy behind and becomes itself a moving projectile in the target. (Recoils gaining less than E_D must be considered as well, details follow below). The transport of such a recoil is simulated with the same function as for the ion, using recursive function calls. This way, a complete collision cascade can be simulated. A special case considers “replacement collisions”: when projectile and recoil are of the same type, and the projectile loses so much energy to the recoil that its remaining kinetic energy is below E_D , then the projectile is assumed to *replace* the recoil on its lattice site. In that case, no vacancy is created.

In order to record the ion induced damage, each cell of the simulation volume has a number of counters for the various type of defects (vacancies, displacements, interstitials, replacements, atoms sputtered from this cell). Separate counters are defined for each material and each element. Whenever a displacement or replacement occurs or when a projectile stops, the respective counters are increased. Counters also exist for primary ions that have stopped. Finally, the distribution of all types of damage as well as the distribution of implanted ions can be extracted from these counters.

In order to appropriately calculate sputtering, some more details must be taken into account during the simulation. The surface binding energy E_S is the important quantity here: when a projectile attempts to move from a cell with material to a cell with vacuum, it must overcome this energy barrier. When moving from vacuum to material, it gains E_S . The surface binding energy acts in direction perpendicular to the surface; thus, if the projectile velocity is not perpendicular to the surface, the velocity vector needs to be adjusted (surface refraction).

Furthermore, the displacement of recoils must be treated differently: if a target nucleus gains less than its displacement energy, it does not mean that it does not move at all. It just means that in the end it will usually be placed at its original site with a high probability. But in between, it may transfer energy to other target atoms, or it may leave the solid and become a sputtered atom. This issue is quite important, considering that typical displacement energies are in the order of 10 to 25 eV, while typical surface binding energies are in the order of 1 to 5 eV. To account for this effect in the simulation, recoils are assumed to be displaced and become moving recoils even if their energy is below E_D . However, in that case the recoil is marked as a “sub-threshold” particle and when it has lost all its energy it is placed back to its original site, not creating a vacancy and interstitial. A further issue important for sputtering is interaction of a projectile moving in vacuum with close-by material. If the projectile is less than a few mean atomic distances away from material, it may still be scattered in a collision and it may transfer energy to target atoms which can then be sputtered. Thus, even if the projectile is moving in vacuum, a possible target atom position is calculated in each step and if this target position is inside a cell with material, then a collision is assumed to happen. It is not sufficient to take into account collisions only within a cylinder of radius p_{\max} , because small energy transfers can also be important for sputtering. Thus, target atom positions are also searched for in ring cylinders with radii between $\sqrt{n} \cdot p_{\max}$ and $\sqrt{n+1} \cdot p_{\max}$ with $n = 1, 2, 3$; details in [Eck91, p.92ff].

Taking into account the above mentioned effects requires quite some calculation time. In case the sputter yields are not of interest, some calculations can be skipped. Therefore, an alternative faster variant of the transport algorithm is also implemented in *iradina*. This simplified algorithm is more similar to the transport algorithm of the *corteo* code and mainly uses the following approximations: (1) When the projectile is in vacuum, no interaction with nearby material is considered. (2) Additional target atoms in ring cylinders are not taken into account. (3) The recoils are assumed to start exactly from the point where the projectile changes its direction (and not one impact parameter away). (4) Surface refraction is neglected. These simplifications make the calculations about four to five times faster. The resulting distributions of implanted ions and of displacement events are almost the same as for the non-simplified (“full”) transport algorithm, a comparison follows below.

3.3 Simulation results and discussion

3.3.1 Comparison to TRIM

Comparisons between simulation results obtained from *iradina* and from TRIM were made. Since *iradina* works similar to TRIM, the results should be comparable and can serve as a basic test for correct functionality of the code. Figure 3.1 shows simulation results for Ar irradiation of bulk Si (perpendicular incidence). The distribution of implanted ions as a function of depth and as a function of lateral offset from entry point is shown for three different energies. Close agreement between (both algorithms of) *iradina* and TRIM is achieved in all three cases. The ion beam induced damage resulting from the simulations is illustrated in figure 3.2, which shows the displacement events as a function of depth. The results from *iradina* and TRIM are mostly in good agreement as well.³

In order to verify functionality of *iradina* over a larger range of ion masses, further comparisons were made with different ions (H, N, Ag and Pb), each with 10, 100, and 1000 keV (results illustrated in appendix B.3). The results from *iradina* and TRIM are in good agreement for most cases. For hydrogen ions, the TRIM simulations yield slightly sharper distributions of implanted ions than *iradina*. Problems with the hydrogen implantation profiles also occurred in *corteo* and may be caused by the universal potential used to calculate the scattering angles [Sch10].

3.3.2 Sputtering

An interesting application for simulating ion beam irradiation of nanostructures is the calculation of sputter yields. The sputter yields of nanostructures can strongly differ from bulk values, especially when the size of the collision cascade becomes comparable to the size of the nanostructure itself. The rectangular target structure used in *iradina* poses a problem for sputtering: as illustrated in figure 3.3(a), surfaces inclined to the rectangular grid become stepped in the simulation. Their effective surface area is thus enhanced, which may increase sputtering.

³A minor deviation occurs here: in the *iradina* results, the fraction of *replacement* events is about 30% of all displacements, which is in agreement with the SRIM manual, see [Zie11]. But in contrast, the TRIM program finds a replacement fraction of only about 10%. As it is not known how exactly TRIM calculates the replacements and the source code of TRIM is not available to the author of this thesis, the reason for this discrepancy could not be determined. In any case, the method to use the displacement energy as a sharp cut-off to calculate the replacement fraction is a very simple model, that cannot be expected to yield very accurate results compared with experiments. This error further does not influence the shape of the distribution of damage but only its amplitude. The amplitude of damage obtained from MC simulations is not very accurate anyway, as a number of point defects anneal out during implantation (“dynamic annealing”). Thus, this discrepancy is not assumed to have any severe effect.

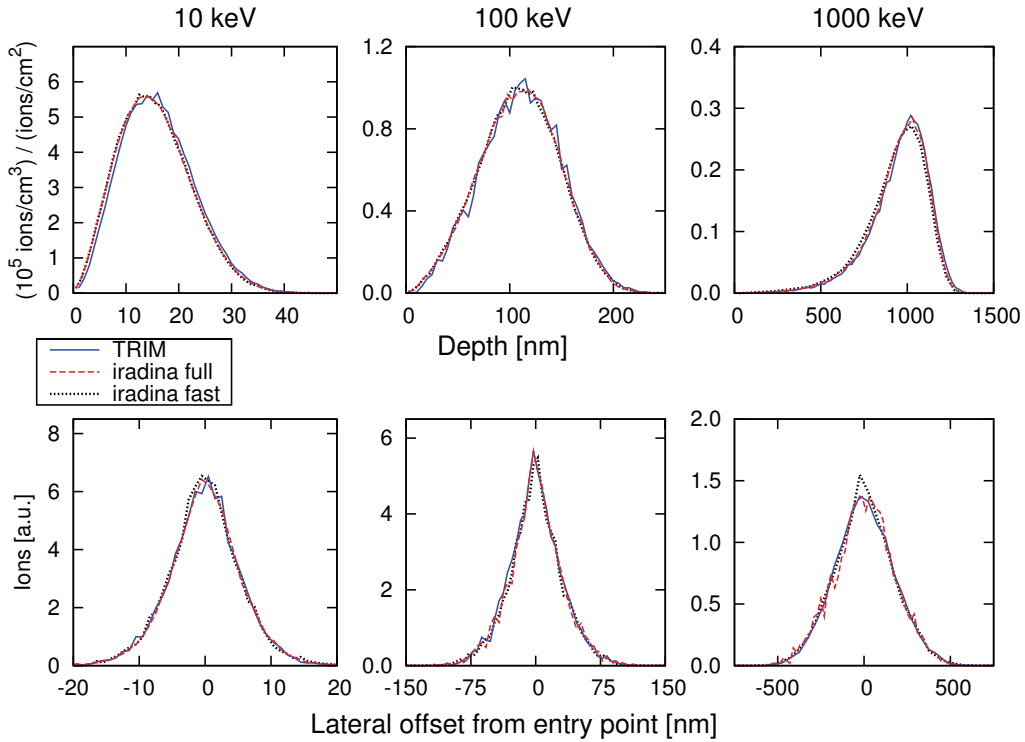


Figure 3.1: Simulation results from iradina (full and fast algorithm) and TRIM (SRIM 2008.03) for Ar implantation into bulk Si. The top row shows depth distribution of implanted ions for three different energies, the bottom row shows the lateral distribution for the respective energies.

Additionally, sputtered particles may re-enter the solid material and cause extra damage and sputtering. Furthermore, the local angles of incidence are affected by the rectangular grid. In order to determine the magnitude of this problem, simulations were made for irradiation of bulk Si with 5 keV Ar ions using different angles between surface plane and grid axes (but with the ion beam always being perpendicular to the plane). The resulting sputter yields are plotted in figure 3.3(b). When a cell size of 10 nm is selected, the sputter yield increases almost by a factor of 2, when the angle changes from 0° to 45° , showing the significant error caused by using a rectangular grid. One way to circumvent this problem is to reduce the cell size to very small values as shown in 3.3(b). At 5 nm cell size, the sputter yield still changes, but at 1 nm cell size, almost no influence on the sputter yield occurs. The reason is that when the cell size is in the same order of magnitude as the flight length of the projectile, then the surface effectively becomes smooth. This observation is also in agreement with sputter simulations made with the 3d version of TRIDYN, which is currently being developed [Möl11]. On the other hand, the drawback of using very small cell sizes is that the total number of cells may become very large – especially in 3d targets. Since each cell requires a few counters for all the different types of defects, this can result in huge requirements for memory.

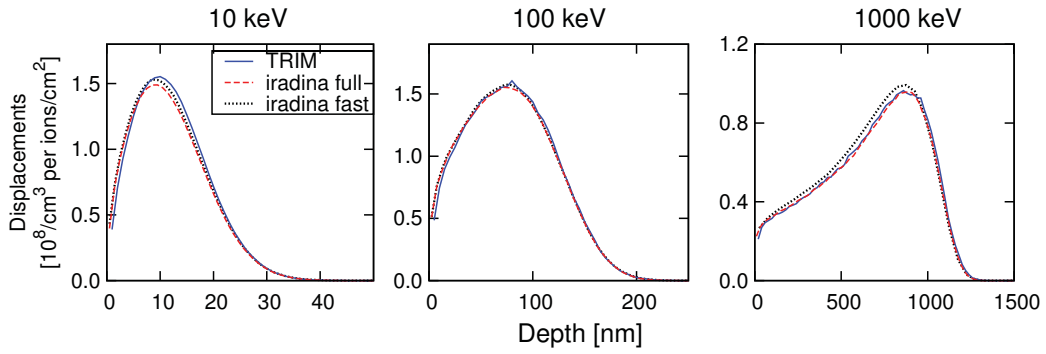


Figure 3.2: Simulation results from iradina (full and fast) and TRIM (SRIM 2008.03) for Ar implantation into bulk Si. The displacement events are shown as a function of depth for three different Ar energies.

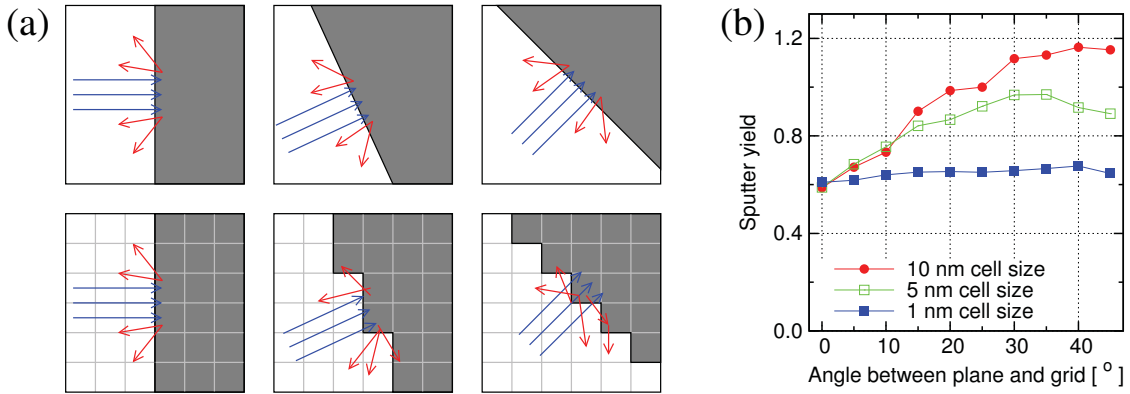


Figure 3.3: Problem of sputtering at surfaces inclined to the rectangular grid. (a) Top row: in reality, the sputter yield is of course always the same, as long as the ion beam is perpendicular to the surface. Bottom row: In the simulation, the sputtering details depend on the angle between surface and rectangular grid. Blue: ions, red: sputtered particles. (b) Simulated sputter yields (5 keV Ar ions on silicon target) as a function of angle between surface plane and grid for different cell sizes.

Therefore, another solution to this problem is implemented in *iradina* for nanostructures of simple geometry: for example nanoparticles or nanowires can easily be described analytically by spheres or cylinders, respectively. *Irادina* uses the analytical formula to decide whether a given position is inside or outside the nanostructure, meaning whether there is material or vacuum at a possible location of a target nucleus. Nevertheless, for counting damage and implanted ions, the rectangular cell geometry is kept. This combination allows on the one hand to accurately represent smooth surfaces, but on the other hand to maintain the simplicity of a rectangular geometry. Thus, only little changes of the code are required to incorporate accurate description of nanosized spheres or cylinders.

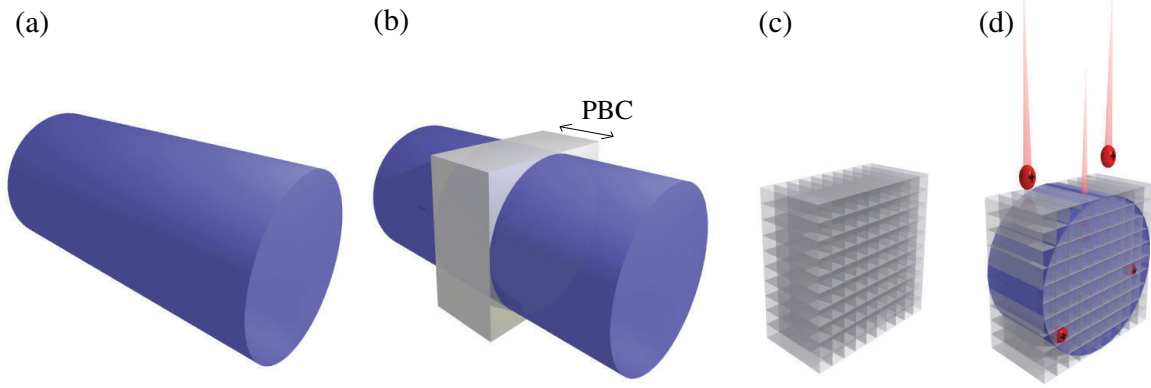


Figure 3.4: Schematic illustration of simulating ion irradiation of a nanowire with iradina. (a) A nanowire, (b) the gray shaded box is used as the simulation volume, with PBC along the nanowire axis, (c) the simulation volume is divided into cells, and (d) a cylinder is used to define the NW surface during irradiation.

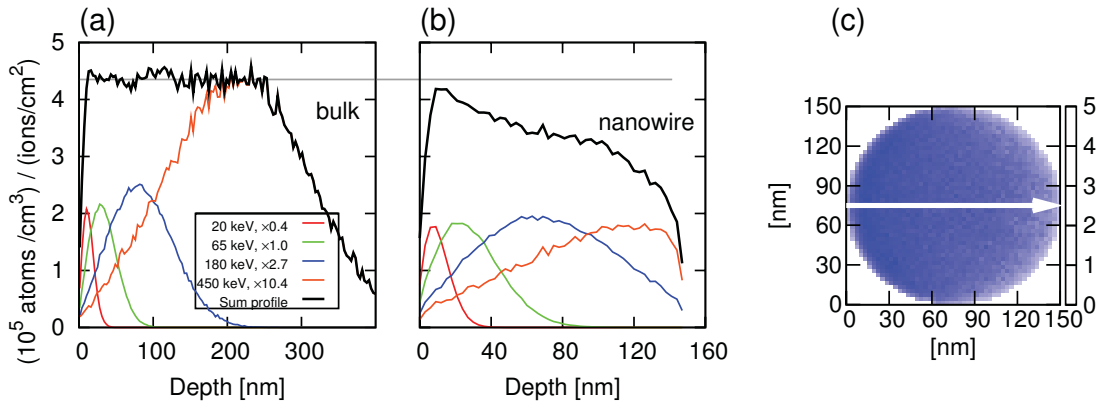


Figure 3.5: (a) Homogeneous bulk implantation profile achieved by adding simulated profiles from four different energies. (b) The same profile implanted into a GaAs NW of 150 nm diameter. (c) A cross sectional view of the nanowire, the number of implanted ions is shown as color scale. The white arrow corresponds to the profile in (b).

3.3.3 Irradiation of nanowires

The original motivation for developing *iradina* was to accurately simulate ion beam implantation into semiconductor nanowires. In the experiments performed in the scope of this thesis, all nanowires were irradiated from the side and their lengths were much larger than their diameters (details in chapters 4 and 5). Thus, it is sufficient to use only a slice from the nanowires in the simulation and apply periodic boundary conditions (PBC) in axial direction, see figure 3.4 for illustration. The simulation volume (gray shaded box in the figure), which just surrounds the slice of the NW, is divided into a number of cells in two directions (typically 30×30 or 40×40). No subdivision is required in the third direction along the nanowire axis due to the translational symmetry along the NW. The cells are used to count implanted ions and ion beam induced defects, but a cylinder is used to accurately define the NW surface as described above.

In past experiments of doping semiconductor nanowires with ion beams, bulk simulations were frequently performed in order to obtain homogeneous implantation profiles. Figure 3.5(a) shows Zn implantation profiles as simulated for bulk GaAs (these profiles were used in reference [Sti08b]). By choosing appropriate factors, profiles for four different implantation energies were superimposed to form a more or less homogeneous profile over a depth range of about 200 nm. The same implantation energies and fluencies were used to implant inclined GaAs nanowires. Now *iradina* was used to simulate the Zn implantation into GaAs nanowires with the correct target geometry, and the resulting implantation profile can be compared to the bulk simulations: figure 3.5(c) shows the concentration of implanted ions over the cross section of the nanowire and 3.5(b) illustrates the profile corresponding to the white arrow in (c) for comparison to the bulk profile. First, fewer ions are implanted into the nanowire than expected from bulk simulations, and second, the doping profile is quite inhomogeneous. The reason for this inhomogeneity can be found when comparing the implantation profiles of the lowest and highest ion energy: for the lowest energy of 20 keV, the nanowire appears almost as bulk, and most of the ions are implanted like in bulk, but for the highest energy of 450 keV, where the range is comparable to the NW diameter, many ions can leave the NW to the side or completely pass through the NW instead of being implanted.

The observation that fewer ions are implanted in the NW than expected from bulk simulations is in agreement with experimental observations: charge carrier concentrations in ion beam doped nanowires are reported to be lower than expected [Col08,Sti08b]. Partly, this can be explained by compensation, migration and fractional ionization of dopants. But the lower concentration of implanted ions in nanowires than in bulk must also be taken into account and contributes significantly to the lower charge carrier concentrations.

For high concentrations of implanted ions, it is possible to directly measure the concentration using EDX within a TEM. It is shown in chapter 5 that the concentration of Mn in ion implanted GaAs NW is in good agreement with simulation results from *iradina* using the correct nanowire geometry, whereas bulk simulations using TRIM overestimate the concentration.

3.3.4 Sputtering of nanoparticles

The sputter yields of nanoparticles (NPs) are different from bulk values and strongly depend on their size, or more precisely on the ratio of their size and the ion range. Different approaches to investigate the size-dependence of the sputter yields of NPs are reported in the literature: semi-analytical models have been used, as well as molecular dynamics (MD) simulations [Jär08,

Kli09]. *Iradina* can also be used to simulate ion beam irradiation of nanoparticles and obtain the sputter yield as a function of nanoparticle size. In order to compare results from *iradina* to results from alternative methods, two examples were selected: (1) irradiation of Au NPs with 25 keV Ga⁺ ions (compared to [Jär08]) and (2) irradiation of Au NPs with 200 keV Ar⁺ ions (compared to [Kli09]).

Figure 3.6 shows the calculated sputter yield of spherical Au NPs irradiated with 25 keV Ga⁺ ions as a function of NP diameter. Very small NPs have a low sputter yield, which can be explained by the fact that the ions only deposit a small fraction of their energy within the NPs before exiting again. The sputter yield quickly increases with diameter d and reaches a maximum at about $d = 8–10$ nm. This size is approximately the same as the projected range of the ions in bulk material (8.3 nm): the ions deposit most of their energy within the particle but the particle is still so small, that a large fraction of the kinematic energy in the collision cascades reaches the surface of the particle. At larger diameters, the sputter yield decreases again. The reason is that now the collision cascades will often not extend to the surface or the kinematic energy in the collision cascades is to a large extent absorbed within the particle and does not reach the surface. For very large NPs (> 150 nm), the sputter yield converges. Here, the NPs are much larger than the projected range, thus they appear to the ions as bulk. However, the sputter yield does not reach the bulk value (which was calculated for perpendicular incidence and is similar for *iradina* and TRIDYN). The reason is simply that the incidence angles of the ions hitting the particle at different locations are always distributed between 0° and 90°, no matter how large the NP becomes and the sputter yield depends strongly on this angle of incidence.

The behavior of the sputter yield obtained from *iradina* is similar to the results obtained by T. T. Järvi *et al.* [Jär08]. They calculated the sputter yields from molecular dynamic (MD) simulations (only possible up to 15 nm diameter) and from a semi-analytical model. Their MD results show a similar behavior as *iradina*, but their absolute sputter yields are much higher (factor 1.5–3). However, one cannot expect MC and MD simulations to yield the same results. For instance, the MD simulations will be more accurate for very small nanoparticles: while Monte Carlo (MC) simulations intrinsically assume a static solid with a temperature of 0 K, the MD allows all atoms to be in motion and can represent temperatures > 0 K. In the MD, heating of the NP by the ion impact and subsequent thermal (non-ballistic) evaporation of Au atoms is possible – as opposed to MC simulations. The following estimation shows the importance of this effect: consider a small Au NP of 10 000 atoms (≈ 7 nm diameter). Even if an ion deposits

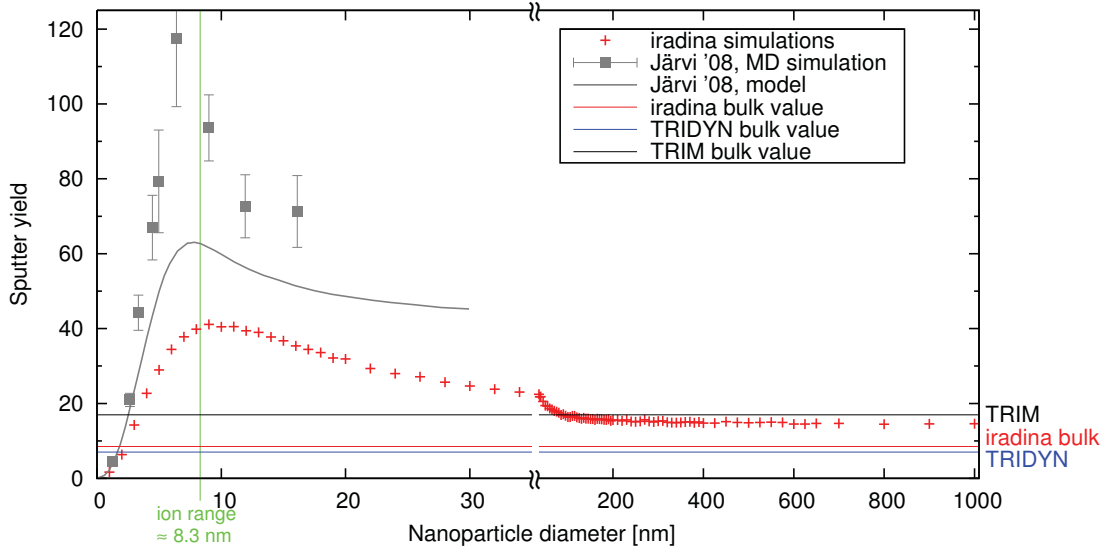


Figure 3.6: Size dependence of sputter yield for irradiation of Au NPs with 25 keV Ga^+ ions ($E_D = 25$ eV, $E_b = 0$ eV, $E_S = 3.8$ eV) calculated by iradina (+). Data from [Jär08] are shown for comparison. The bulk sputter yields for perpendicular incidence are shown as calculated with TRIM [Zie85], TRIDYN [Möl10] and iradina.

only 1 keV into heat, this accounts for an average of 100 meV per atom, corresponding to a temperature of about 900 °C, which can lead to thermal evaporation of atoms. Furthermore, the MD can simulate emission of small Au clusters with several atoms, which requires less energy than to sputter each atom individually. The MD shows indeed that about 30% of sputtered Au is emitted in clusters of two or more Au atoms [Jär08]. Nevertheless, the MD simulations allow only very limited target sizes and small ion numbers due to the extremely large computation times required. The maximum size of a Au NP reported in [Jär08] was 15 nm diameter, corresponding to 130000 atoms, and the maximum number of ions was several 100). In contrast, MC simulations allow to simulate the irradiation of a particle of 1 μm diameter with 10^5 ions within several minutes time on current standard computers.

For their semi-analytical model, Järvi *et al.* assume that the local sputter yield is proportional to the damage inflicted at the surface [Jär08]. They use a Gaussian damage distribution for a single ion impact (approximated to MC simulation results for bulk targets), determine the damage at the surface and integrate this over all entry points on the sphere. Their model results in a similar dependence of the sputter yield as a function of diameter as in *iradina*, but their absolute sputter yield is larger by a factor of about 1.5. However, for some reason, they use a bulk sputter yield of about 28 instead of what one expects from TRIDYN simulations. Possibly they assumed a lower surface binding energy.

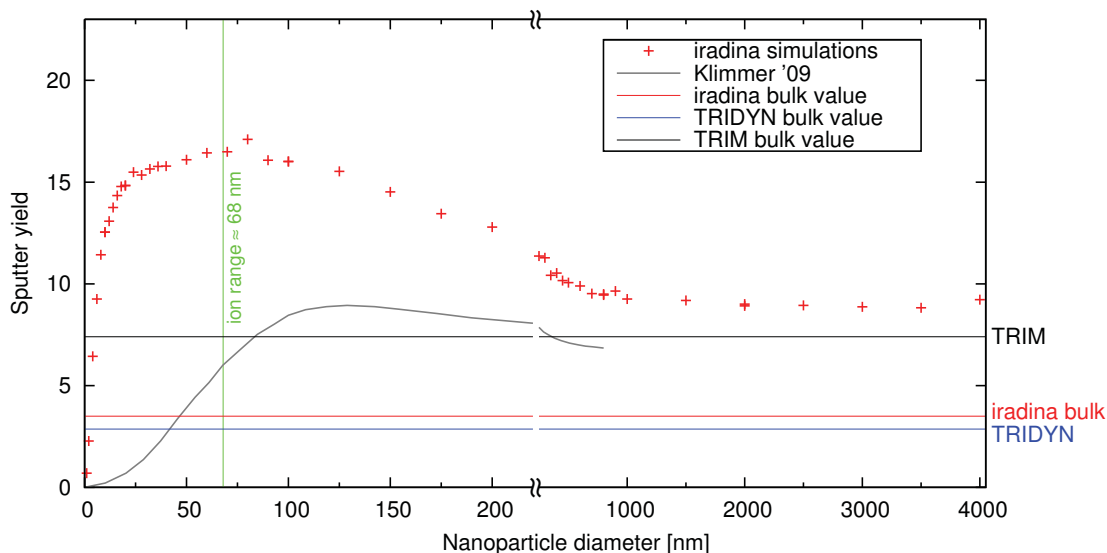


Figure 3.7: Size dependence of sputter yield for irradiation of Au NP with 200 keV Ar^+ ions ($E_D = 25$ eV, $E_b = 0$ eV, $E_S = 3.8$ eV) calculated by *iradina*. The calculation from [Kli09] is shown for comparison. The bulk sputter yields for perpendicular incidence are shown as calculated with TRIM [Zie85], TRIDYN [Möl10] and *iradina*.

Figure 3.7 shows the sputter yield of spherical Au particles irradiated with 200 keV Ar^+ ions as a function of NP diameter, obtained from *iradina* simulations. The behavior is comparable to irradiation with 25 keV Ga^+ ions: The sputter yield is very low for small particles, then increases and reaches its maximum when the particle diameter becomes comparable to the ion range. The sputter yield converges for large diameters.

Klimmer *et al.* used a similar semi-analytical approach like Järvi to calculate the sputtering of Au NPs under bombardment with 200 keV Ar ions: they obtained damage distributions from TRIM simulations, approximated them by three dimensional Gaussian distributions and integrated them of the sphere [Kli09]. Their resulting sputter yields are slightly different from *iradina* simulations in two points: Their maximum sputter yield is about 9 and their sputter yield converges to about 6.9 for large diameters. The *iradina* simulations result in a maximum sputter yield of about 17 and the sputter yield converges to about 9. This discrepancy can be explained by the fact that Klimmer *et al.* normalized their results to the bulk sputter yield of 6.9 (obtained from some version of TRIM). However, as mentioned above, it is not valid to assume that the NP sputter yield converges to the bulk sputter yield (for perpendicular incidence) due to the distribution of entry angles between 0° and 90° . Apart from that, Klimmer *et al.* find the maximum sputter yield at a diameter of about 130 nm, which is twice as large as the one obtained from *iradina*. This difference may be due to the following assumption for the energy distribution: their model uses a Gaussian energy distribution obtained from bulk

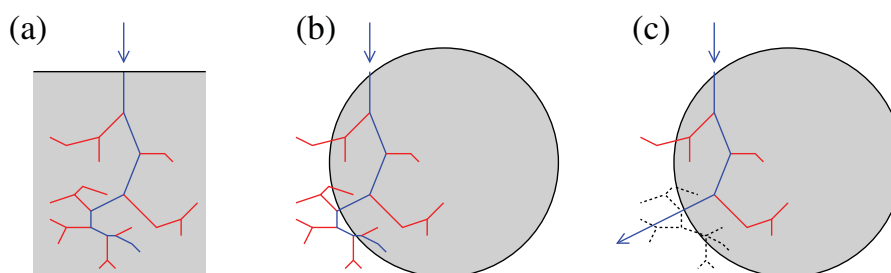


Figure 3.8: Schematic illustration of simulated collision cascades (blue: primary ion, red: recoils). (a) Cascade simulated for bulk target. (b) Applying the same cascade to a nanoparticle. (c) In reality, the ion cannot be scattered back into the nanoparticle and the damage shown by dashed black lines should not occur.

simulations. Using such an energy distribution and cutting it at the NP surface is inaccurate, because for instance projectiles leaving the nanoparticle are lost in reality, but may still deposit energy in the bulk simulations as illustrated in figure 3.8. This example nicely shows, why it is necessary to take into account the correct geometry of the nanostructure already during the MC simulation and why it is inaccurate to use bulk simulations and “cut them” to emulate irradiation of nanostructures.

3.3.5 Limitations of the simulation

When using *iradina*, one should be aware of its limitations. All Monte Carlo ion beam codes suffer from some inherent limitations, because the MC algorithm is only an approximation to what actually happens to the ion in the solid. Some other limitations are specific to *iradina*.

- Binary Collision Approximation (BCA): The projectile is assumed to collide only with one target atom at a time. At high projectile energies this is a valid assumption; but at very small energies (a few tens of eV) this becomes inaccurate as many-body interactions become important. This is no problem for the ion, as it has much higher energy most of the time, but it could be problematic for low energy recoils. Nonetheless, it does not seem to pose a large problem for sputtering; for details see [Eck91, p. 28ff].
- Random Phase Approximation (RPA): The target atoms are assumed to be at random places. Subsequent collisions are uncorrelated. This is a very strong approximation, because such a solid does not exist. Even in amorphous materials, the atoms are not at random positions, but at least first and second nearest neighbors are correlated, which is reflected in the radial distribution function. Nonetheless, the RPA works quite well in *random directions* of crystalline targets; that is when the ion beam is not aligned along

a low index crystal direction. This is often the case when irradiating nanostructures, for example for randomly dispersed nanoparticles on a substrate.

- Central Potential Approximation (CPA): the interaction potential is assumed to be a central potential. This is certainly a good approximation for ion energies where the Coulomb interaction between the two nuclei dominates. Also when the Coulomb force is partly screened by the inner-shell electrons this may still be a good approximation, but at very low ion energies (< 10 eV) the binding electrons begin to play a role and thus the potential may depend on the orientation with respect to the surrounding lattice.
- Another approximation is the model of a sharp displacement threshold: it is assumed that a recoil can only leave its lattice site permanently if it gains more energy in the collision than a certain displacement energy E_D . In reality, the recoil might for example gain just enough energy to jump to a neighbouring interstitial site, but then there are certain probabilities that it jumps back immediately or stays at its new place. Furthermore, the threshold for leaving a site depends on the direction into which the recoil moves. Thus, the displacement energies E_D used in simulation code are not well-defined microscopic physical quantities but rather empirical values, selected to fit experimental observations.
- In MC simulations, all target atoms are assumed to have no energy and momentum prior to any collision; the temperature is assumed to be 0 K. This is certainly a good approximation for calculating the collision kinematics, because even the smallest considered kinetic projectile energies (a few eV) are far larger than typical thermal energies (≈ 25 meV). Nevertheless, in reality some degree of annealing occurs (a) due to the target temperature and (b) due to the energy introduced into the target by the ion and subsequent ions (so called dynamic annealing).
- *Iradina* focuses on the irradiation of nanostructures with small ion energies, where the ion range is comparable to the nanostructures size. At these energies, the nuclear stopping typically dominates and the electronic stopping is of less importance. Therefore, some simplifications are made concerning electronic stopping, namely *iradina* does not perform compound correction of stopping and ignores the time integral in its current implementation. This latter approximation appears to be acceptable, considering the agreement between simulated implantation profiles from *iradina* and TRIM.

3.4 Summary and conclusion

A computer code named *iradina* for the simulation of ion beam irradiation of nanostructures was developed. The program simulates the transport of energetic ions through matter by a Monte Carlo (MC) algorithm using the binary collision approximation (BCA). The ion is followed step by step from collision to collision until it has lost its kinetic energy or leaves the simulation volume. Recoils are followed recursively to simulate the collision cascade. The target in *iradina* is defined as a three-dimensional rectangular equal-spaced grid, which allows to represent arbitrarily shaped nanostructures, in contrast to many other (TRIM-like) MC programs. The comparison of simulation results from *iradina* and TRIM for implantation into bulk material demonstrates the basic correct functionality of the code. Several very fast routines (for example for the calculation of scattering angles and for electronic stopping) are adopted from the open source computer code *corteo*, published by F. Schiettekatte [Sch08]. These make *iradina* faster compared to TRIM by up to about two orders of magnitude, depending on the computer in use and the simulation parameters.

Experimental results for ion beam implantation into GaAs nanowires show that it is indeed important to take into account the correct geometry of the target structure during the simulation: the concentration of implanted ions obtained from *iradina* simulations with the nanowire target geometry are in much better agreement with experimental observations than bulk simulation carried out with TRIM. Furthermore, *iradina* was used to simulate the implantation of boron into Si nanowires and the results were compared with simulation results obtained from the new version of TRIDYN, which is currently being developed and supports three dimensional target definitions [Möl11]. The results of this comparison are also in reasonable agreement, which further indicates that *iradina* works correctly.

One interesting application of *iradina* is the calculation of sputter yields from nanostructures, which deviate strongly from bulk sputter yields. The sputtering from spherical Au nanoparticles is discussed and *iradina* results are compared to alternative methods. First, the bulk sputter yield obtained from *iradina* is compared to values obtained from TRIM and TRIDYN. There is reasonable agreement with the TRIDYN results, while the TRIM results differ strongly. It is not known to the author of this thesis, how exactly TRIM works and calculates the sputter yield, because the source code of current versions of TRIM is not available. Therefore, the reason for the deviation could not be identified. Further information might be obtained by comparing the distribution of energy and ejection angles of sputtered particles. For the

sputtering of Au nanoparticles, *iradina* results exhibit a strong size-dependence of the sputter yield. The observed trends are in good agreement with results from MD simulations and similar to the trends observed from semi-analytical approaches, which integrate damage distributions obtained from TRIM simulations. The exact numbers are different though, which is partly caused by different normalization and due to errors made when using damage distributions simulated for bulk and applying them to spherical nanoparticles. Furthermore, it must be said that there are several uncertainties for very small nanoparticles. For example, the uncertainty of the surface binding energy E_S remains as a major inaccuracy, because E_S may be lower for strongly curved surfaces than for flat surfaces. Additionally, the sputter yield is an average value, but the actual number of sputtered atoms for each individual ion scatters largely, as illustrated in appendix B.4. This is less important for experiments irradiating bulk but may have severe effects when sputtering small nanoparticles, where a significant fraction of the particle may be sputtered away by a single ion. For example, this effect has been observed to cause roughening of ion beam implanted nanowires [Sti08a, p.77].

While the current version of *iradina* has been shown to yield appropriate results in agreement with experiments and other codes, there is still room for improvement. For example, compound correction for stopping powers, the time integral, and correction of stopping when crossing cell boundaries could be implemented. Moreover, the possibility to allow composition changes during simulation and to relax a target structure would be very interesting for *dynamic* simulations. However, allowing relaxation in three dimensions and maintaining a rectangular grid is more complex than relaxation in one dimension.

Chapter 4

Ion Beam Induced Bending of Nanowires

This chapter reports on the ion beam induced bending of GaAs and ZnO nanowires. Experimental results for GaAs and ZnO nanowires are presented as well as results from Monte Carlo simulations and a dynamic bending model. The experiments on GaAs nanowires were done in collaboration with the group of Dr. W. Prost/Prof. F.-J. Tegude at the University of Duisburg-Essen, where the nanowires were grown; some of the results are published in [Bor09]. The experiments on ZnO nanowires were done in close collaboration with Susann Spindler (see her diploma thesis [Spi11]) and are partly published in [Bor11c]. Results from the dynamic bending calculations are unpublished up to now.

4.1 Motivation and background

A variety of chemical and physical growth techniques to create nanowires have been reported (see introduction). Even so, it is not possible to achieve any arbitrary desired shape, morphology or growth orientation. The orientation of the growing nanowires is sometimes limited by epitaxial relations putting a constraint on possible applications, as illustrated in the following example: in semiconductor electronics, [100]-oriented substrates are always used due to the better quality of the (100) surface plane (lower trap density than (111)). However, zinc blende structured semiconductor nanowires like GaAs usually grow in a $\langle 111 \rangle$ -type direction, thus it is difficult to perpendicularly grow nanowires on such [100]-oriented substrates.

For many applications, post-growth methods to control the shape, morphology and orientation of nanowires are required. Different methods to align large numbers of nanowires have been reported, for example the Langmuir-Blodgett technique [Kim01], the blown bubble film approach [Yu08] or alignment by dielectrophoresis [Smi00]. The disadvantage of these methods is the necessity to suspend the nanowires in solution.

It has been known for some time that ion beam irradiation can cause plastic deformation of materials [Tri95] and that shape and morphology of nanostructures can be manipulated using ion beams [Tub09, Kra10], one example being the “ion hammering” effect [Sno00]. However, ion beam induced morphological and structural changes of nanostructures are often observed as undesired side effects of ion beam doping.

The advantage of using ion beams to control nanowire shape, morphology or orientation is the possibility to irradiate a large area and modify large numbers of nanowires in parallel. Furthermore, any nanowires can be irradiated independent of the growth method, and suspension in solution is not required.

Bending of semiconductor nanowires under ion beam irradiation was first observed as an unwanted side effect during ion beam doping of nanowires [Sti08a, Sti08b]. In 2009, several groups reported the use of ion beam irradiation with the purpose to bend or align semiconductor nanowires:

(1) Romano and Pecora *et al.* irradiated Ge nanowires with 30 keV Ga ions in a focused ion beam system [Rom09]. They observed bending of the nanowires toward the ion beam and explained this effect by densification of the amorphized material or ion hammering in combination with a negative thermal expansion coefficient. In later experiments, they studied the bending of Si nanowires under 45 keV Ge ion irradiation and the influence of annealing on the bending [Pec10, Pec11]. They observed bending and alignment only above a fluence threshold, which corresponds to amorphization of the NW material. Upon annealing and recrystallization they observed a reversal of the bending.

(2) Jun *et al.* irradiated single Si nanowires with 30 keV Ga ions using a focused ion beam system [Jun09]. Their experiments were different from the Catania group: in most cases they focused the beam on one spot of the nanowire, instead of scanning the beam about an area surrounding the nanowire for imitating homogeneous irradiation. On the point of irradiation, the nanowire kinks and bends toward the ion beam direction. For homogeneous low dose irradiation they observed bending away from the ion beam. They explained their findings by tensile stress caused by amorphization of Si and at low doses by compressive stress caused by interstitial Ga, respectively.

(3) The bending and alignment of GaAs nanowires under ion beam irradiation was investigated in the scope of this thesis [Bor09]. Following the studies with GaAs nanowires, the bending of ZnO nanowires was examined in much more detail for several reasons. As opposed to elemental group IV and III-V compound semiconductors, ZnO can hardly be amorphized by ion irradi-

ation. Thus, it allows to test bending models relying on amorphization and it allows to study the crystal structure in detail after high fluence irradiation. Furthermore, as discussed in the introduction, the ion beam doping of ZnO nanowires with electrically, optically or magnetically active dopants is of great interest. Understanding the structural and morphological impact of ion irradiation on the ZnO nanowires helps to avoid or even utilize originally undesired side effects, for example making use of bending to achieve alignment.

A number of nanowire bending experiments have been reported in which the nanowires were bent mechanically by external forces. For static experiments, microwires were directly bent with tweezers [Die11] or nanowires were bent with a nanomanipulator [Che07a] or an AFM tip [Hof06] within a SEM. Other bending experiments were done dynamically by exciting mechanical oscillations of the nanowires similar to a pitchfork [Che06, CT10] and determining resonance frequencies. The elastic bending by *external* forces is quite different from bending by ion beam irradiation, because ion irradiation causes bending by *internal* changes in the NW structure. Nevertheless, the mechanical properties of nanowires as determined from external bending measurements are important for the discussion of ion beam induced bending as well. In particular, the Young moduli and fracture strengths of semiconductor nanowires depend on their diameter; for ZnO nanowires they are both increased compared to the bulk value [Che06, Che07a, Agr08]. The diameter dependence of the Young modulus can be explained by a superposition of bulk modulus and a surface modulus, the latter being different due to different bond lengths near the surface: the Young modulus scales with the inverse fourth power of bond length [Agr08]. Increased fracture strengths of semiconductor nanowires are attributed to the lack of crystal imperfections from which fractures are initiated and propagate in bulk material.

There is one report on the investigation of the strain of ZnO nanowires caused by low energy ion beam induced bending [Che11]; however, the bending mechanism is not discussed at all and no correlation to the ion beam induced structural changes is made. Another reported possibility to bend nanowires is depositing additional material on the NW side by pulsed laser deposition (PLD) [She10], but the mechanism is not fully understood and may actually be the same as ion irradiation (atoms in PLD may be “deposited” with up to a few hundred eV).

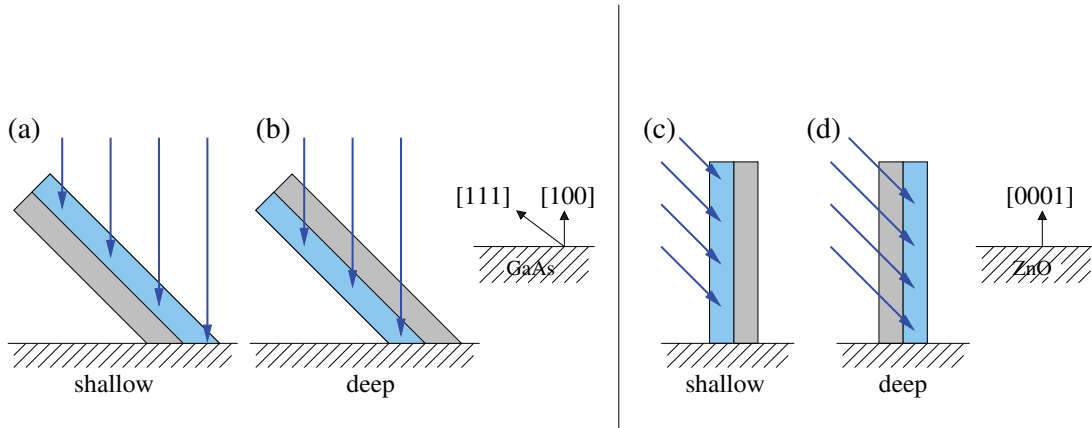


Figure 4.1: Schematic illustration of the two implantation conditions. (a,b) GaAs NW mostly grow in $[111]$ -direction epitaxially on GaAs substrate with $[100]$ surface normal, thus the NW are inclined. Irradiation from the top. (a) Shallow implantation, where ions are implanted to the side of the NW facing the ion beam, (b) deep implantation, where ions are implanted to the back half. (c,d) ZnO NW grow in c -direction epitaxially on c -oriented ZnO substrates, thus perpendicular. Irradiation from the side. (c) Shallow implantation, (d) deep implantation.

4.2 Irradiation experiments

4.2.1 Ensemble irradiation

Substrates with well aligned epitaxially grown nanowires were irradiated with ions using the general purpose implanter ROMEQ (details in section 2.2). The ion beam was not focused, leading to a large number of nanowires being irradiated simultaneously, which is why these experiments are designated *ensemble irradiations*. Noble gas ions were selected in order to exclude chemical effects occurring in the NWs. The noble gas atoms are assumed mostly to diffuse out after being implanted.

Inclined GaAs nanowires with diameters of about 150 nm were irradiated with Ar and Xe ions perpendicular to the substrate surface and at room temperatures. Energies between 35 keV and 210 keV were selected to achieve projected ranges significantly below and above the radius of the nanowire. This was done in order to realize (1) shallow implantation, where mostly just one half of the nanowire is affected and (2) deep implantation, where ions are implanted to the “back-side” of the nanowires, see illustration in figure 4.1(a,b). The fluencies were increased in several steps from $1 \cdot 10^{13}/\text{cm}^2$ to $5 \cdot 10^{15}/\text{cm}^2$.

Perpendicular ZnO nanowires with diameters in the range of typically 50 to 120 nm were irradiated with Ar ions under angles of about 38 to 45°. Energies of 10 keV and 20 keV were used for shallow implantation and energies of 100 keV and 200 keV were used for deep implantation, see figure 4.1(c,d).

In between each irradiation step, the samples were investigated using a SEM (see section 2.3) to study the bending as a function of ion fluence. To characterize the bending, the curvatures of a number of nanowires were measured from the SEM images of each sample. These ensemble measurements have two disadvantages: First, for each step of increasing fluence, the samples have to be taken out of the implanter, have to be transferred to the SEM, characterized and then taken back to the implanter. Only one step of increasing fluence could be done per slot of beam time, so that the total number of possible fluence steps was very limited. The other (minor) disadvantage is that it is usually not possible in the SEM to find exactly the same nanowires after each step. But on the other hand, the ensemble irradiation also has several advantages: First, all ion species are available in the implanter, which allows using noble gas ions, second, all ion energies in the range from 10 keV to 380 keV are available and third, due to the large number of nanowires irradiated simultaneously it is possible to obtain good statistics of the curvature as a function of fluence.

4.2.2 Single nanowire irradiation

Using a focused ion beam (FIB) machine avoids the two disadvantages of the ensemble irradiation. The focusing of the beam allows single nanowires to be irradiated and most importantly, the bending of the nanowires can be observed practically *in-situ* with the SEM column of the FIB. It is possible to record the bending of a single nanowire as a function of fluence for a large number of small fluence steps: in each step, the NW is irradiated with a very small fluence of ions, the ion beam is blanked, a SEM image is recorded using the electron beam and then ion irradiation is continued. The ion irradiation of the NW is done by scanning the focused ion beam over a quadratic area surrounding the NW. The fluence steps are chosen small ($\approx 1 \cdot 10^{13}/\text{cm}^2$) to achieve “quasi-homogeneous” irradiation of the NW.

One significant limitation of the available FIB machines is the maximum ion energy of 30 keV, which just allows to realize the situation of “shallow implantation”, where the ions only penetrate a small fraction of the nanowire. The other disadvantage is the choice of ions, limited to Ga: at high fluencies, the implanted Ga contributes a significant atomic fraction to the nanowire material, which may change its material properties.

4.2.3 Subsequent annealing

In order to investigate the stability of the bent state against annealing, irradiated and bent ZnO nanowires were annealed in subsequent steps at temperatures from 500 °C to 900 °C for 30 minutes each. Annealing was performed in ambient conditions. When annealing ZnO nanowires in vacuum, oxygen is lost, but this loss is avoided when annealing in air. The curvatures of the nanowires were measured in between each annealing step. From doping experiments of ZnO nanowires, it is known that typically 700 °C in air are sufficient to remove most of the ion beam induced damage and to activate dopants [Geb08b].

4.2.4 High temperature implantation

In order to gain additional insight into the bending mechanisms, a few substrates with ZnO nanowires were irradiated at elevated temperatures ranging from 300 °C to 800 °C. High temperature irradiation was only possible for the *ensemble* irradiation using the ROMEIO implanter, because the FIB machines were not equipped with heating stages.

4.3 Results on bending and alignment

4.3.1 GaAs nanowires

Ensemble irradiation

Figure 4.2(a-c) illustrates the effect of 35 keV argon irradiation (shallow implantation) on GaAs nanowires. The NWs are initially inclined but straight, see figure part (a). With increasing fluence, the nanowires bend down toward the substrate, away from the ion beam. Note that some NWs appear to be perpendicular. This is due to the four possible $\langle 111 \rangle$ -type growth directions and the orientation of the NWs with respect to the electron beam in the SEM. The NWs, which appear perpendicular, are inclined toward or away from the direction of the electron beam and their bending cannot be observed.

The effect of higher energy irradiation with 210 keV Ar ions (deep implantation) is illustrated in figure 4.2(d-f). In this case, the initially straight nanowires bend upward with increasing fluence. At high fluencies of $1 \cdot 10^{15}/\text{cm}^2$ the nanowires become almost perpendicular and thus aligned with the incident ion beam direction.

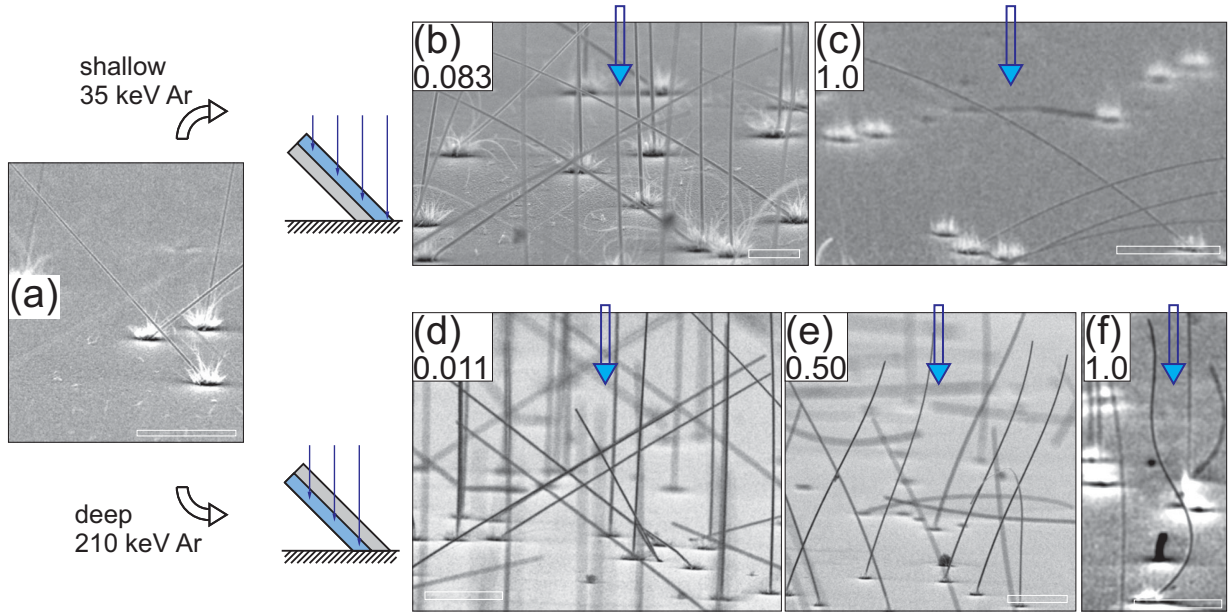


Figure 4.2: SEM images of GaAs nanowires (150 nm diameter) irradiated with 35 keV Ar ions (top row, shallow implantation) and 210 keV Ar ions (bottom row, deep implantation). Blue arrows indicate ion beam direction. Numbers denote ion fluence in $1 \cdot 10^{15}/\text{cm}^2$. (a) As-grown, straight, non-irradiated NW, (b,c) down-bending, (d-f) up-bending and alignment toward ion beam. All scale bars show 5 μm .

Single nanowire irradiation

Irradiation of a single GaAs nanowire with 30 keV Ga ions was performed using a FIB with *in-situ* SEM imaging. The results are illustrated in figure 4.3. The nanowire is initially inclined but straight. Under ion beam irradiation the nanowire begins to bend down toward the substrate away from the ion beam. However, starting at fluencies of approximately $1 \cdot 10^{16}/\text{cm}^2$ the nanowire begins to decompose. The reason becomes obvious when taking a look at the GaAs phase diagram [Sci94] and taking into account that the FIB features a Ga ion beam: the only stable mixed phase is stoichiometric $\text{Ga}_{0.50}\text{As}_{0.50}$, phase segregation into GaAs and pure Ga or As occurs for all other compositions in thermal equilibrium. Irradiation is done at RT, where thermal equilibrium phases may not be reached; however, the impacting ions may provide sufficient energy to cause phase segregation. The NW material is thus quickly destabilized rendering meaningful evaluation of NW curvatures impossible. In the SEM images one can observe an emerging droplet at the top of the NW, which probably consists of the excess Ga implanted by the ion beam (the melting point of Ga is about 30 °C, which is most probably reached in the NW due to heating by ion and electron beam). At very high fluencies, these droplets also appear on the substrates.

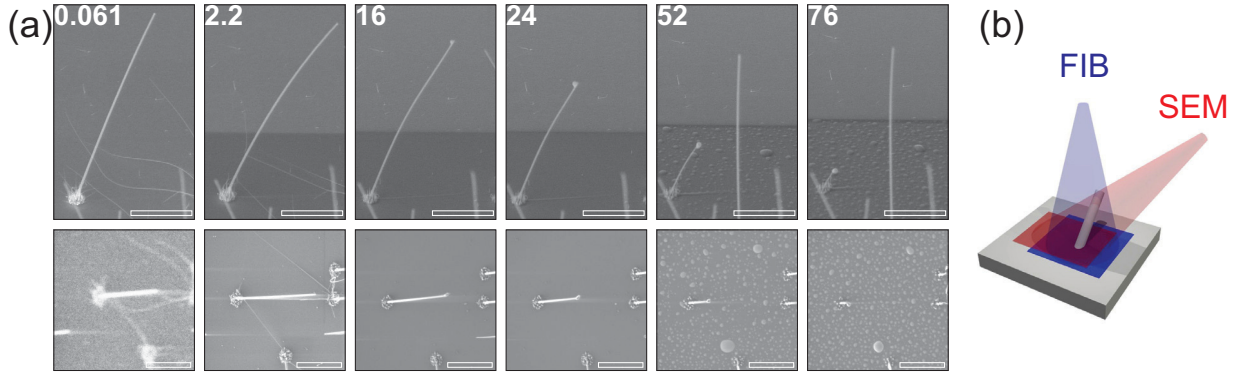


Figure 4.3: (a) A single GaAs nanowire, irradiated with 30 keV Ga ions within a FIB system. Top row: SEM images with increasing ion fluence from left to right. The numbers denote fluences in units of $1 \cdot 10^{15}/\text{cm}^2$. Bottom row: corresponding “ion images” from secondary electrons generated during ion beam irradiation. Scale bars show $5 \mu\text{m}$. (b) Schematic illustration of geometry. Ions irradiate inclined NW from the top, electron beam scans NW from the side.

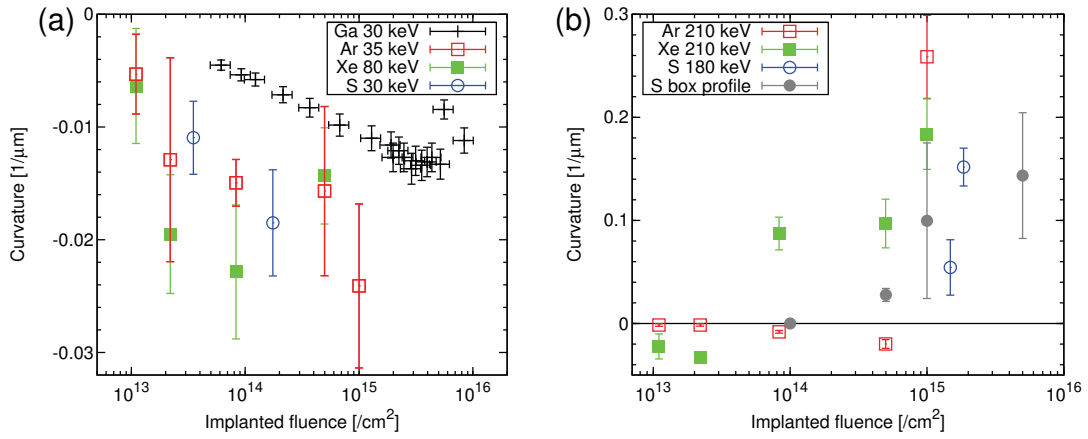


Figure 4.4: The curvature of the irradiated nanowires as a function of ion fluence for (a) shallow implantation and (b) deep implantation. Negative curvature denotes bending away from ion beam, positive curvature toward ion beam.

Figure 4.4 shows the curvature of irradiated GaAs nanowires as a function of ion fluence. The curvature is the reciprocal value of the bending radius; positive values of curvature are used for upward bending toward the ion beam and negative values of curvature are used for downward bending away from the ion beam. The data points for 30 keV Ga irradiation are determined from the single nanowire irradiated in the FIB, the accuracy is estimated to about 10%. No curvatures were measured above $1 \cdot 10^{16}/\text{cm}^2$, because of starting decomposition of the NW. Data points for other ion species and energies were obtained from ensemble irradiations. About ten different nanowires were measured for each data point and the error bars represent the standard deviation of curvatures, which is rather large in some cases. Additionally, the curvature is not always the same along the complete nanowire. Thus, especially for NWs which are almost

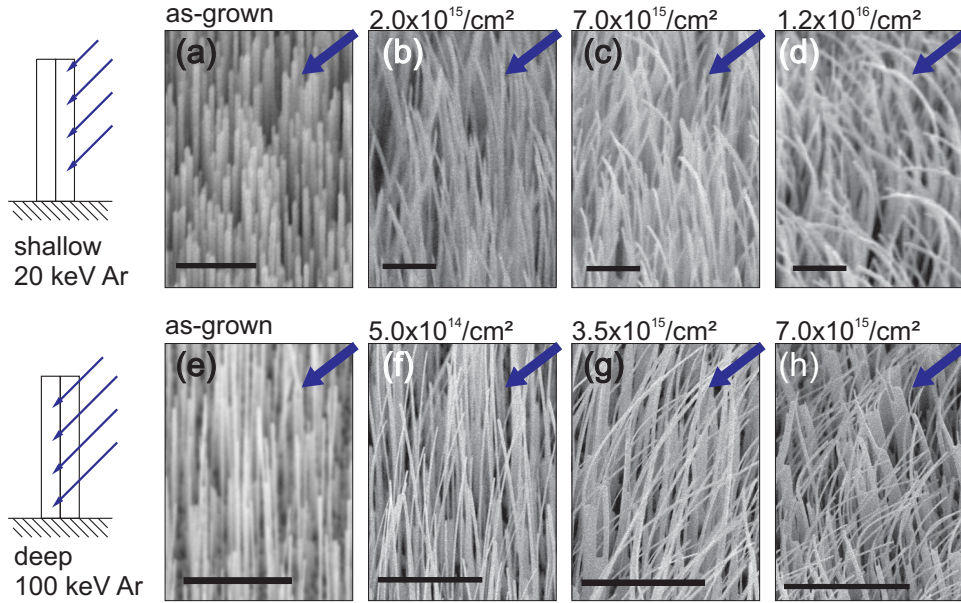


Figure 4.5: (a-d) SEM images of ZnO nanowires (≈ 60 nm diameter) irradiated with 20 keV Ar ions (shallow implantation) with increasing fluencies as denoted, scale bars are $1 \mu\text{m}$. (e-h) ZnO nanowires (≈ 90 nm diameter) irradiated with increasing fluencies of 100 keV Ar ions (deep implantation), scale bars are $5 \mu\text{m}$. Blue arrows indicate ion beam direction.

perpendicularly aligned a single value for the curvature cannot be defined clearly, leading to large errors.

Although the statistical deviations are quite large, a general trend can be observed for both cases: down-bending away from the ion beam for shallow implantation as well as up-bending toward the ion beam for deep implantation, both increasing with ion fluence. Note, however, that also in the deep implantation case the NWs first bend down a little bit before bending upward for Ar as well as Xe implantation.

Figure 4.4 also shows bending results from irradiation experiments with sulfur ions (originally intended for n-doping of the GaAs NWs). These results exhibit in general similar trends to irradiation with noble gas ions.

4.3.2 ZnO nanowires

Ensemble irradiation

Figure 4.5 (top row) illustrates the effect of 20 keV Ar irradiation (shallow) on ZnO nanowires for increasing fluencies. The nanowires are initially straight and perpendicular, but with increasing ion fluence, they bend away from the ion beam. Similar observations are made for 10 keV Ar ions (also shallow implantation case, not shown here). The case of deep implantation (100 keV Ar ions) is illustrated in figure 4.5 (bottom row). The initially straight nanowires bend

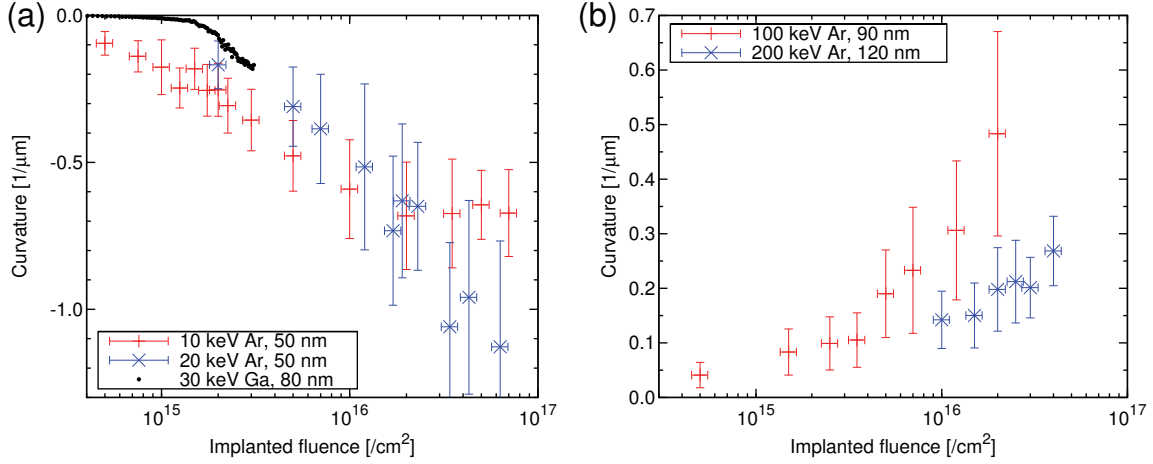


Figure 4.6: Curvature of ZnO nanowires as a function of fluence. (a) Shallow implantation, NWs bending away from ion beam and (b) deep implantation, NWs bending toward ion beam. Typical NW diameters are noted in the key.

toward the ion beam with increasing fluence until they become approximately aligned with the ion beam direction. Similar observations were also made for 200 keV Ar ions (also deep implantation, not shown here). These two trends observed for ZnO are the same as observed for GaAs nanowires.

After each irradiation step, the curvatures of the ZnO nanowires were evaluated from SEM images as described above, in this case measuring about 200 nanowires for each data point. The resulting curvatures as a function of fluence are plotted in figure 4.6. One can clearly observe that the curvature becomes stronger with increasing ion fluence for both cases of bending away and toward the ion beam. Irradiation with 10 keV and 20 keV Ar ions result in comparable bending, taking into account the distribution of curvatures. In both cases, the average diameter of the nanowires was approximately 50 nm; however, the exact distribution of diameters varies from sample to sample limiting inter-sample comparison of curvatures. The curvature results of single nanowire irradiation with the FIB (30 keV Ga) are shown for comparison, details follow in the next section. For the deep implantation case (irradiation with 100 keV and 200 keV Ar ions), the NW diameters were different, but the curvature shows similar trends of bending toward the ion beam for both energies.

Single nanowire irradiation

Figure 4.7 illustrates a single ZnO nanowire irradiated with a focused ion beam. SEM images were recorded after each of the ≈ 100 small steps of irradiation, six of them are shown exemplarily. The curvature of the nanowire as a function of fluence is plotted in figure 4.7(g). The

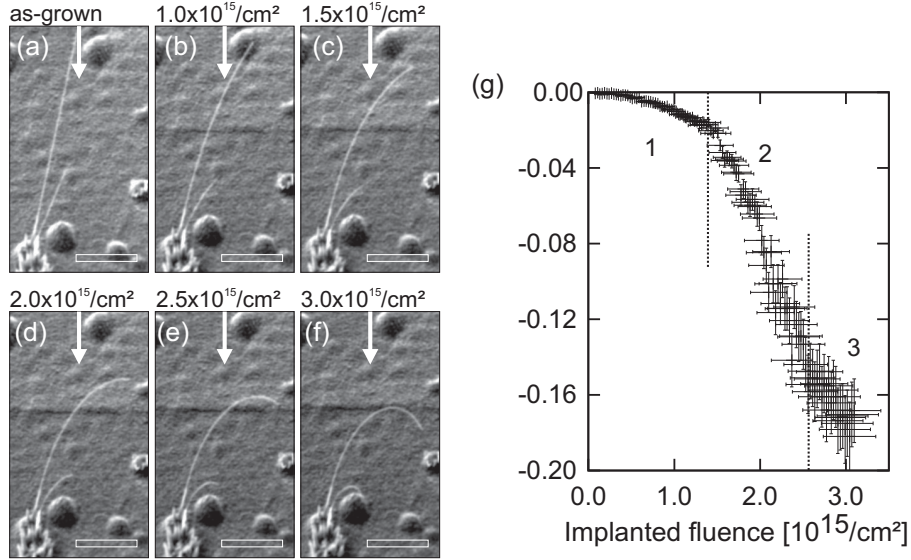


Figure 4.7: FIB-irradiation of a single ZnO nanowire with diameter of 80 nm: (a-f): SEM images, recorded after irradiation with increasing ion fluence as noted. The white arrows indicate the ion beam direction. Scale bars are 10 μm . (g) Curvature as a function of fluence. (The curvature was measured at the point of strongest bending.)

error bars of the curvature represent the fact that the curvature is not constant along the NW and the error bars in the fluence represent the uncertainty of the ion beam current that cannot be measured exactly in the FIB (10% accuracy estimated).

The curvature as a function of fluence shows the same general trend as for shallow Ar implantation: the nanowire bends away from the ion beam. However, the larger number of data points allows a more detailed analysis. Furthermore, in comparison to the FIB-irradiated GaAs nanowire, the ZnO nanowire seem to be more stable against Ga irradiation, because the NW does not decompose before very strong bending occurs. In the plot of curvature versus fluence, one can discern three not sharply separated domains, as illustrated in figure 4.7(g): (1) slow bending up to about $1.4 \cdot 10^{15}$ ions/cm², (2) accelerated bending up to about $2.6 \cdot 10^{15}$ ions/cm², and (3) slower bending again at higher fluencies. Discussion follows below (section 4.4.3) after establishing a model for the bending mechanism.

Similar experiments were done for 11 different single nanowires in the FIB (results not shown here, can be found in [Spi11]). They all show in general a similar behavior; however, the absolute value of curvatures and the fluencies necessary to achieve the same curvature are different for all the nanowires. One reason are different diameters and different initial angles between ion beam and nanowire, but no distinct correlation between these parameters and bending curvatures could be found [Spi11]. Different adjustments of the FIB machine on different days may play a role here.

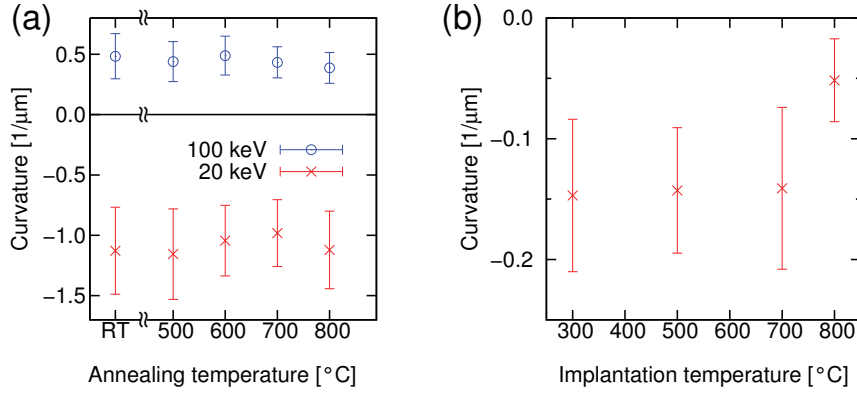


Figure 4.8: (a) Curvature of ZnO nanowires irradiated at RT and subsequently annealed at increasing temperatures. The samples were irradiated with Ar ions of 20 keV with a fluence of $6.3 \cdot 10^{16}/\text{cm}^2$ and 100 keV with a fluence of $2.0 \cdot 10^{16}/\text{cm}^2$. (b) Curvature of ZnO nanowires irradiated at different temperatures with $2 \cdot 10^{16}/\text{cm}^2$ Ar ions of 20 keV.

Annealing of bent nanowires and high temperature irradiation

Figure 4.8(a) shows the curvature of ZnO nanowires, which were irradiated at room temperature and subsequently annealed at increasing temperatures up to 800 °C. In between each annealing step, the samples were characterized in the SEM (images not shown here, can be found in [Spi11]), and the curvatures of a large number of nanowires were measured. For both directions of bending, there is no significant change in the curvature as a function of annealing temperature, showing that the bent state is stable upon annealing. At 900 °C, the nanowires begin to melt and no curvatures can be measured. Interestingly, the melting point of bulk ZnO is much higher (1975 °C). Even though nanostructures can have lower melting points compared to bulk, this cannot explain melting at 900 °C. However, during ion beam irradiation, carbon from the residual gas in the vacuum vessel is deposited on the ZnO nanowires. Carbon reduces ZnO already at 900 °C [Wan08], and the remaining pure Zn melts at 419 °C.

In order to investigate the influence of temperature *during* the irradiation, different nanowire samples were irradiated at various temperatures in the range from 300 °C to 800 °C with Ar ions of 20 keV and a fluence of $2.0 \cdot 10^{16}/\text{cm}^2$. The resulting curvatures are shown in figure 4.8(b). It should be noted that different samples were used, which have similar but not exactly the same distribution of NW diameters, so the comparability of the data points is limited. Nevertheless, up to irradiation at 700 °C, the curvature remains about the same. At 800 °C, the curvature is significantly less; the NW are only slightly bent (SEM images of NW irradiated at high temperatures can be found in [Spi11]).

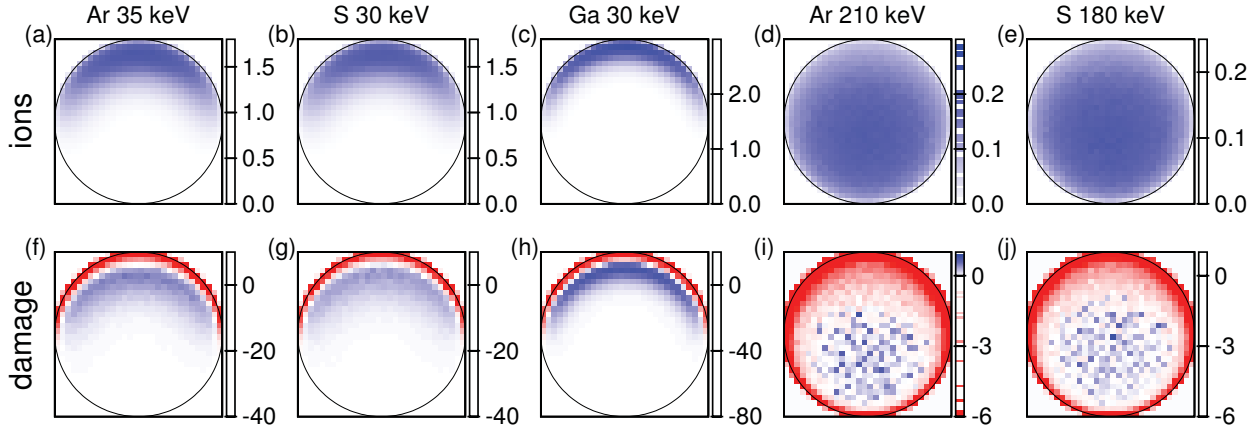


Figure 4.9: Results from *iradina* simulations for irradiation of GaAs NW (150 nm diameter) with different ions and energies. NW cross sections are shown; the ion beam comes from the top in all cases. The top row (a-e) shows concentration of implanted ions, the bottom row (f-j) shows the value of interstitials minus vacancies. For each image, the color scale denotes the concentration of ions or defects in units of $10^5/\text{cm}^3$ per ions/ cm^2 .

4.4 Discussion with qualitative model

In order to understand the mechanisms causing the nanowires to bend in different directions upon ion beam irradiation, one has to take a closer look on how exactly the ions interact with the nanowire material. At the energies used for these studies, the number of point defects (vacancies and interstitials) produced per ion is in the order of 10^3 (as calculated by *iradina* or TRIM [Zie85]). Additionally, noble gas atoms are assumed to easily diffuse out of the material after implantation. These considerations indicate that the bending is mainly related to defect production and not to the implanted ions themselves. To obtain a good understanding of the bending mechanism, it is necessary to know the distribution of defects within the nanowire. This distribution can be obtained from Monte Carlo computer simulations of the ion irradiation.

4.4.1 Simulations and ion beam induced defects

*Iradi*na was used to simulate the irradiation of GaAs and ZnO nanowires with different ion species and energies corresponding to the parameters used in the experiments (see section 3.3.3 for details on the simulation). Figures 4.9 and 4.10 show simulation results for irradiation of GaAs and ZnO nanowires with different diameters, ions and ion energies, as used in the experiments¹. In the top rows, the concentration of implanted ions is plotted, each colorized dot

¹The simulations shown in the publication [Bor09] were performed with a 3d-variant of TRIM by Daniel Schwen, University of Illinois [Sch09b], because *iradina* had not been developed at that time. The simulation

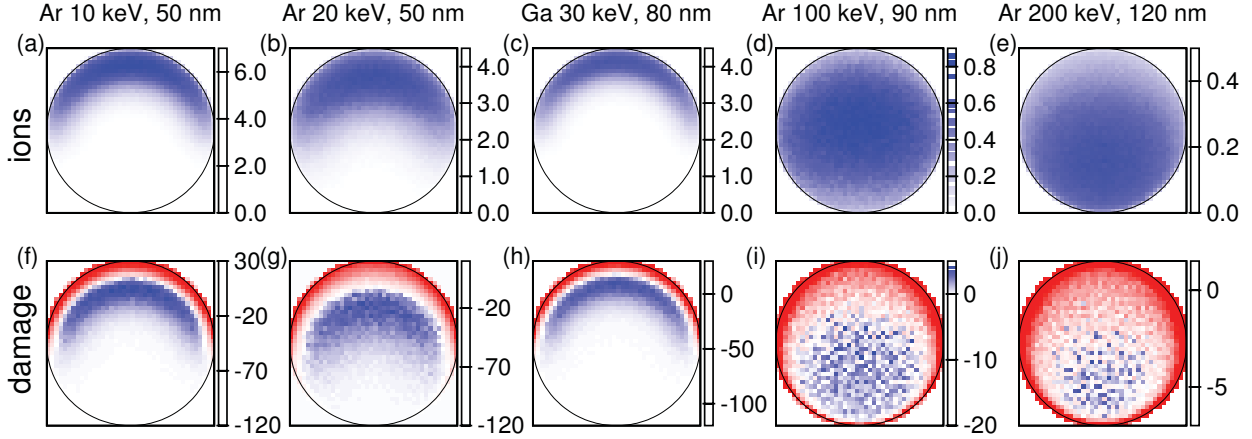


Figure 4.10: Results from *iradina* simulations for irradiation of ZnO NW with different diameters, ions and energies. NW cross sections are shown; the ion beam comes from the top in all cases. The top row (a-e) shows concentration of implanted ions, the bottom row (f-j) shows the value of interstitials minus vacancies. For each image, the color scale denotes the concentration of ions or defects in units of $10^5/\text{cm}^3$ per ions/ cm^2 . Ar irradiation: 38° between ion beam and NW, Ga irradiation: 27° .

corresponding to one cell of the simulation. For the cases of low-energy (shallow) implantation shown in subfigures (a-c) one can observe that the ions are only implanted into that side of the nanowire, which faces the ion beam. For the high-energy implantations shown in subfigures (d,e), the ions are implanted deep into the nanowire; nevertheless, ions can be found almost everywhere in the nanowires.

Concerning the production of point defects by the ion beam, it must be taken into account that Monte Carlo simulation codes like *iradina* do not take into account any annealing (dynamic or thermal); implicitly, a temperature of 0 K is assumed. In reality, however, annealing occurs and for example a vacancy may annihilate with a close-by interstitial. Room temperature, where irradiation took place, is above a major recovery stage of GaAs reported at 250 K [Hof92]. In ZnO, annihilation of vacancies and interstitials is also very likely; shown by the fact that ZnO can hardly be amorphized by ion irradiation due to its high ionicity [Nag75]. However, diffusion of point defects over large distances is unlikely at room temperature. In order to make a rough estimate of the remaining defects from the simulation results, one may assume that interstitials and vacancies can annihilate within each cell of the simulation, but not across cell boundaries (typical cell dimensions are 1 to 4 nm). A vacancy and an interstitial are always created together in the collision cascade, but the vacancy remains at the point of the collision, while

results shown here are obtained from *iradina* simulations done with higher accuracy than the ones shown in [Bor09].

the interstitial proceeds some distance before it stops. On average, interstitials are transported forward due to the momentum of the incoming ion. Thus, the spatial distribution of vacancies and interstitials is not exactly the same. When assuming fully effective annihilation of point defects within each cell, some cells will have excess interstitials and some excess vacancies. This is illustrated in figures 4.9 and 4.10, subfigures (f-j), which show the difference value of interstitials minus vacancies. Red shows excess vacancies, blue excess interstitials.

The inhomogeneous distribution of defects within the nanowire results in an inhomogeneous distribution of stress: material with vacancy excess tries to reduce its volume causing tensile stress, while material with excess interstitials tends to expand causing compressive stress. These inhomogeneous distributions can now explain both bending directions away and toward the ion beam for shallow and deep implantation in a qualitative way:

In case of the shallow implantation, the defect distribution is centered near the surface of the NW on the side facing the ion beam, see figure 4.9 and 4.10 (f-h). A closer look shows that a high concentration of excess vacancies only occurs in the cells which are at the NW surface. This is due to the static simulation, where the surface remains fixed: recoils leaving the NW (sputtered atoms) do not lead to interstitials and thus, excess vacancies accumulate close to the surface. In reality, the surface itself is retracted due to sputtering and such a strong accumulation of vacancies at the surface cannot occur. However, many cells with excess interstitials remain within the nanowire. For shallow implantation, these excess interstitials occur in the half of the NW which faces the ion beam, causing this half of the NW to expand. The other half remains undamaged. Consequently, a bending momentum is induced. For shallow implantation this bending momentum bends the nanowire *away* from the incident ion beam. In the case of deep implantation, the damage is produced all over the nanowire cross section, but excess vacancies remain at the side facing the ion beam, while excess interstitials remain deeper in the nanowire, see figure 4.10(i,j). As the interstitial-rich material expands and the vacancy-rich material shrinks, the nanowires bends in direction *toward* the ion beam. For both bending directions the curvature increases with fluence, because the number of ion beam induced defects increases with fluence.

Having established a model to explain how bending in the two different direction works, it is now possible to analyze and discuss in more detail the curvature as a function of fluence for the different experimental situations.

4.4.2 Bending and alignment of GaAs nanowires

One observes down-bending away from the ion beam in agreement with the model for the case of low-energy ensemble irradiation of GaAs NWs [see figure 4.4(a)]. However, due to the few data points and large distributions of curvature a more detailed discussion is of little use. For the irradiation of a single GaAs NW in the FIB, one can clearly see that the curvature monotonically increases with fluence, as expected from the model, until the NW begins to decompose as discussed in section 4.3.1. The overall curvature of the single NW is not as strong as for ensemble NWs. This is probably due to a steeper angle of the NW, which perhaps grew in a $\langle 224 \rangle$ -direction instead of $\langle 111 \rangle$, which happens occasionally [Sti08a].

For the high energy irradiation of GaAs NWs, [figure 4.4(b)], one observes in general upward-bending, but a little downward bending occurs first for small fluencies. Indeed, looking at the simulations results for GaAs NW in figure 4.9(i,j), one can see that the distribution of excess interstitials is almost centered. Depending on the exact angle and NW diameter, there may be more interstitials on the side facing the ion beam at first, causing down-bending initially. As the nanowires become thinner due to sputtering, the distribution of damage is shifted deeper into the nanowire. The excess interstitials accumulate on the side facing away from the ion beam and the nanowire bends upward in agreement with the model.

The GaAs NWs become amorphous for high fluencies (typically at the order of $1 \cdot 10^{15}/\text{cm}^2$ or more), as was shown in earlier implantation experiments [Sti08a,Sti08b]. But even in amorphous material, the bending mechanism works for both directions. The amorphous phase has a lower density than crystalline GaAs. In the shallow implantation case, only the material facing the ion beam is amorphized, leading to additional expansion of the material on the side facing the ion beam and thus amplifying the down-bending process. For the deep implantation case, almost all of the nanowire material can be amorphized. However, the forward transport of recoil atoms persists leading to additional expansion of the material on the side facing away of the ion beam and contraction on the side facing the beam, which bends the nanowire upward. The observation that nanowires become aligned with the incident ion beam for high fluencies [see figure 4.2(f)] remains to be explained. As the nanowire is bended upward, the angle between nanowire and ion beam decreases, especially close to the tip of the nanowire, see schematic illustration in figure 4.11(a,b). Thus, the projected range of the ions decreases, which also shifts the damage distribution closer to the side of the nanowire facing the ion beam. Consequently, the situation changes from the deep implantation case to the shallow implantation case, the

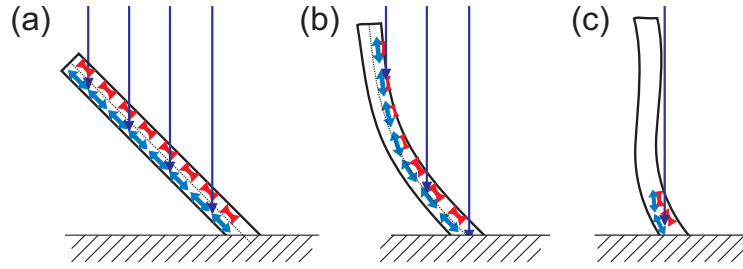


Figure 4.11: Schematic illustration of alignment model. (a) Initially straight nanowire is irradiated homogeneously. Expansion at the bottom side (blue), contraction at top side (red). (b) With bending, angle between ion beam and NW changes, regions of expansion/contraction change, bending at tip reverses. (c) Once aligned, only few ions are implanted. Note, that in the illustration, the NW diameter is increased with respect to length for clarity.

bending momentum is reversed, the curvature decreases, and the nanowire tip is straightened out again. In contrast, the foot of the nanowire is firmly attached to the substrate and the angle between ion beam and nanowire almost stays constant. Here, the upward-bending persists. Depending on how fast the two mechanisms at tip and foot are, this may lead to a point, where the nanowire is relatively straight and almost aligned with the ion beam. In that case the area of the nanowire as seen from the ion beam direction becomes very small. Very few ions hit the nanowire anymore and further bending is very slow, see figure 4.11(c). Consequently, once the NW is in an aligned state with the ion beam it will remain so over a larger fluence range. This persistence once alignment with the ion beam is achieved is also reported for aligning Si nanowires with ion beams [Pec10].

4.4.3 Bending and alignment of ZnO nanowires

The agreement between experimental observations and bending model is more pronounced for irradiation of ZnO nanowires than for GaAs nanowires. In the case of shallow ensemble implantation, see figure 4.6(a), one observes the practically monotonic increase of curvature with ion fluence. Results from 10 keV and 20 keV Ar irradiation are similar within the error bars; the respective damage distributions are similar as well, see figure 4.10(f,g).

The curvature of the single ZnO nanowire irradiated with the FIB is plotted in more detail in figure 4.7(g). The bending proceeds slow at first (1), then becomes faster (2) and finally slows down (3), which can be understood partly by geometric considerations. At first, the nanowire is quite steep and the angle between NW and ion beam is very small. Only few ions are implanted per nanowire length, bending is slow and the angle hardly changes. But with increasing angle, the number of ions implanted per nanowire length increases, and the bending is accelerated until the nanowire is perpendicular to the ion beam. This is the case around $2.5 \cdot 10^{15}$ ions/cm²,

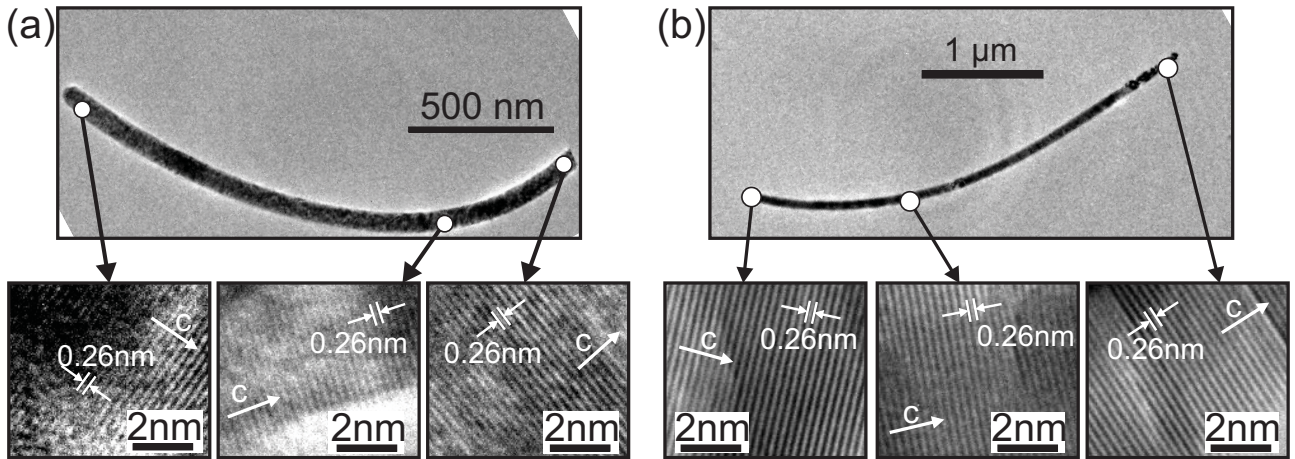


Figure 4.12: TEM images of bent ZnO nanowires after irradiation with 100 keV Ar ions with a fluence of $2 \cdot 10^{16}$ ions/cm². (a) After irradiation, (b) after irradiation and subsequent annealing at 800 °C. HR-TEM images recorded at different locations on the NW show that the *c*-direction is parallel to the NW axis at each point.

corresponding to SEM image 4.7(e). However, with increasing angle, the projected range and concurrently the distribution of defects is shifted away from the NW surface a little deeper into the NW. The bending momentum depends on the distance of the region with excess interstitials from the middle of the nanowire; thus, the additional bending momentum caused by additional damage is reduced, slowing down the further bending. Moreover, this effect is enhanced by thinning of the NW through sputtering.

In the case of deep implantation with high energies, one observes a monotonic increase of curvature as a function of fluence, see figure 4.6(b), in agreement with the bending model. Figure 4.5(g) and (h) illustrate roughly the alignment and straightening of the NW with the incident ion beam as explained above. This alignment is not reflected in the plot in figure 4.6(b), because the curvatures were measured at the point of strongest bending, which is close to the NW foot, as illustrated in figure 4.11.

4.5 Impact of ion irradiation on the crystal structure and the influence of temperature

While the GaAs nanowires become amorphous for high fluencies, this is not the case for ZnO nanowires. Due to the high ionicity of about 1.8, ZnO can hardly be amorphized [Nag75]. The question arises how the crystal structure of the ZnO nanowires is affected by the ion irradiation and how the crystal structure accommodates the bending of the nanowires.

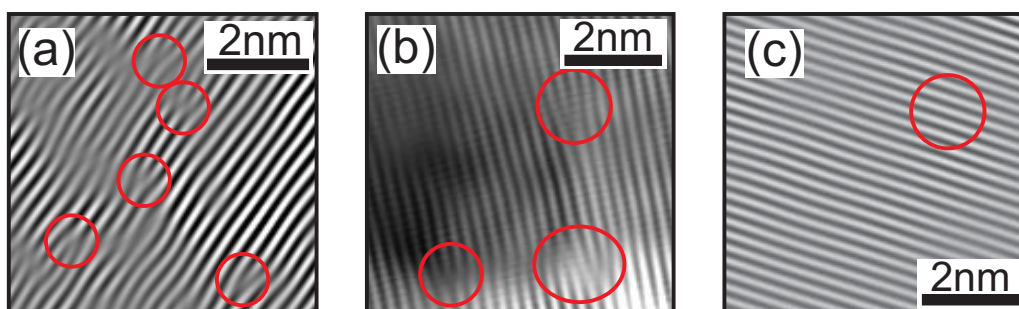


Figure 4.13: Fourier-filtered HR-TEM images of bent ZnO nanowires after irradiation with fluencies of $2 \cdot 10^{16}$ ions/cm². (a) After irradiation with 100 keV Ar ions, (b) after irradiation with 100 keV Ar ions and subsequent annealing at 800 °C, (c) after irradiation with 20 keV Ar ions at 800 °C. Red circles mark positions of dislocations.

The as-grown ZnO nanowires mostly exhibit single-crystalline wurtzite structure and grow in [0001]-direction (or “*c*-direction”) [Bor06]. Figure 4.12(a) shows a TEM image of a single bent ZnO nanowire after irradiation. HR-TEM images were recorded on different points of the nanowire. Fringe patterns with a spacing of 0.26 nm appear in these HR-images. This spacing corresponds to the distance of Zn-planes in *c*-direction (in other words to the [0002] reflex). At each point of the nanowire, these fringes are perpendicular to the local nanowire axis, indicating that the *c*-direction is always parallel to the nanowire and changes gradually along with the nanowire. No grain boundaries were found and the nanowire still consists of one single crystal. Such a bending of the single crystal is associated with strain energy. Upon annealing, point defects become mobile and one might assume that excess vacancies and interstitials can be annihilated or pushed out of the crystal so that the nanowire is straightened again to minimize this strain energy. Increased mobility of point defects and annealing stages in ZnO are observed already between 130 °C and 330 °C, depending on the type of defect [Tuo05]; however, the bending of irradiated ZnO nanowires persists even up to 800 °C as shown in figure 4.8(a). A TEM image of a nanowire bent by irradiation and subsequently annealed at 800 °C is shown in figure 4.12(b). The NW is still bent and the *c*-direction is still parallel with the NW axis at each point.

Consequently, there must exist a mechanism that stabilizes the bending against annealing. Indeed, this can be found in Fourier-filtered HR-TEM images of bent nanowires, see figure 4.13(a). While as-grown nanowires usually exhibit very few dislocations, the bent nanowires exhibit a high density of dislocations (approximately in the order of magnitude of 10^{13} /cm² at the point of strongest curvature). In order to understand how these dislocations are created, we can estimate the tensile or compressive stress in axial direction of the nanowire close to its surface. If one bends a nanowire of 50-100 nm diameter elastically to a curvature of $0.5/\mu\text{m}$,

the axial stress at the surface is about 2-4 GPa (considering an increased Young modulus for ZnO nanowires as compared to bulk [Che06]). These values are still below the yield stress of 7.0 GPa [Ria08], so one would expect that this curvature can still be reached elastically without the creation of dislocations [Che07a]. However, the nucleation of dislocation loops under axial strain is known to be enhanced by ion irradiation due to the introduced point defects and has been observed in ZnO [Wei07, Wen09]. The stress in the bent nanowire changes from compressive on one side to tensile on the other side. In this inhomogeneous stress field, dislocation loops may grow and can move, the movement (climbing) being enhanced by generation of new point defects from the ion beam. If dislocation loops grow and are partly pushed out toward the surface, they can leave behind single edge dislocations, which are observed in figure 4.13(a). The creation and motion of dislocations allows to relax the axial stresses occurring in the nanowires.

It is expected that extended defects like dislocations are only removed from ZnO at temperatures above 1000°C [Kuc03]. The activation energy for dislocation motion in ZnO is around 0.7 to 1.2 eV [Yon09], which is still much more than the thermal energy at 800 °C (≈ 0.09 eV). Nevertheless, additional stress might easily move dislocations at high temperatures; the yield stress at 800 °C is reduced to about 20-30 MPa compared to 7.0 GPa at room temperature [Yon09]. Since the bending of the ZnO nanowires persists at annealing at 800 °C and dislocations are still found after annealing [see figure 4.13(b)], it can be concluded that the stresses occurring in the bent nanowire are indeed mostly relaxed after ion irradiation and before annealing. This finding clearly shows that the nanowire bending by ion irradiation is *plastic* and not *elastic* (as stated above, elastic bending would require stresses at the order of 2-4 GPa).

The bending of ZnO nanowires during high temperature irradiation remains to be discussed, see figure 4.8(b). No difference in the bending was observed from room temperature up to implantation at 700 °C. This finding indicates that the bending is primarily not an effect caused by temperature (i.e. inhomogeneous heating of the NW through irradiation) but indeed a ballistic effect based on damage distribution. If it was a temperature effect, the temperature gradients would probably change with base temperature, and one would observe a dependence of the bending from implantation temperature.

Only when increasing the implantation temperature to 800 °C, the bending is strongly reduced. This means that below 800 °C, the diffusion of point defects must be slower than the creation of dislocations and seems not to be sufficient to balance defects over all the nanowire cross section, although the point defect mobility is already enhanced at temperatures around 130 °C

to 330 °C [Tuo05]. Since the bending is reduced starting at 800 °C, one can assume that the mobility becomes so large that point defects move over larger distances and can annihilate or diffuse to the surface, quickly balancing the inhomogeneous defect distribution introduced by the ion beam, before many dislocations is created. Indeed, TEM images taken from nanowires implanted at 800 °C show only few dislocations; an example is illustrated in figure 4.13(c).

4.6 Dynamic bending calculations in the linear elastic regime

The proposed bending model based on inhomogeneous distribution of excess vacancies and excess interstitials is only qualitative up to this point, except for a rough estimation of stresses to evaluate the possibility to create and move dislocations. In this section, it will be attempted to evaluate the bending model quantitatively by numerically calculating the bending dynamics of nanowires. The basic idea is to obtain damage distributions caused by ion beam irradiation under different angles using *iradina*, see chapter 3. These damage distributions are translated into stress fields, which are forced into the nanowire. From this internal stress field, the bending curve of the nanowire is calculated. It should be noted that standard beam bending theory² cannot be used for this calculation: in simple beam bending theory [Fey64, Ch. 38], external forces are applied to a homogeneous beam and the resulting bending as well as the stress distribution within the beam are calculated. In the present case however, the ions force a specific damage field ($\hat{=}$ initial stress field) into the nanowire and the resulting bending curve needs to be calculated.

For these calculations a simplified linear elastic model of the nanowire is developed. It should be noted that a full calculation of the bending dynamics could be done using finite element methods; however, as the nanowires have a high aspect ratio, only the axial stresses are of interest, and the simple model described here is assumed to be sufficient.

4.6.1 Modeling the nanowire

The nanowire is first assumed to be a cylinder of length L and diameter D with $D \ll L$, see figure 4.14(a). The nanowire is divided into n cylindrical segments indexed by s with initial lengths $l_s = L/n$, see figure 4.14(b). Each segment is further divided into a number of rectangular-shaped elements (long thin rods), see figure 4.14(c). If a sufficiently large number

²Here, “beam” must not be confused with “ion beam”. It means something like “bar” here (“beam bending theory” in German is “Theorie der Balkenbiegung”).

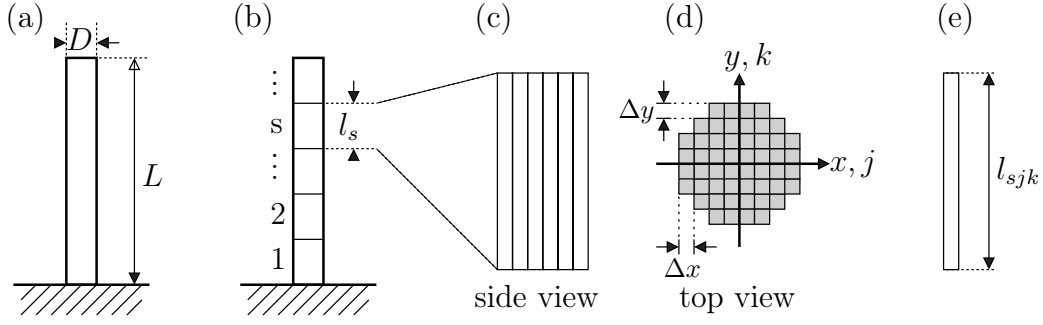


Figure 4.14: Schematic illustration of nanowire model: (a) Nanowire of length L and diameter D . (b) The NW is divided into nearly cylindrical segments indexed by s with lengths l_s . (c) Each segment s is further divided into elements. (d) These elements are numbered by the two in-plane indices j and k . (e) The length of each element is designated by l_{sjk} .

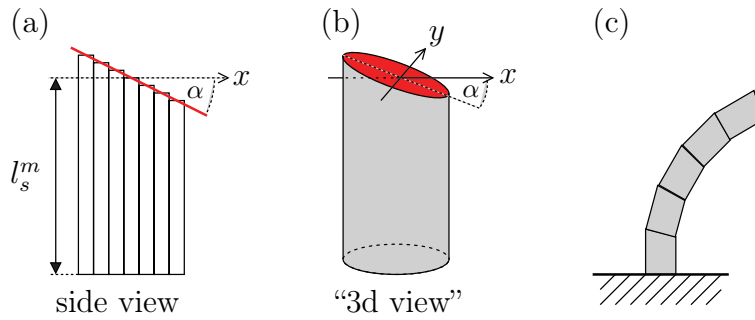


Figure 4.15: Schematic illustration how bending is modeled: (a) The elements of one segment form a plane end-cap (marked in red). (b) The end-cap of a segment is tilted by an angle of α with respect to the x -axis. (c) The combined segments represent a bent nanowire.

of elements is used (i.e. 40×40), the cylinder can be well approximated as shown in “top view” in figure 4.14(d). The elements within one segment are indexed using j, k and the positions within the plane can be calculated by $x = j \cdot \Delta x$ and $y = k \cdot \Delta y$.

Next, the bending of a nanowire needs to be represented in the model. Therefore, we take a closer look at one arbitrary segment s . One can assume that the length l_{sjk} of each element within the segment can be changed, depending on the local stress induced by the ion beam. For simplification, the width Δx and depth Δy of the all elements are assumed to remain constant. As the elements are tightly bound together to form the segment, the elements’ lengths cannot be changed independently: to ensure material integrity the elements are assumed to form up a plane end-cap of the segment, as illustrated in figure 4.15(a,b).

The plane end-cap of the segment is characterized by three parameters: the tilt angle α_s with respect to the x -axis, the tilt angle β_s with respect to the y -axis (not illustrated for the sake of clarity) and the mean segment length l_s^m . The complete nanowire in its bent state is formed by

subsequently “mounting” each segment s on the plane end-cap of the previous segment $s - 1$, as illustrated schematically in figure 4.15(c).

Next, we consider the stress induced in the nanowire by the ion beam. The ion beam irradiation of a segment of the nanowire is simulated using *iradina*, see chapter 3. In the simulations, each simulation cell corresponds exactly to one element (jk). The simulation yields the distributions of the various interstitials and vacancies within the nanowire. In each cell (and for each element) the difference value of interstitials minus vacancies is calculated assuming annihilation of defects (as described above). This can lead to compressive or tensile stress within each element (details how the damage is converted to stress are discussed in section 4.6.4). Simulations are done for all segments yielding stress values σ_{sjk} for all elements of the nanowire. These stresses will lead to a bending of the nanowire.

4.6.2 Calculation of bending

At first, one individual segment s will be considered. After a certain field of stress σ has been induced in the segment, we need to calculate the resulting length l_s^m and the tilt angles α_s and β_s of the plane end cap of that segment. To do this, let us first assume that all elements of a segment were independent and not connected. Then their lengths would change purely because of the induced local stress σ_{sjk} . We denote the length which each free element (sjk) would like to assume as the “relaxed length” $l_{sjk}^r = l_s^0 \cdot (1 + \sigma_{sjk}/Y_{jk}^c)$, where Y_{jk}^c is the Young’s modulus of the material (in c -direction for ZnO)³. However, in reality the elements are parts of one solid. We force all elements of one segment together by choosing their lengths such that they reach a common plane end-cap as described above. The forced length of each element shall be l_{sjk}^f . Each element will thus be strained and the strain energy depends on the difference between relaxed and forced length $\Delta l_{sjk} = l_{sjk}^r - l_{sjk}^f$. The strain energy is $E_{sjk} = (\Delta l_{sjk})^2 \cdot Y_{jk}^c$. The length and the strain energy of each element now depend on the end-cap, or more specifically on the mean segment length l_s^m and the tilt angles α_s and β_s . Thus, the complete strain energy of the segment (which is the sum of all its elements’ strain energies) can be expressed as a function of these three parameters: $E_s = E_s(l_s^m, \alpha_s, \beta_s)$. The nanowire will bend in such a way as to minimize this total strain energy E_s . The parameters l_s^m , α_s and β_s can thus be found

³The Young’s modulus may depend on the element index, because close to the surface it differs from the bulk value [Che06].

by minimizing E_s with respect to these three parameters. Doing this leads to the following set of equations (the derivation being shown in appendix C):

$$\begin{aligned}
 \sum_{jk} Y_{jk}^c \cdot (l_s^m - l_{sjk}^r - j \cdot \Delta x \cdot \tan \alpha_s - k \cdot \Delta y \cdot \tan \beta_s) &\stackrel{!}{=} 0 \\
 \sum_{jk} Y_{jk}^c \cdot j \cdot (l_s^m - l_{sjk}^r - j \cdot \Delta x \cdot \tan \alpha_s - k \cdot \Delta y \cdot \tan \beta_s) &\stackrel{!}{=} 0 \\
 \sum_{jk} Y_{jk}^c \cdot k \cdot (l_s^m - l_{sjk}^r - j \cdot \Delta x \cdot \tan \alpha_s - k \cdot \Delta y \cdot \tan \beta_s) &\stackrel{!}{=} 0
 \end{aligned} \tag{4.1}$$

Instead of minimizing the energy, the same conditions can also be derived by requiring that the sum of all forces as well as the sum of all angular momenta acting on the end plane vanish.

The set of equations 4.1 is solved numerically by using Newton's method [Got95, p.681], details are shown in appendix C. The solution tells us how the end-cap of the segment s is tilted for any given distribution of stress. To calculate the complete shape of the nanowire, one simply needs to calculate the length and tilt angles of each segment and assemble them to form a nanowire as illustrated in figure 4.15(c).

4.6.3 The dynamics of the bending

In order to calculate the *dynamics* of NW bending under ion beam irradiation, the virtual nanowire is irradiated step by step with small fluencies. Between each step, the bending of the nanowire is calculated. In each irradiation step, all the angles between ion beam and nanowire axis may be different for all the segments, which poses a problem in terms of efficiency: for the *iradina* simulations, the angle between ion beam and nanowire must be known. However, it would take far too much time to fully simulate the irradiation of all segments in between all steps. Thus, before the calculation of the bending begins, simulations are made with *iradina* for 20 different incidence angles. All simulation results are loaded to memory and then, for irradiating a segment during the dynamic calculation, the *iradina* simulation is used with the angle that is closest to the correct angle.

The errors made by this approximation are estimated to be small, because the differences in implantation profiles between two adjacent angles are small. This is ensured by not distributing the incidence angles evenly but distributing their cosines evenly: whether the ion beam hits the nanowire perpendicular or 10° off perpendicular direction does not make much of a difference; but whether the ion beam is parallel to the NW or 10° off the axis makes a huge difference.

4.6.4 Bending of ZnO nanowires

Translating damage to stress

In the qualitative model it was simply assumed that excess interstitials cause expansion and excess vacancies cause contraction of the material. However, such an approach is too simple for ZnO for several reasons: the formation volumes for Zn and O interstitials and vacancies are different, and the formation volumes depend strongly on the charge state of the defects, due to the high ionicity of ZnO. In fact, some type of vacancies can even cause expansion of the material, and interstitials can cause contraction. Erhart *et al.* have made first-principle studies of defects in ZnO from which the formation volumes of the different defect types can be determined [Erh05,Erh06]. The values are listed in appendix C.

The following steps are performed to calculate the expansion or contraction caused by damage obtained from *iradina* simulations: Zn interstitials and Zn vacancies are assumed to annihilate in each simulation cell, and separately, O interstitials and O vacancies are assumed to annihilate within each simulation cell. “Cross-annihilation” of defects from different elements is not taken into account, because the formation energies of antisites are higher than of other defects in ZnO [Koh00] and they are thus less likely to occur. The Monte Carlo simulations cannot distinguish between the different types of oxygen interstitials that occur in ZnO (octahedral and dumb-bell interstitials), thus an average value for the formation volume has to be used. Furthermore, the charge states of the defects in the nanowires are not known. One can determine probable charge states of the various defect types by using the energy diagram of the ZnO band gap from reference [Erh06, fig. 6c], see also figure C.1 in appendix C, which shows the various energy levels for all the charge states of each defect type. However, it is not known at which position the Fermi level is within the band gap for such heavily damaged NW material. Assuming that the Fermi energy level is approximately in the middle of the band gap (Position A in figure C.1), one obtains the average formation volumes: zinc interstitials: $V_f^{Zn,i} = -0.30$, zinc vacancies: $V_f^{Zn,v} = 0.45$, oxygen interstitials: $V_f^{O,i} = 0.53$, and oxygen vacancies: $V_f^{O,v} = -0.32$ in units of the ZnO formula volume ($=2.41 \cdot 10^{-22} \text{ cm}^3$).

The numbers n of excess defects of each type after annihilation are counted in each element (sjk) of the nanowire segment and the defects are assumed to cause an isotropic expansion or contraction of the volume of that element:

$$\Delta V_{sjk} = n_{sjk}^{Zn,i} \cdot V_f^{Zn,i} + n_{sjk}^{Zn,v} \cdot V_f^{Zn,v} + n_{sjk}^{O,i} \cdot V_f^{O,i} + n_{sjk}^{O,v} \cdot V_f^{O,v}$$

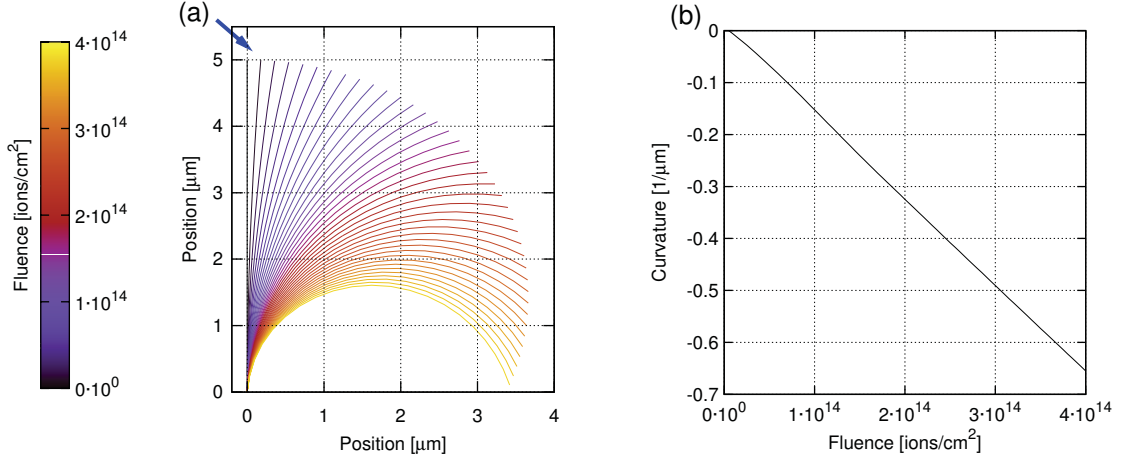


Figure 4.16: Results of dynamic bending calculation. (a) shows the shape of a ZnO nanowire, bending with increasing ion fluence (color-coded) of 10 keV Ar irradiation (50 nm diameter, 20 segments, 5 μm length, fluence steps of $5 \cdot 10^{12}$ ions/cm²). Blue arrow shows ion beam direction. (b) shows the maximum curvature of the nanowire as a function of fluence.

Either $n_{sjk}^{Zn,i}$ or $n_{sjk}^{Zn,v}$ must vanish, the same is true for oxygen. From the change in volume, the change in length of each element can be calculated, which leads to the above mentioned “relaxed length” l_{sjk}^r . However, if the element is not allowed to relax, it is stressed and the corresponding value for the *ion beam induced stress* is: $\sigma_{sjk} = (l_{sjk}^r/l_{sjk}^0 - 1) \cdot Y_{jk}^c$, where l_{sjk}^0 is the length of the undamaged element. As explained above, relaxation is done in such a way as to minimize the total strain energy of a segment of the nanowire.

Calculation results

Dynamic bending calculations were done for various situations corresponding to the experiments. Figure 4.16 shows the bending of a ZnO nanowire under 10 keV Ar irradiation comparable with the experimental situation shown in figure 4.6. Initially, the NW is perpendicular and straight. With increasing ion fluence (ions coming from the left), the NW bends away from the ion beam, down toward the substrate. However, the bending in the simulation proceeds about 33 times faster than observed in the experiment: in the simulation the curvature reaches $-0.5/\mu\text{m}$ at an ion fluence of about $3 \cdot 10^{14}/\text{cm}^2$, while in the experiments about $1 \cdot 10^{16}/\text{cm}^2$ are required. For the simulations it was simply assumed that defects annihilate only within each simulation cell (in this case, the lateral cell size is only $1.25 \times 1.25 \text{ nm}^2$). In reality, annihilation of defects by dynamic annealing might be more effective, explaining why higher ion fluencies are required to reach the same curvature. Furthermore, exact values for the displacement energies in ZnO are not known (for the simulations, $E_D(\text{Zn})=18.5 \text{ eV}$ and $E_D(\text{O})=41.4 \text{ eV}$ were used [Loo99]).

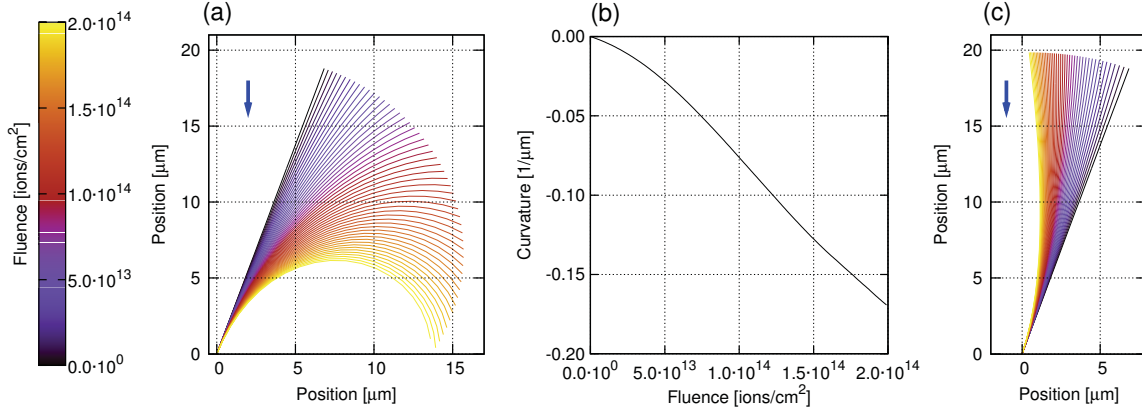


Figure 4.17: Results of dynamic bending calculation. (a) The shape of the nanowire is shown as a function of fluence (color-coded). Parameters are 30 keV Ga irradiation, 80 nm diameter, 20 segments, 20 μm length. Blue arrows show ion beam direction. (b) Maximum curvature as a function of fluence. While (a) shows the bending of NW for E_F in middle of band gap, (c) shows the bending for E_F close to the valence band.

Figure 4.17 illustrates the bending of a ZnO nanowire under 30 keV Ga irradiation, comparable to the experimental situation shown in figure 4.7. Subfigure (a) shows the bending for the Fermi level approximately in the middle of the band gap as used above. The NW bends away from the ion beam, down toward the substrate like observed in the experiment. Figure 4.17(b) illustrates the curvature as a function of fluence. Again, one observes that the bending in the simulation proceeds much faster than in the experiment, due to less effective annihilation of defects as explained above. A division into three fluence ranges with slow, faster and slower bending was observed in the experiment [figure 4.7(g)]. The simulation results reproduce this effect, albeit somewhat weaker.

Figure 4.18 illustrates calculation results for bending of ZnO nanowires irradiated with 100 keV Ar ions (deep implantation case), comparable to the experimental situation shown in figure 4.5(e-h) and 4.6(b). In figure 4.18(a) one can observe that the simulated NW bends *away* from the ion beam in contrast to the experiments, where the nanowires were bent *toward* the ion beam. In order to investigate, whether this might be due to a wrongly selected Fermi level, simulations were done for two other Fermi levels leading to different charge states and to different formation volumes of the various defects [figures 4.18(b) and (c)]. When a Fermi level of $0.15 \cdot E_G$ above the valence band is selected [4.18(c)], the NW bends in direction toward the ion beam as observed in the experiment. In this case, one can also observe the alignment effect: at first, the bending increases with fluence, but as the NW becomes increasingly aligned with the ion beam, the bending slows down, and the bending direction at the tip of the nanowire is reversed.

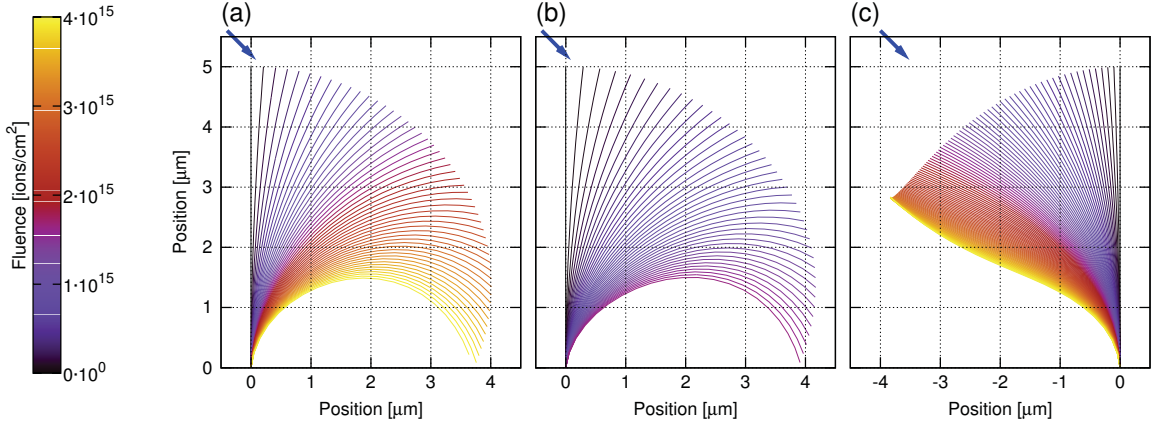


Figure 4.18: Results of dynamic bending calculation. The shape of the nanowire is shown as a function of fluence (color-coded) for three different Fermi energy levels. (100 keV Ar irradiation, 90 nm diameter, 20 segments, 5 μm length, fluence steps of $2 \cdot 10^{13}$ ions/cm 2). Blue arrows show ion beam direction. (a) E_F in middle of band gap, (b) close to CB, (c) close to VB; compare with figure C.1.

However, ZnO is almost always n-type; thus, such a low Fermi level close to the valence band is quite unlikely. Furthermore, this low Fermi level of $0.15 \cdot E_G$ above the valence band is not consistent with the case of low energy irradiation: Figure 4.17(c) shows the bending of a ZnO nanowire under 30 keV Ga irradiation for this low Fermi level. In this case, the NW bends towards the ion beam direction, as opposed to the experimental observation, where the NW bends down. No consistent Fermi level was found that reproduces both cases correctly.

An unrealistically high concentration of vacancies occurred close to the NW surface in the *iradina* simulations, as discussed in section 4.4. Bending simulations were made, in which the surface part of the nanowires was ignored (calculations limited to material within 90% of NW radius) in order to exclude a major impact from these surface effects. However, the results did not change much and the inconsistency of the bending directions could not be resolved.

The inconsistent bending directions are therefore ascribed to the fact that too many approximations and inaccuracies are included in the dynamic bending calculations: One important source of error are the charge states and formation volumes obtained from the first-principle studies of ZnO [Erh05, Erh06]. Experimental confirmation of those results is not available. The calculations result in a band gap of 1.83 eV as opposed to the experimentally observed 3.4 eV in ZnO, and all values for transition levels must be extrapolated to the experimental band gap. Furthermore, defect formation volumes and charge states are calculated for isolated defects (more precisely, the values are extrapolated from finite periodic supercells to infinite dilution,

which causes quite some uncertainty). The high defect densities in the experiment may lead to formation of impurity bands, changes in the charge state distribution and changes in the formation volumes. Furthermore, the Fermi level may be pinned at the surface of the nanowire, leading to band bending and inhomogeneous charge state distribution of the defects throughout the nanowire. Further approximations are made by the dynamic model itself: linearity of defect concentration with ion fluence as well as linear elasticity are assumed. The occurrence of dislocations clearly shows that this assumption is invalid for high fluencies. Additionally, the NW diameter is assumed to be constant, while in reality the NW is thinned by sputtering.

It is possible to find parameters for each case of irradiation that allow to reproduce the experimental observations with the dynamic bending calculations; but due to the inconsistencies caused by the many assumptions and approximations, it must be concluded that the model presented here cannot be used to predict the bending of nanowires for arbitrary other irradiation parameters.

Future improvements may be possible by calculating the irradiation itself dynamically, meaning that the nanowire is allowed to change its shape and composition. This could also eliminate the problem of sputtering at the NW surface. However, *iradina* is currently a static code and cannot be used for such calculations.

4.6.5 Bending of GaAs nanowires

In contrast to ZnO, no values for the formation volumes of defects in GaAs were found in the literature. But one can find calculated values for the volume relaxation of the tetraeders formed by the four neighboring atoms of a defect in GaAs [Seo95, Sta01, Mal07]. These volume relaxations can be used as an approximation for the expansion or reduction caused by each defect type; detailed values are listed in appendix C. Since GaAs is less ionic than ZnO, the formation of antisites is more probable. This is accounted for in the calculations for GaAs NWs: first, the interstitials and vacancies of each type are allowed to annihilate within each simulation cell (like for ZnO). Subsequently, “cross annihilation” of Ga and As defects is performed, meaning that if there is an excess of As vacancies and Ga interstitials, they annihilate to Ga_{As} antisites and vice versa. The tetraeder volume relaxation of the various defects in GaAs does not show a strong dependence on the charge state, as opposed to ZnO. Only As vacancies and Ga_{As} antisites shows a little dependence [Seo95]; thus, for these defects the charge states is selected for a Fermi level approximately in the center of the band gap, value taken from [Sch09a].

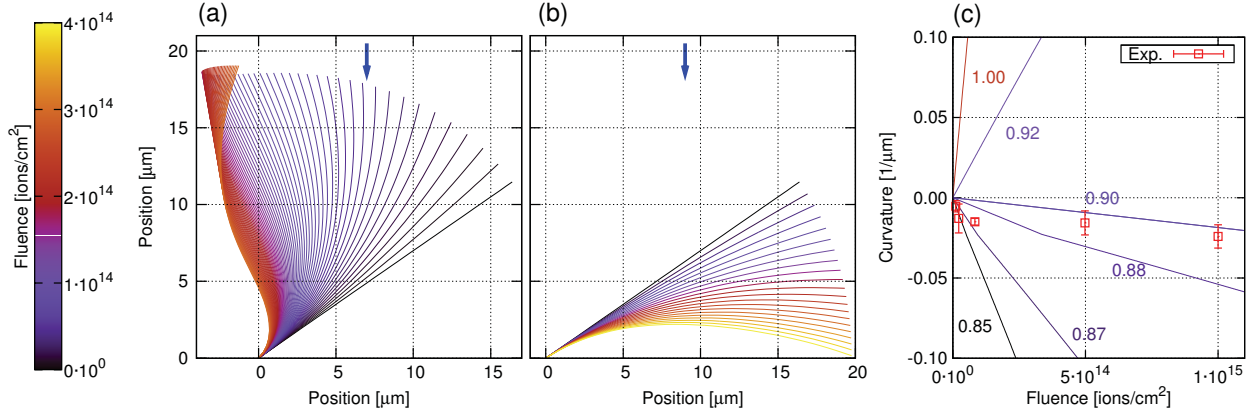


Figure 4.19: Results of dynamic bending calculation for GaAs nanowires of 150 nm diameter, 20 μm long, 40 segments, irradiated with 35 keV Ar. (a) shows the shape of the nanowires as a function of fluence (color-coded) if the full cross section is taken into account, blue arrow shows direction of ion beam. (b) shows the evolution of nanowire shape if the diameter is cut off at 87%. (c) shows the maximum curvature of the nanowire as a function of fluence for different cut-off values, as well as the experimentally observed curvature.

An increased Young modulus of GaAs nanowires is taken into account in the calculations: Wang *et al.* recently studied the size dependence of the Young modulus of GaAs nanowires by combining mechanical bending experiments (and *in-situ* TEM observation) with finite element analysis of the bent NWs [Wan11]. They obtain a young modulus of 118 GPa for GaAs NWs of 150 nm diameter (compared to the bulk value of 86 GPa).

Calculation results

Figure 4.19(a) illustrates the calculated bending results for irradiation of GaAs NWs with 35 keV Ar (situation of shallow implantation). As opposed to the experiment, the nanowire bends upward in the simulation (compare to figure 4.2(a-c)). The problem here may be the strong excess of vacancies that occurs close to the nanowire surface in the results from *iradina* (figure 4.9), which is not realistic as explained in section 4.4. In order to monitor the influence of this effect, bending calculations were also made where the cells close to the nanowire surface were ignored. Figure 4.19(b) illustrates the evolution of the nanowire shape for a cut-off radius of 87%, meaning that all material outside this cut-off radius is ignored in the bending calculation. The cut-off results in the correct bending direction of the nanowire down toward the surface. Calculations were made for different cut-off values and the resulting maximum curvature of the nanowires is shown as a function of fluence in figure 4.19(c). The direction of the curvature as well as its dependence on fluence vary strongly with the selected cut-off radius. For the lower fluencies ($< 2 \cdot 10^{14}/\text{cm}^2$), a cut-off of 87% is in reasonable agreement with the experimentally

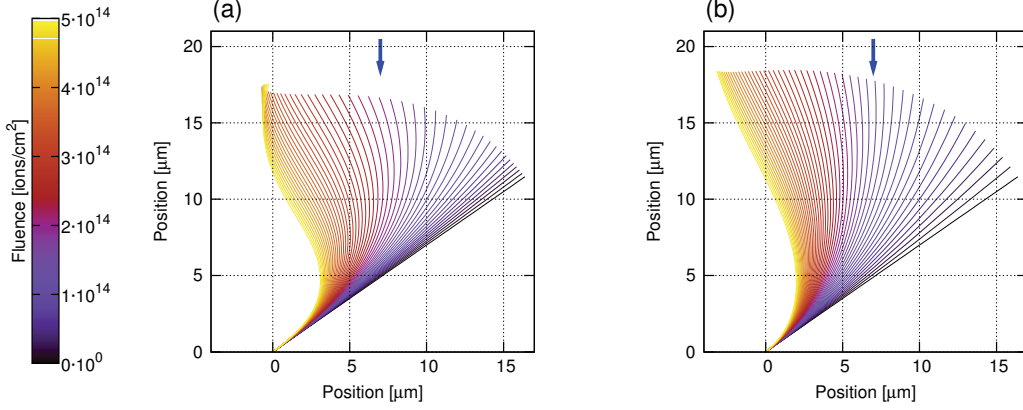


Figure 4.20: Results of dynamic bending calculation for GaAs nanowires of 150 nm diameter, 20 μm long, 40 segments, irradiated with 210 keV Ar. (a) shows the shape of the nanowires as a function of fluence (color-coded) if the full cross section is taken into account. (b) shows the evolution of nanowire shape if the diameter is cut off at 87%.

observed maximum curvatures. For higher fluencies, a somewhat larger cut-off radius would fit better to the curvature; but at these larger cut-off radii, the nanowire tips start to bend upwards in the bending simulations (not shown), which is not observed in the experiments. Thus, it must be concluded that the cut-off procedure is too simple and cannot be used to consistently fit the calculations to the experimental observations.

Results of the bending calculations for irradiation with 210 keV Ar ions (deep implantation) are illustrated in figure 4.20. The calculated shape of the nanowire after irradiation with $5 \cdot 10^{14}$ ions/cm² is remarkably similar to the experimentally observed shape after irradiation with $1 \cdot 10^{15}$ ions/cm² [see figure 4.2(f)]. The factor of about 2 between calculation and experiment shows that the annihilation of defects is probably more effective in reality than in the simulation. Note that for ZnO, this factor is about 33 (see section 4.6.4) resembling the fact that ZnO is more ionic and thus more resistant to radiation than GaAs. Incidentally, the lower ionicity of GaAs poses an additional problem: while ZnO nanowires remain crystalline, the GaAs nanowires can be amorphized during irradiation, which changes the mechanical properties of the nanowires. This is not taken into account by the bending calculations.

Calculations for the deep implantation case were also made with different cut-off radii, in order to check consistency with the low-energy irradiation. The result for a cut-off radius of 87% is shown in figure 4.20(b). Obviously, the cut-off has much less effect for the high energy irradiation than for the low energy irradiation. This is no surprise considering that the simulated defect distribution for 210 keV Ar is not so much dominated by near-surface defects [see figure 4.9(i)].

In general, one finds a similar conclusion for the GaAs as for the ZnO nanowires: although it is possible to reproduce the experimental observations with the dynamic bending calculations, there are too many assumptions and approximations to allow reliable predictions of nanowire bending for arbitrary other irradiation parameters.

4.7 Summary and conclusion

Ion beam induced bending of GaAs and ZnO nanowires was investigated. Ensembles of nanowires were irradiated with unfocused ion beams mostly of noble gas ions. When the ion range is much smaller than the NW diameter, the nanowires bend away from the ion beam direction, the curvature increasing with ion fluence. For the case of higher ion energies, when the ion range becomes comparable to the NW diameter, the nanowires bend toward the ion beam and it is possible to align the nanowires with the incident ion beam direction. Single nanowires were irradiated with Ga ions in a FIB and the bending could be monitored in detail by *in-situ* observation with the attached SEM column. However, only the low energy case could be studied, as the ion energy was limited to 30 keV. Like for low energy Ar irradiation, the nanowires were bent away from the Ga ion beam.

The bending can be explained by an inhomogeneous distribution of defects over the nanowire cross section, which can be obtained from *iradina* simulations. In the low energy case, all defects remain on the irradiated side, causing expansion of the material and a bending momentum away from the beam. In the high energy case, defects are created all over the nanowire; however, an excess of vacancies accumulates at the irradiated side while an excess of interstitials accumulates on the other side, because the interstitials are transported forwards and vacancies are left behind. This inhomogeneous distribution causes contraction on the irradiated side and expansion on the back side, leading to a bending momentum toward the ion beam.

GaAs nanowires were amorphized during irradiation [Sti08b,Sti08a], but in contrast, the ZnO nanowires remained crystalline, as shown by HR-TEM investigations. This finding supports the hypothesis that the inhomogeneous distribution of ion beam induced defects is indeed the driving force for bending in these experiments, in contrast to the observations reported by the Catania group attributing the bending of Ge and Si nanowires to amorphization [Rom09, Pec10, Pec11]. Detailed analysis of the crystalline structure reveals that the *c*-axis is parallel to the NW axis at each point of the bent nanowire. This gradual change in crystal orientation is achieved by dislocations. The stresses expected from the curvatures are not sufficient to

explain the onset of dislocations alone, but the ion beam irradiation enhances their production and movement. These dislocations relax the stresses in the nanowire and stabilize the bent state during post-irradiation annealing: the NW curvature remains constant up to 800 °C. Carbon-induced decomposition occurs at higher temperatures.

In order to investigate the influence of temperature during the bending process, nanowires were irradiated at elevated temperatures up to 800 °C. The bending of the nanowires does not change from RT up to 700 °C, indicating that the bending is not a temperature effect. However, the bending becomes significantly less for irradiation at 800 °C. Here, the mobility of point defects becomes so large that defect annihilation is possible over larger distances and the inhomogeneous defect distribution can partly be balanced. This is an important result for ion beam doping of ZnO nanowires, because implantation at 800 °C can be used to avoid undesired bending of the nanowires. Furthermore, the lower density of dislocations occurring during irradiation at 800 °C is advantageous, because dislocations in ZnO are known to decrease the electron mobility [Miy04]. On the other hand, one has to make sure that no out-diffusion of the dopants occurs. For ion beam implantation of rare earth elements, temperatures above 750 °C begin to be problematic [Geb08a].

Attempts were made to calculate the bending of nanowires under ion irradiation dynamically. A simple linear elastic model of a nanowire was established and simulation results from *iradina* were used as input parameters to obtain the distribution of ion-beam induced stresses in the nanowire. The simulated bending as a function of fluence increases faster than in the experiments, showing that defect annihilation is very effective. This may be expected due to the enhanced dynamic annealing observed for nanowires. For each irradiation case, parameters can be found that lead to agreement between the simulated and experimentally observed bending. However, the parameters are inconsistent between various irradiation conditions; which is not totally unexpected, considering all the assumptions and approximations made in the model. In conclusion, the model cannot be used for reliable predictions of NW bending.

Nevertheless, the experiments demonstrate a way to achieve bending and alignment of semiconductor nanowires independent of the growth method. Mechanical deformation of nanostructures by external forces has to overcome large elasticities before permanent deformation can be achieved [Che07a]. In contrast, ion beam irradiation easily allows permanent plastic deformation of the nanostructures. Simultaneous doping of semiconductor nanostructures may be achieved by selecting appropriate ions. Furthermore, ion beam irradiation of wafer-scale targets is possible, allowing to align large numbers of nanostructures in parallel.

Chapter 5

Manganese Doping of GaAs Nanowires

The experiments described in this chapter were done in close collaboration with the group of Prof. Lars Samuelson and Prof. Håkan Pettersson from Lund in Sweden. Parts of the results are published in [Bor11a].

5.1 Motivation - diluted magnetic semiconductors for spintronics

Today's information processing and microelectronics is based on semiconductors. The success of semiconductors is based on several key elements. Their electrical properties can be controlled by doping, which allows to adjust the conductivity over many orders of magnitude. Furthermore, like in a field effect transistor (FET), it is possible to electrically control the concentration of charge carriers and with that the conductivity by applying a gate bias. In today's microelectronic devices, the charge carriers are not spin-polarized and the spin degree of freedom is not used for the transport or processing of information. It is used though in permanent magnetic data storage, where information is stored as magnetization. Spin-dependent effects are used for reading the data via the giant magnetoresistance effect [Bai88, Bin89].

Microelectronic device concepts, which make use of the electron spin in addition to conventional use of the electron charge, are summarized in the term "spintronics". An example for such a device, which features new functionality compared to conventional electronics, is a "spin-FET". For example, it shows an oscillating output current as a function of gate bias due to spin precession of spin-polarized charge carrier in the FET channel [Dat90, Sug10].

In general, the requirements for useful applications of such devices can be summarized compactly by quoting H. Ohno: "*One has to be able to create, sustain, control and detect the spin polarization of carriers.*" [Ohn98]. To control the spin polarization, splitting of the energy levels for charge carriers of the two different spin states is desired. In non-magnetic semicon-

ductors, unusefully large external magnetic fields would be required to achieve any significant splitting [Ohn98]. But sufficient energy splitting could be achieved with *magnetic* semiconductors. There exist intrinsically ferromagnetic semiconductors (for example the europium-chalcogenides [Mau86]); however, they are not useful for spintronic applications for several reasons: they are difficult to grow in high quality and they are incompatible to standard semiconductor technology. Much more useful is the possibility to make technologically established but intrinsically non-magnetic semiconductors, like Si or GaAs, ferromagnetic. This takes us to the concept of a *diluted magnetic semiconductor* (DMS).

While in pure transition metals ferromagnetism can be described well in a band model, the magnetism in a DMS is better understood in a model based on localized magnetic moments. Basically two conditions must be fulfilled for ferromagnetism to occur: First, unpaired spins are required, which provide the magnetic moments, and second, a coupling mechanism must exist, which makes parallel orientation of the unpaired spins energetically favorable. Unpaired spins can be provided by 3d-transition metal (TM) atoms, which are incorporated into the semiconductor host matrix (these are the “diluted” magnetic atoms of the “DMS”). A Mn atom for example provides a spin of $5/2$ from the five electrons in the 3d sub-shell with parallel spins. Coupling between the unpaired spins from various atoms is achieved indirectly via the free charge carriers in the semiconductor. In case of Mn doped GaAs, this coupling can roughly be described by the Rudermann-Kittel-Kasuya-Yosida (RKKY) interaction [Yos57, Ohn98]: simply speaking, a local magnetic moment (from one TM atom) spin-polarizes the surrounding charge carriers via exchange coupling. The polarized charge carriers then interact with other localized magnetic moments (other TM atoms) again via exchange coupling. Thus, the spins of the TM atoms are indirectly coupled. Since the spin polarization of charge carriers oscillates, the RKKY coupling can be ferromagnetic or antiferromagnetic depending on the distance between neighboring TM atoms, the host material and the charge carrier concentration. Ferromagnetic DMS have been achieved by Mn-doping of various III-V [Ohn99], II-VI [Fur88], as well as group IV [Par02] semiconductors.

In thin films of highly Mn doped GaAs, ferromagnetism has been observed for Mn concentrations in the order of a few percent [Ohn96, Esc97]. The Mn atoms provide the spins as well as the charge carriers, because they act as acceptors when substitutionally incorporated on Ga sites. However, the solubility limits of transition metals in III-V semiconductors are low and the only possibility to obtain ferromagnetic GaMnAs is by non-equilibrium growth techniques, for example low temperature MBE at 250 °C [Ohn96]. When using higher growth temper-

atures or subsequent annealing, higher doping levels are achieved, but segregation of MnAs clusters occurs [Boe96, Wel97]. These MnAs clusters are ferromagnetic; thus, GaAs with MnAs clusters may exhibit ferromagnetism on a macroscopic scale. There are several applications of MnAs clusters embedded in a GaAs host matrix [Wel97, Mor03, Hai07, Hai09]; however, this is not a DMS, the coupling of spins is not carrier-mediated and thus, the magnetism cannot be controlled electrically.

The low solubility limit of transition metals in III-V semiconductors (typically below 0.1%¹ [DeS82]) at thermal equilibrium makes it especially difficult to create DMS GaMnAs nanowires, because the growth of nanowires requires higher temperatures than in low-temperature MBE for thin films. However, various attempts have been reported: Successful growth of InGaMnAs NWs by migration enhanced epitaxy was reported by Sadowsky *et al.* in 2002 [Sad02]. They also reported on growth of Ga_{1-x}Mn_xAs NWs using MnAs nanoclusters as growth seeds [Sad07]. Manganese concentrations in the nanowires up to 7% were obtained, but the NW were strongly tapered and exhibited irregular side facets. Additionally, the high Mn content can lead to branching of the NWs [Dlu09]. Another attempt to obtain highly Mn doped GaAs NW is to use Mn-assisted growth [Mar06].

Room temperature ferromagnetism in Ga_{1-x}Mn_xAs nanowires with low Mn content (<5%) has been reported by Kim *et al.*, who grew the nanowires via vapor transport [Kim09]. However, the magnetic properties are questionable, because there is no mechanism that could explain the high T_C values [Rud09]. Some reports even show room temperature ferromagnetism of GaMnAs nanowires with Mn concentrations of 20% [Jeo07]. However, at these concentrations one does not have diluted Mn in a GaAs matrix, but rather a new compound or possibly ferromagnetic MnAs clusters. In other approaches, non-homogeneous structures were created on purpose by combining a GaAs nanowire with a GaMnAs shell [Rud09] or decorating GaAs nanowires with MnAs nanoparticles [Wol11].

The problem with most of the reported attempts to create highly Mn-doped GaAs nanowires is the segregation of the MnAs phase during growth. This is not unexpected, because, according to the phase diagram determined by Ohno for Ga_{1-x}Mn_xAs layer growth via MBE [Ohn99], MnAs forms above about 300 °C for x in the order of 0.5% to 6%. A GaAs nanowire with small segregated ferromagnetic MnAs nanoclusters can easily be mistaken for a DMS. It has been reported that the detection of small MnAs nanoclusters in GaAs with XRD or HR-

¹Here, % always refers to the atomic fraction, not the mass fraction.

TEM is rather challenging [Seo04]. Even if no MnAs clusters segregate, the Mn might not incorporate homogeneously in the NWs, but for example accumulate in a shell. This effect has been seen directly for doped Ge nanowires by tomographic atom probe measurements [Per09]. In conclusion, growing highly Mn doped homogeneous GaAs nanowires is a challenging issue. The possibility to incorporate Mn *after* growth remains. However, any diffusion based approach will fail due to the low solubility limit; only hyper-thermal doping has a prospect of success, which is why ion beam implantation comes into play at this point. Ion beam implantation can in principle be used to incorporate any element into any material beyond any solubility limit. However, due to the introduced defects, post-implantation annealing is usually required. For Mn ion implantation of GaAs thin films, thermal annealing at 650 °C has been reported to lead to MnAs cluster formation [Bür09]. Only non-equilibrium annealing, like pulsed laser melting [Sca03, Sca08] and ion beam-induced epitaxial crystallization annealing [Che09] have shown promising results regarding the incorporation of Mn in GaAs to create DMS systems. Regarding nanowires, it must be noted that the annealing methods known from bulk material cannot be directly adapted in most cases. The reason is that the nanostructures are often not the equilibrium form of the material and the large surface-to-volume ratio may lead to lower melting points compared to bulk counterparts. Nevertheless, examples of successful doping by ion beam implantation and subsequent annealing exist for GaAs nanowires: for example, it has been shown that p-type doping was achieved by ion beam implantation of Zn and subsequent annealing at 800 °C under tertiarybutylarsine atmosphere [Sti08b]. In the scope of this thesis, possibilities to create highly Mn doped GaAs nanowires by ion beam implantation and annealing were evaluated. In this context two approaches are compared: (1) ion beam implantation with subsequent annealing and (2) ion beam implantation at elevated temperatures to facilitate *in-situ* annealing.

5.2 Experiments

5.2.1 Ion beam implantation

GaAs nanowires were implanted with Mn ions at room temperature and at temperatures up to 400 °C. Ion fluencies from $1 \cdot 10^{15}/\text{cm}^2$ to $2 \cdot 10^{16}/\text{cm}^2$ were used. The nanowires had diameters ranging from about 30 to 80 nm. The diameter distribution on one growth substrate is only a few nanometers wide, but typically the nanowires are slightly tapered and a few percent thinner close to their tip than at their bottom, due to additional growth at the side facets [Bor04].

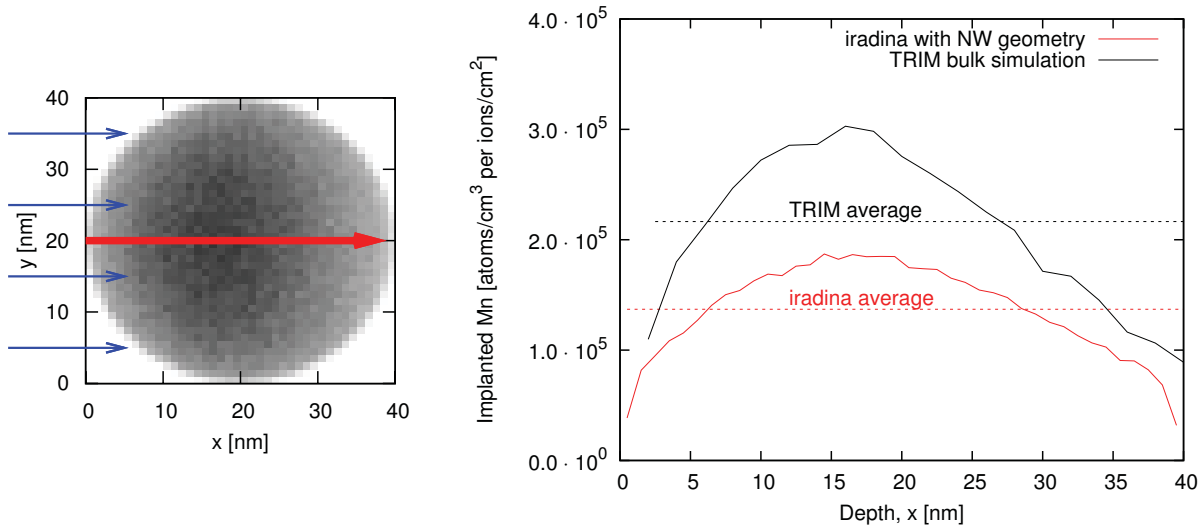


Figure 5.1: Simulation results created by *iradina* for implantation of 40 keV Mn ions into a GaAs nanowire with 40 nm diameter. Left: cross sectional distribution of implanted ions, grey scale shows concentration of Mn ions in arbitrary units. Blue arrows show the direction of incoming ions. Right: Implantation profile corresponding to the red arrow from the left figure. A bulk implantation profile simulated with TRIM is shown for comparison. The average concentrations of implanted ions are indicated as dashed lines.

The nanowires were well aligned on homoepitaxial growth substrates. The substrates were inserted into the implantation chamber and the nanowires were implanted under oblique angles of about 45° . Computer simulations were performed in order to find the optimum ion energies for implantation and to obtain the concentration of implanted Mn atoms within the nanowires. The simulations were done with *iradina* (see chapter 3). It is important to take into account the correct nanowire geometry during the simulation, because bulk simulations turn out to overestimate the concentration of implanted atoms strongly: for implantation of 40 keV Mn ions into GaAs nanowires of 40 nm diameter, bulk simulations done with TRIM overestimate the concentration of implanted ions by a factor of 1.6. This effect is illustrated in figure 5.1, comparing the distribution of implanted ions as simulated with TRIM and *iradina*.

The range straggling is quite large compared to the ion range itself at such low implantation energies; thus, it was decided to implant each nanowire substrate only with one energy for the sake of simplicity instead of using profiles of multiple ion energies, as usually done for homogeneous bulk doping. Implantation energies between 40 keV and 60 keV were selected depending on the mean nanowire diameter.

For the example of Mn ions with 40 keV implanted into NW with 40 nm diameter, shown in figure 5.1, a fluence of $1 \cdot 10^{15}/\text{cm}^2$ results in an average volume concentration of about $1.4 \cdot 10^{20}/\text{cm}^3$, corresponding to a relative Mn concentration in GaAs of about 0.3%. In terms

of $\text{Ga}_{1-x}\text{Mn}_x\text{As}$, this corresponds to $x = 0.006$. Higher Mn concentrations in the range of $x \approx 0.03$ to 0.07 are desirable for ferromagnetic ordering to occur [Ohn98]. Therefore, some nanowire samples were implanted with $1 \cdot 10^{16}/\text{cm}^2$, corresponding to $x \approx 0.06$. One should note though, that at these high fluencies the *iradina* simulations might overestimate the average Mn concentration: the nanowires are thinned during the implantation by sputtering – an effect not captured in a static simulation. At the end of the implantation process, fewer ions will be implanted in the thin nanowire, because more ions are transmitted. The sputter yield of 40 keV Mn ions incident on the GaAs NW of 40 nm diameter is about 20. Thus, as a rough estimation, implanting 3% Mn would result in removal of 60% of the material and consequently a reduction in diameter of about 36%. However, since the sputter yield depends on the nanowire diameter (compare to section 3.3.4), a dynamic simulation code would be required in order to calculate this effect more accurately.

5.2.2 Post-implantation annealing

In order to remove ion beam induced defects, the implanted nanowires were annealed using different parameters. Some samples were annealed in vacuum (about 10^{-2} mbar) at temperatures ranging from 350 °C up to 500 °C, for 30 minutes each. The temperature was not increased further, because decomposition of the nanowires occurred (see below, section 5.3.2). Other substrates with implanted nanowires were annealed under AsH_3 atmosphere to prevent loss of arsenic at temperatures ranging from 350 °C to 650 °C². In preliminary experiments, it had been tried to anneal Mn implanted GaAs nanowires in arsine atmosphere at 800 °C, as was reported successful for Zn implanted GaAs nanowires [Sti08b]; however, the Mn implanted GaAs nanowires were completely decomposed at 800 °C [Skö07].

In order to investigate the morphology and crystal structure of the nanowires, TEM specimens were prepared as described in section 2.3 before and after the annealing of each sample³.

5.2.3 Implantation at elevated temperatures

Nanowires were implanted at elevated temperatures ranging from 100 °C to 400 °C. Higher temperatures were not selected, because decomposition of Mn-implanted nanowires occurred in vacuum at 500 °C (see below, section 5.3.2). The substrates with nanowires were mounted

²The annealing experiments under arsine atmosphere were performed by Magnus Borgström in Lund.

³TEM investigations were partly done in Jena by the author of this thesis and partly in Lund by Maria E. Messing.

into the implantation chamber, the chamber was pumped down and heating of the samples was started when the vacuum was about $1 \cdot 10^{-5}$ mbar. Typical heating rates of 25K/min were used. The ion beam implantation was started a few minutes after reaching the desired temperature in order to allow the sample surface to reach equilibrium temperature with the surrounding holder. The ion current density was always limited to 500 nA/cm², corresponding to a power density of about 20 mW/cm², in order to avoid excessive additional heating of the sample surface by the ion beam.

5.3 Results and discussion

5.3.1 Room temperature implantation

Figure 5.2 illustrates the structural impact of implanting Mn into GaAs nanowires. The as-grown nanowires [figure part (a)] are highly-crystalline with zincblende structure, growing in [111] direction. The Au droplet (growth seed particle) is still attached. The nanowires exhibit planar defects, which are mostly twin planes, all perpendicular to the nanowire axis⁴. The twin planes cause two orientations to occur in the fourier transform [see inset of figure part (a)]. These two orientations just differ by rotation of 180° about the [111] axis⁵.

After ion beam implantation with high fluencies of Mn, the nanowires are amorphized, as shown in figure 5.2(b). The diffraction pattern (DP) recorded from large parts of the nanowires, shows no peaks but only rings corresponding to the amorphous phase. For lower fluencies or larger diameters, the NWs do not become completely amorphized, as illustrated in figure 5.2(c). In this case, half of the nanowire became amorphous, while the crystal structure was preserved in the other half, as shown by the fractional FFTs.

This half amorphized nanowire presents a very interesting case, which allows to estimate an amorphization threshold for Mn implantation of GaAs nanowires: The NW in question has a diameter of 60 nm and was irradiated with 60 keV Mn ions using a fluence of $2.6 \cdot 10^{15}$ ions/cm². An *iradina* simulation was made with these parameters and the displacement events were extracted from the simulation. Note that a single ion causes approximately 10^3 displacements. The displacement events can be compared to the TEM image, as illustrated in figure 5.3. From the point in the nanowire where amorphization stops, an amorphization threshold of approxi-

⁴Different definitions of twin planes can be found in the literature. Here, a twin plane \underline{A} is a mirror plane where the stacking order of (111)-planes is reversed: ... ABC \underline{A} CBA..., see [Car08] for details.

⁵Note, most of the following HR-TEM images were recorded with a zone axis (ZA) of $\overline{[110]}$ or equivalent. For clarity, the indices in the following FFTs are mostly not labeled.

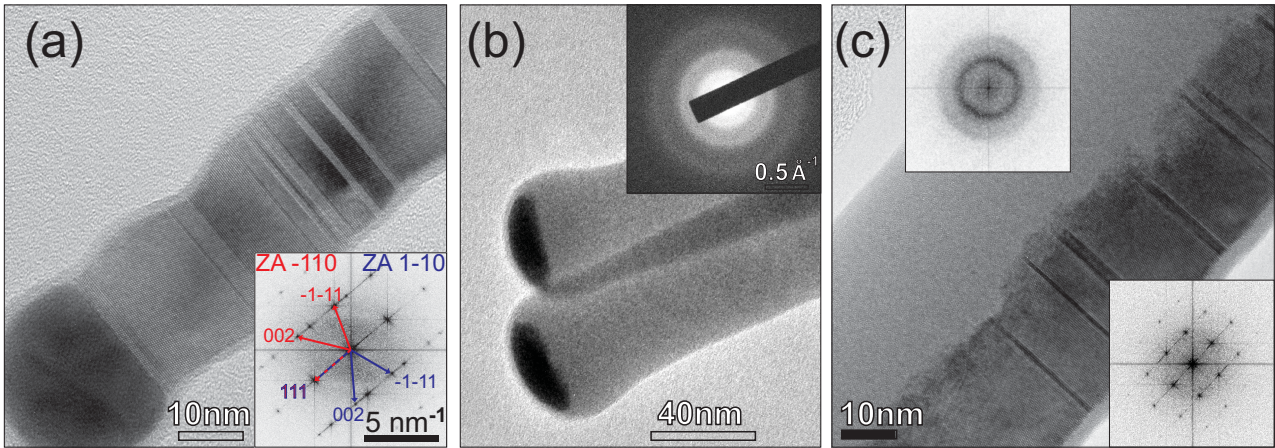


Figure 5.2: (a) HR-TEM image of as-grown (non-implanted) GaAs NW. The Au droplet is visible at the bottom left. Inset shows FFT of wire only, reflexes are labeled; two directions occur due to twin planes. (b) NWs implanted with $9.5 \cdot 10^{15}/\text{cm}^2$, 40 keV, at RT. The inset shows a DP of the completely amorphized nanowires (Au droplets were excluded when recording the DP). (c) Nanowire implanted with $2.6 \cdot 10^{15}/\text{cm}^2$, 60 keV, RT. The NW is partly amorphized. The two insets are FFTs calculated from upper left and lower right region of the image.

mately 7 DPA (displacements per atom) can be estimated for RT implantations, meaning that each target atom has to be displaced 7 times until the material is amorphized. At first, this number appears to be quite high for GaAs. For example during Si implantation into GaAs at room temperature, about 2 DPA were observed to lead to complete amorphization [Bro97]. A part of that discrepancy can be explained by sputtering: The original nanowire was thicker and some material was sputtered away. Thus, the material at the back side of the nanowire suffered less damage in reality than in the simulation, because the static simulation cannot capture this effect. The sputter yield for 60 keV Mn ions incident on GaAs NWs of 60 nm diameter is about 20. At the given fluence, this results roughly in a reduction of the NW radius by about 10 nm throughout the irradiation. Shifting the damage distribution by an average 5 nm to the front, would result in an amorphization threshold of about 5 DPA, which is still higher than in bulk. This indicates that strong dynamic annealing occurs in the nanowire: the ion deposits its energy in a small volume, leading to local heating of the material. High temperatures can be reached and immediate annealing of a fraction of the defects is possible. In bulk material, the thermal energy quickly dissipates (typically on a time scale of about 0.1 ps [Hof98]) leaving little time for annealing. In the nanowire, the thermal energy can only dissipate in one dimension as opposed to three dimensions in bulk. Thus, there is more time for *in-situ* removal of defects. This significant enhancement of dynamic annealing increases the amorphization threshold. A similar effect has been observed for Ga implantation of GaN nanowires: Dhara

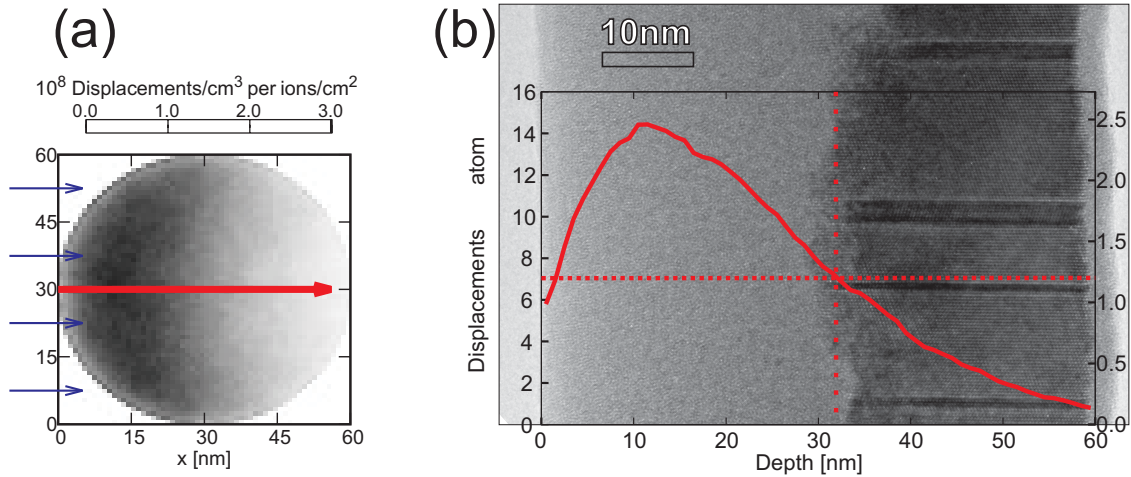


Figure 5.3: (a) Simulation results from iradina for implantation of 60 keV Mn ions into GaAs NW with 60 nm diameter. The number of displacement events (coded in grey scale) is shown over the cross section of the nanowire. Blue arrows indicate ion beam direction. (b) TEM image of implanted NW [the same image as in figure 5.2(c)]. Superimposed is a plot of the displacement events corresponding to the red arrow in (a). Right ordinate shows displacements per implanted ions, left ordinate is multiplied with fluence of $2.6 \cdot 10^{15}/\text{cm}^2$ as implanted in reality and divided by GaAs density, yielding the number of displacements per target atom (DPA). The amorphization threshold is $\approx 7\text{DPA}$ at RT.

et al. reported a five-fold increase in amorphization threshold and attributed this to enhanced dynamic annealing [Dha03].

5.3.2 Subsequent annealing

Figure 5.4 shows TEM micrographs of GaAs nanowires implanted with $9.5 \cdot 10^{15}$ Mn ions / cm^2 at room temperature and subsequently annealed in vacuum. The previously amorphized nanowires are recrystallized during the annealing at 400 °C. However, they do not become single crystals as before, but become polycrystalline, as shown in the inset of figure 5.4(a). The situation is similar at 350 °C (not shown). When annealing the nanowires at 500 °C in vacuum, their structure changes strongly, see figure 5.4(b-d). They also recrystallize (see the DP), but they become very inhomogeneous. EDX measurements show that these NWs consist of typically $\approx 90\%$ Ga and only little As. The loss of As can be attributed to the high As vapor pressure over GaAs at such temperatures, and has also been reported for annealing ion implanted bulk GaAs [Wes92].

In conclusion, 400 °C vacuum annealing after implantation is not sufficient to obtain single crystalline nanowires but higher annealing temperatures lead to the decomposition of the nanowires. Thus, the possibility to remove the ion beam induced damage via vacuum annealing is eliminated.

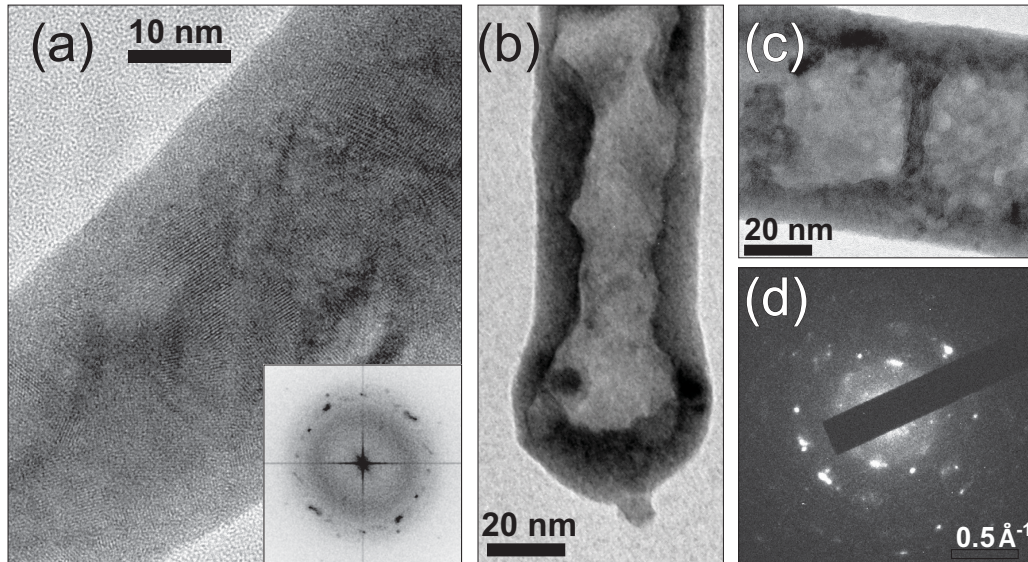


Figure 5.4: TEM micrographs of nanowires implanted with Mn ($9.5 \cdot 10^{15}/\text{cm}^2$) at RT and annealed in vacuum. (a) After annealing at 400 °C. The NW is recrystallized but polycrystalline (see inset FFT). (b,c) After annealing at 500 °C, the nanowires become very inhomogeneous. (d) shows a typical DP of NWs annealed at 500 °C.

For that reason, GaAs nanowires implanted with Mn were annealed in AsH₃ atmosphere to avoid excessive loss of arsenic. Similar methods were reported successful for annealing of Zn implanted GaAs nanowires [Sti08b] and have been used for annealing bulk GaAs for decades [Kas79]. Figure 5.5 illustrates the resulting structure of Mn implanted GaAs nanowires after annealing in arsine. Within the investigated temperature range, all nanowires were recrystallized (350 to 650 °C). In figure 5.5(a), bottom part, one observes the single crystalline structure of the nanowire with the original twin planes perpendicular to the nanowire axis. However, in the top part of figure 5.5(a), twin planes in a new direction appear, not found in the as-grown nanowires. Probably, the nanowire was half amorphized during irradiation, similar to the situation shown in figure 5.2(c). The original crystal structure is maintained in the non-amorphized half, while the amorphous half recrystallized starting from the remaining crystals. However, strong twinning occurs, possibly due to ion beam induced or thermal stress in the nanowire. Figure 5.5(b) illustrates a nanowire which became polycrystalline after the annealing. The radius of the ring in the FFT corresponds to the (111)-plane spacing in GaAs, indicating that the crystals consist of GaAs. This nanowire was probably one that was completely amorphized during ion beam irradiation. The original crystalline orientation was completely lost and recrystallization occurred randomly, leading to the polycrystalline nanowire.

A new phenomenon occurs when annealing at higher temperatures in arsine atmosphere, illustrated in figure 5.5(c,d). In contrast to vacuum annealing, the loss of arsenic is avoided;

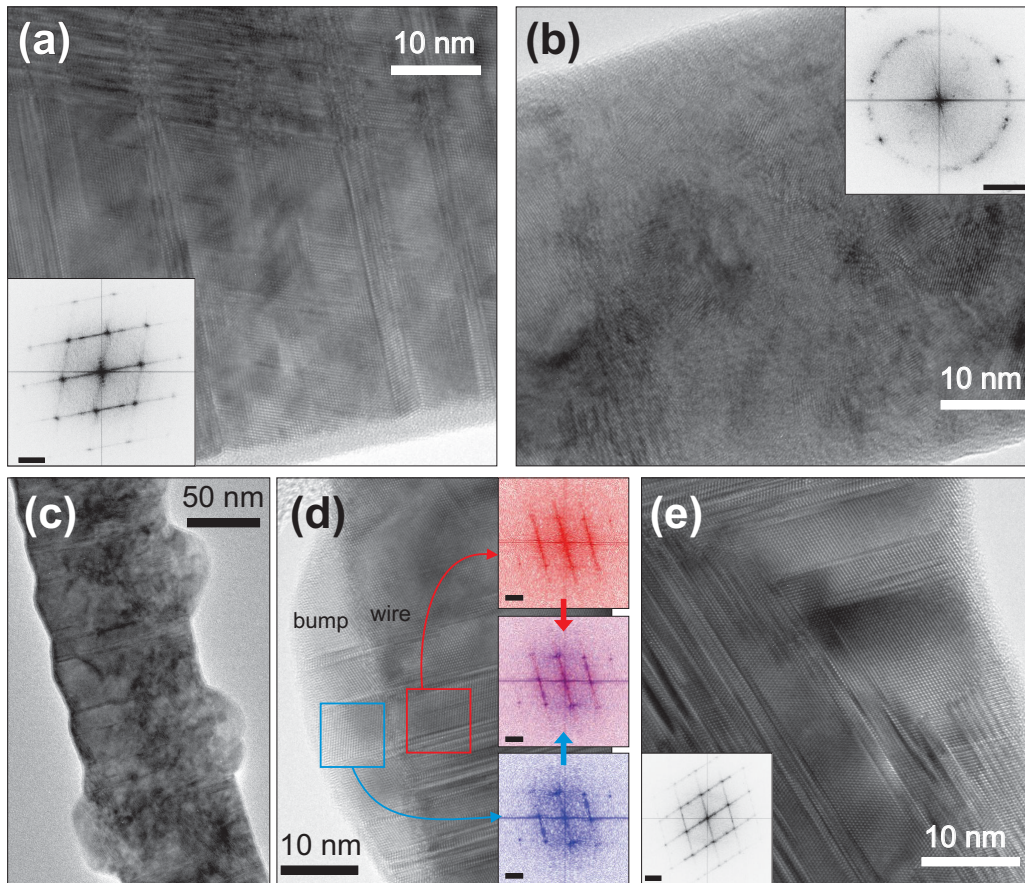


Figure 5.5: TEM images of nanowires implanted at RT and annealed in arsine atmosphere. Insets are FFTs, their scale bars are 2 nm^{-1} . (a) Annealed at $350 \text{ }^\circ\text{C}$, twinning in new direction occurs. (b) Annealed at $350 \text{ }^\circ\text{C}$, polycrystalline nanowire, radius of the ring in the FFT corresponds to the (111)-plane spacing in GaAs. (c) Annealed at $550 \text{ }^\circ\text{C}$, bumps appear on the nanowire sides. (d) Annealed at $650 \text{ }^\circ\text{C}$, structural analysis of a bump: localized FFTs of bump and wire show that they have same crystal structure (the middle FFT is an overlay of the red and the blue one). (e) Annealed at $650 \text{ }^\circ\text{C}$, strong twinning in new direction.

however, “bumps” appear on the nanowire side facets. EDX measurements indicate that these bumps may consist of GaAs, but the significance is low, due to the limited spatial resolution of EDX and the small volume of the bumps compared to the nanowires. Nevertheless, in the HR-TEM images, the bumps show the same crystal structure and the same orientation as the nanowires (see overlay FFT in 5.5(d), even the twin planes from the NW extend into the bump). Thus, the bumps most likely consist of GaAs. The bumps are possibly formed during annealing by As from the arsine atmosphere and excess Ga from the nanowire: the sputter yield for As is about a factor of 1.5 larger than the sputter yield of Ga; thus, one can expect excess Ga after the implantation.

Apart from the bumps, the nanowires annealed at $650 \text{ }^\circ\text{C}$ in AsH_3 exhibit the same structure as the ones annealed at $350 \text{ }^\circ\text{C}$ in AsH_3 : figure 5.5(e) illustrates the strong twinning in new

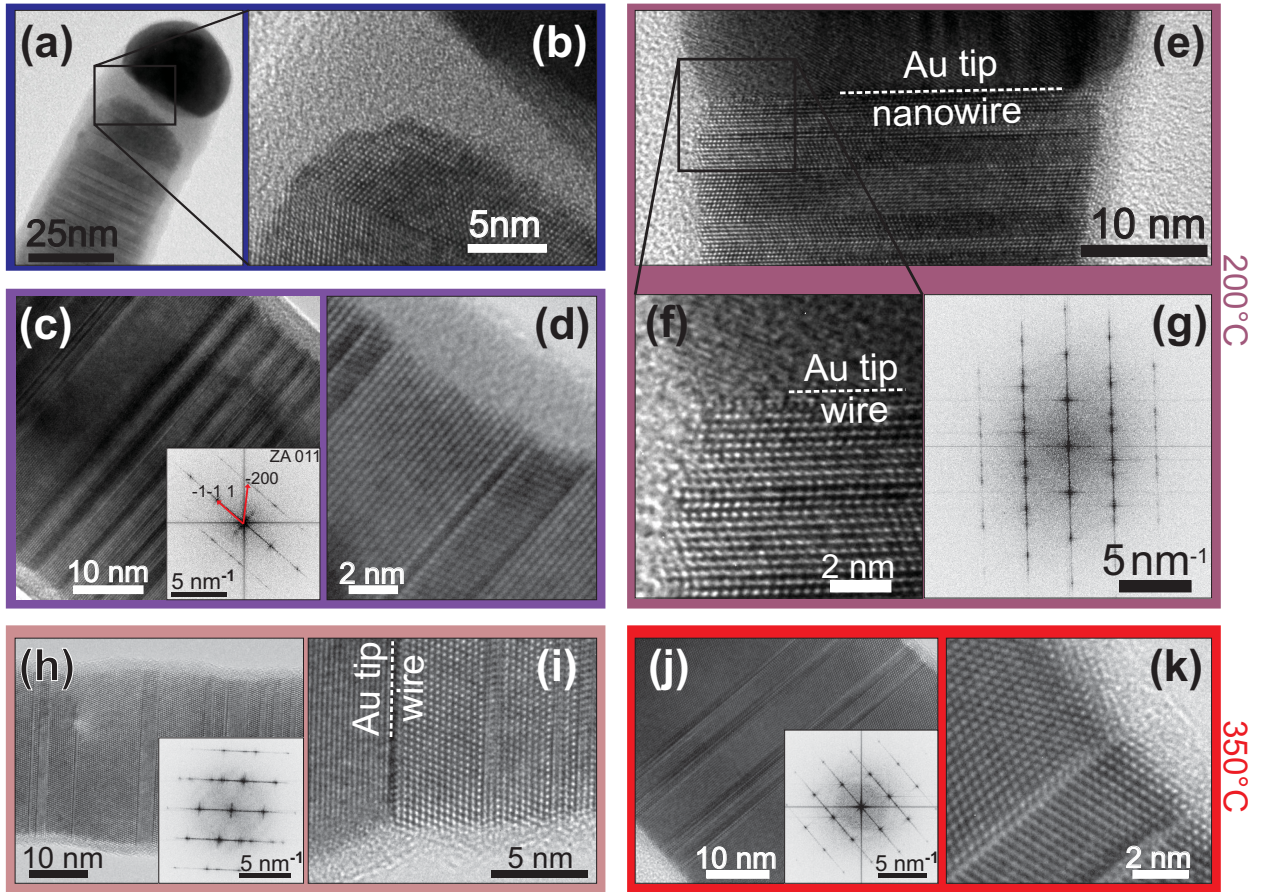


Figure 5.6: (HR-)TEM images of GaAs nanowires implanted with $2 \cdot 10^{15}$ Mn ions/cm² at elevated temperatures, as indicated at the sides; insets are FFTs. (a,b) NW mostly remains single crystalline; amorphous gap between wire and Au tip. (c-k) At higher temperatures, NWs remain single crystalline as well, sharp interfaces between crystalline NWs and Au tip. Twin planes perpendicular to NW axis.

directions, in addition to the original twin structures. A high density of twins decreases the conductivity in semiconductors [Sti90], and is therefore not desired.

In conclusion, neither post-implantation annealing technique can be used to obtain single crystalline low-defect GaAs nanowires after high dose ion beam implantation of Mn.

5.3.3 Implantation at elevated temperatures

Instead of post-implantation annealing, *in-situ* annealing (in addition to the dynamic annealing) is performed by heating the target during ion beam implantation. The idea is that most of the ion beam damage anneals immediately; thus, no amorphization occurs and the crystallinity is never lost. In bulk GaAs, it has been observed that amorphization can be delayed greatly by increasing the substrate temperature above room temperatures [Bro97]. Since the target must be in vacuum for ion beam implantation, 400 °C cannot be exceeded to avoid decomposition of the nanowires, as shown in the previous section.

Figure 5.6 shows TEM images of nanowires implanted with Mn at different temperatures from 100 °C to 350 °C, all with fluencies of $2 \cdot 10^{15}$ ions/cm² (corresponding to an atomic Mn concentration of about 1%). Even at an implantation temperature of 100 °C [figure 5.6(a,b)], the nanowires are mostly crystalline after implantation. There are twin planes, all perpendicular to the NW axis, indicating that the original crystal structure is preserved during implantation. However, the shell of the NW is amorphized during implantation and an amorphous gap exists between the Au tip and the nanowire. Probably, the Au tip allows faster cooling of the NW close to the tip (thermal conductivity of Au is 5-6 times larger than that of GaAs), and thus reducing dynamic annealing in this region.

At 150 °C, the NWs remain crystalline as well, but still an amorphized shell is observed in figure 5.6(d). This is further reduced at 200°C, see figure 5.6(e,f). At these high implantation temperatures, no amorphous gap between tip and nanowire appears, and instead, the interface remains perfectly flat as for the as-grown nanowires. The same observation is made for the higher implantation temperatures 250 °C, 300 °C (not shown) and 350 °C. The original crystal structure with its twin planes is always preserved, as shown in figures 5.6(e)-(k). Unfortunately, for the fluencies of $2 \cdot 10^{15}$ ions/cm², the detection limit of the EDX system does not allow to show that the implanted Mn remains within the nanowire.

Anyway, in order to make GaAs ferromagnetic, higher Mn concentrations are required. Thus, further nanowires were implanted with higher fluencies of $1 \cdot 10^{16}$ Mn ions/cm², corresponding to a Mn concentration of about 2.9% ($x \approx 0.058$). The implantation with lower fluencies showed preservation of crystallinity at all temperatures above about 150 °C, but the higher the temperature, the fewer defects are expected to remain. On the other hand, there is an upper limit, when it comes to high Mn concentrations: according to the growth phase diagram of GaMnAs determined by H. Ohno from MBE growth [Ohn96, Ohn98], phase segregation of MnAs might occur at temperatures above about 300 °C. Thus, an implantation temperature of 250 °C was selected for this high-fluence implantation experiment.

Figure 5.7 shows TEM images of a nanowire implanted with $1 \cdot 10^{16}$ Mn ions/cm² at 250 °C, which is highly crystalline and the original structure with its twin planes is preserved. The electron beam was focused to different points on the nanowire, and EDX spectra were recorded, an exemplary spectrum is illustrated in figure 5.8. The characteristic X-ray lines from Ga, As and from Mn are observed. The signal from Au appears as well, because the spectrum was recorded in the vicinity of the nanowire tip. The Cu signal originates from the mesh holding the nanowire, the oxygen may stem from oxidized copper. Other small signals are

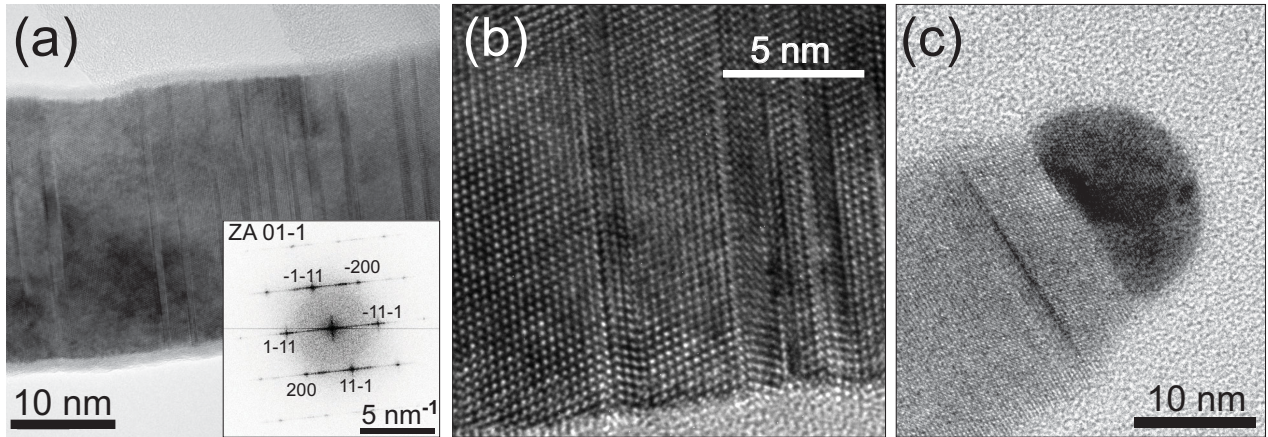


Figure 5.7: GaAs NW implanted with $1 \cdot 10^{16}$ Mn ions/cm² at 250 °C. (a) Single crystallinity with original twin plane structure maintained, inset shows FFT. (b) HR-TEM image of the same nanowire. (c) TEM image of another nanowire, no amorphous gap between wire and tip occurs.

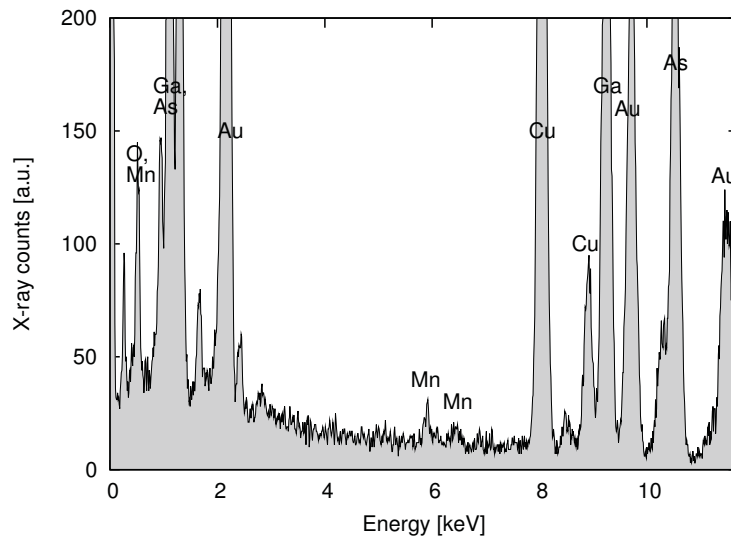


Figure 5.8: X-ray spectrum of a GaAs nanowire implanted with $1 \cdot 10^{16}$ Mn ions/cm² at 250 °C. The spectrum was recorded in a TEM on a point close to the NW tip.

attributed to elements from the sample holder. From these spectra, the Mn concentrations were evaluated to be between 2% and 3% on all measured points, being in good agreement with the concentrations obtained from the *iradina* simulations. This example clearly shows how bulk simulations overestimate concentrations in ion implanted nanostructures and why it is necessary to take into account the correct target geometry, as in *iradina*. However, the EDX spectrum just shows the total Mn concentration, it cannot be concluded what fraction of the Mn atoms actually occupies Ga sites as desired.

5.4 Magnetotransport properties

5.4.1 Sample preparation and measurements

The electrical and magnetotransport properties of nanowires implanted with $1 \cdot 10^{16}$ Mn ions/cm² at 250 °C, as well as unimplanted reference nanowires, were investigated. Single nanowires were contacted and their transport properties measured at different temperatures and with different magnetic fields⁶. First, silicon substrates were prepared for the measurements: the substrates were covered by a 210 nm thick SiO₂ layer for insulation, into which trenches were etched in order to achieve a preferred alignment direction of the NW. The substrates were further covered with markers and macroscopic contact pads. Then some NWs were transferred mechanically onto the substrates, passivated and finally contacted and connected to the macroscopic metal pads using electron beam lithography and evaporation of Pd/Zn/Pd. Four contacts were created on each nanowire to allow 4-point measurements, eliminating the influence of contact resistance. A SEM image of such a contacted nanowire is shown in figure 5.9(a). A Janis VariTemp superconducting cryomagnet system (Model 8T-SVM) was used to perform the magnetotransport measurements. The measurements were carried out at temperatures between 1.6 K and 300 K and at magnetic fields up to 5T parallel and perpendicular to the nanowires.

5.4.2 Results and discussion

2-point and 4-point measurements were compared down to about 70 K. Below, 4-point measurements became difficult, due to the high NW resistance. It can be concluded from the comparison that the contact resistance is mostly negligible compared to the NW resistance.

Figure 5.9(b) shows the current-voltage characteristics of a Mn implanted nanowire for different temperatures. Down to about 100 K, it is mostly ohmic, while a somewhat non-linear but symmetrical behavior dominates at low temperatures. Non-implanted reference samples exhibited resistance in the order of 200 GΩ at room temperature (not shown here); thus, it can be concluded that the ion implantation of Mn strongly increases the conductance.

From the room-temperature resistance in the MΩ regime, a hole concentration of about 10^{17} /cm³ can be estimated, assuming a reduced mobility of 60 cm²/Vs [Slu07] and 40 nm wire diameter. This hole concentration is very low, considering the high doping levels of Mn ($x \approx 0.058$). Several effects may explain this observation. Fermi-level pinning at the GaAs surface (typical

⁶The preparation and measurements were done by Waldomiro Paschoal Jr. and Sandeep Kumar in Lund.

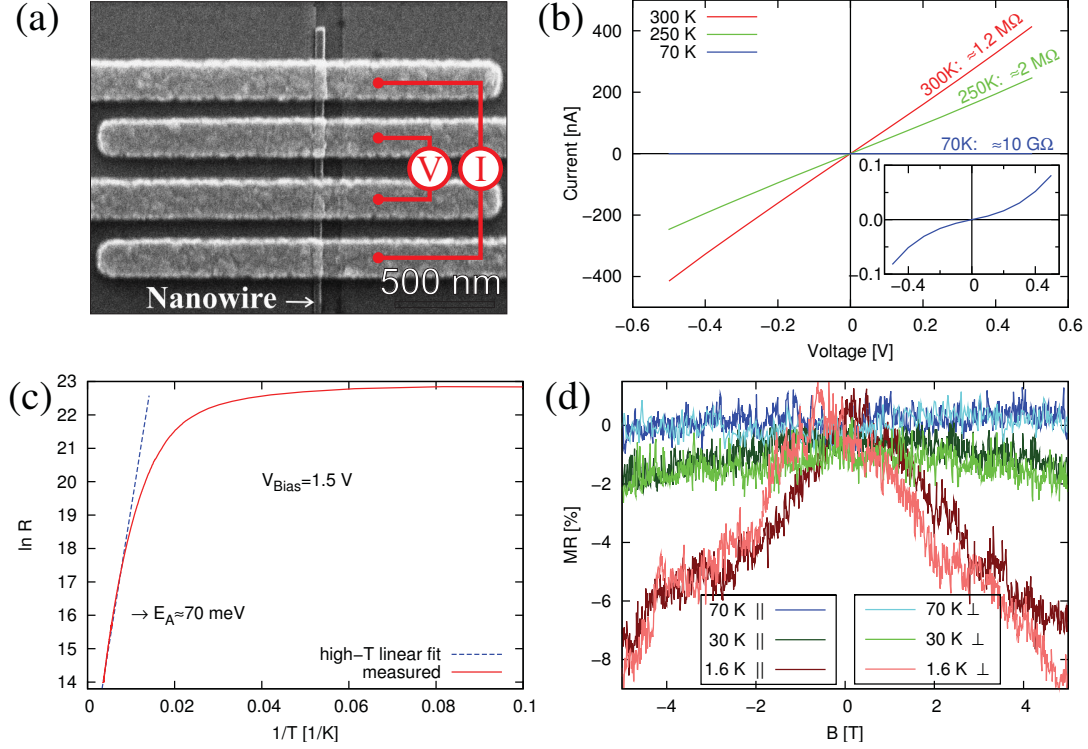


Figure 5.9: (a) SEM image of a contacted nanowire with schematic illustration of 4-point measurement. (b) IV characteristics of a contacted nanowire for different temperatures (inset shows curve for 70K again with different scaling). (c) $\ln(R)$ plotted as a function of $1/T$ to extract activation energy. (d) Relative drop in resistance of the nanowire as a function of magnetic field, which is parallel (||) or perpendicular (\perp) to the NW axis.

in GaAs NWs [Dem10]) effectively creates a radially depleted semiconductor nanowire, leaving only a thin channel of high conductance in the center. Furthermore, the simulated implantation profiles show that the Mn concentration close to the surface is lower than the average (see figure 5.1). Additionally, the Mn acceptors may be compensated to a large extent by donor-type point defects produced during the ion implantation: for example interstitial Mn as well as substitutional As_{Ga} antisites both act as double donors [Sca08].

Figure 5.9(c) shows the resistance as a function of temperature as an Arrhenius plot. An activation energy of about 70 meV is extracted from the linear fit for high temperatures; similar results were obtained for several different nanowires. Slupinski *et al.* found a similar behavior in GaMnAs thin films and attributed it to thermal emission of holes from a Mn impurity band to the valence band [Slu07]. It should be noted that this result is different from the activation energy of isolated substitutional Mn impurities on Ga sites in (low doped) GaAs, which is typically observed around 113 meV [Ile75].

If ferromagnetic ordering of Mn spins occurred in the nanowire, one would expect a singularity in the derivative of the resistance at the critical temperature [Nov08]. Such singularity does

not occur, indicating that ferromagnetic ordering does not occur. The reason for this absence is most probably the hole concentration (see above). It is too low to mediate ferromagnetic coupling between the Mn spins. The uncoupled spins can only lead to a paramagnetic state. More light can be shed on the magnetic properties of the nanowires by the measurements of the resistance as a function of an externally applied magnetic field at different temperatures [see figure 5.9(d)]. No significant magnetoresistance (MR) effect is observed for 70K, but at the lower temperatures of 30K and 1.6 K, the resistance decreases with increasing magnetic field (negative MR). The MR is not observed to saturate within the investigated range up to 5T and no hysteresis effects were found, supporting the finding that the Mn implanted nanowires are in a paramagnetic state and not ferromagnetic. Furthermore, no significant anisotropy was observed for magnetic fields parallel and perpendicular to the nanowire, which one might expect for a ferromagnetic DMS due to different orientation of the magnetization relative to the current direction. Magnetotransport measurements of the non-implanted reference nanowires were practically impossible due to the high resistance of $\approx 200 \text{ G}\Omega$.

There are two mechanisms to which the negative MR is usually attributed: spin-disorder scattering in metallic samples [Ohn99] and suppression of Anderson localization of holes in insulating or semiconducting samples [Iye99]. Both mechanisms possibly contribute to the decrease in resistance at high magnetic fields. The Zeeman energy splitting for a spin of $5/2$ and an external field of 5 T is in the order of 1.4 meV, (corresponding to a temperature of about 16 K). Thus, at higher temperatures like 70 K, the spins are almost randomly oriented. At lower temperature, the Mn spins become successively oriented by the magnetic field and spin-disorder scattering is reduced. At high magnetic fields, the Zeeman shift may also move the Fermi energy for one of the spin-orientations to the non-localized side of the mobility edge, suppressing the localization and enhancing conductivity [Iye99].

From the magnetoresistance properties, one can also obtain some information about possible segregation of small MnAs clusters: theoretical studies by Michel *et al.* on the influence of ferromagnetic MnAs clusters in a paramagnetic GaMnAs thin film reveal that a high density of MnAs clusters leads to a strong positive MR behavior of several hundred percent between 30 and 100 K [Mic08]. Negative MR at high cluster densities is only expected below 30 K. In contrast, the experimental results on Mn-doped GaAs nanowires only show a weak negative MR below 70 K and no positive MR at all, see figure 5.9(d), which indicates that there are either no MnAs clusters in the nanowires or at least a low density of them, meaning that most of the Mn is indeed diluted in the GaAs host matrix as desired.

5.5 Summary and outlook

Diluted magnetic semiconductors (DMS) are prospective materials for future spintronic devices, because they allow electrical control of the magnetism and the spin-polarization. One of the promising candidates is $\text{Ga}_{1-x}\text{Mn}_x\text{As}$, because the GaAs is a well studied semiconductor and has been used in technological applications for decades. When x is in the order of a few percent, $\text{Ga}_{1-x}\text{Mn}_x\text{As}$ can become a ferromagnetic DMS. The Mn atoms provide the unpaired spins as well as holes that couple the spins.

The low solubility limit of transition metals in semiconductors makes it difficult to incorporate sufficient amounts without causing phase segregation; nevertheless ferromagnetic thin film $\text{Ga}_{1-x}\text{Mn}_x\text{As}$ has been achieved via low temperature MBE [Ohn98]. However, the incorporation of sufficient Mn into GaAs *nanowires* remains problematic, due to the complex mechanism employed during nanowire growth. Most reported attempts suffer from phase segregation of MnAs.

Within the scope of this thesis, ion implantation was investigated as a possibility for hyperthermal Mn doping of pre-grown GaAs nanowires beyond the solubility limit. As ion beam implantation induces a large amount of damage in the material, annealing is required to remove the damage. Two approaches were studied: First, post-implantation annealing in vacuum or arsine atmosphere and second, implantation at elevated temperatures in order to facilitate *in-situ* annealing.

In the first approach, the nanowires were to a large extent amorphized during implantation. A high amorphization threshold of 5 to 7 DPA was found, which can be attributed to the enhancement of dynamic annealing in nanowires as compared to bulk. Subsequent annealing in vacuum up to 400 °C leads to recrystallization but either to polycrystalline GaAs or to heavily twinned NWs. At higher temperatures, decomposition was observed. Annealing in arsine atmosphere could not solve the problems: the NWs became heavily twinned or polycrystalline at 350 °C. At higher temperatures, unwanted side growth of GaAs bumps occurred.

The second approach using *in-situ* annealing showed promising results: At implantation temperatures above about 150 °C, the crystal structure of the GaAs nanowires was preserved during implantation. The dynamic annealing, which is already enhanced due to the confined geometry of the nanowire, is further enhanced by the higher base temperature. Highly Mn doped $\text{Ga}_{1-x}\text{Mn}_x\text{As}$ nanowires with $x \approx 5 - 6\%$ with high crystallinity were obtained at an implantation temperature of 250 °C. These nanowires were contacted and their electrical and

magnetotransport properties were investigated. The electrical measurements showed that the implantation decreased the room temperature resistance by about 5 orders of magnitude from about 200 G Ω to 1.2 M Ω . The temperature-dependent resistance reveals an activation energy of 70 meV, which points to a Mn impurity band rather than isolated impurities. Nevertheless, the estimated hole concentration ($\approx 10^{17}/\text{cm}^3$) is far lower than expected from the Mn doping concentration, possibly due to depletion by Fermi-level pinning at the NW surface and due to compensation by donors (interstitial Mn and As_{Ga} antisites). The low carrier concentration inhibits ferromagnetic ordering to occur in the nanowires.

At low temperatures (30K and 1.6K), a negative magnetoresistance (MR) is observed, independent of the direction of the external magnetic field. This could be caused by reduced spin-disorder scattering and suppression of Anderson localization. No traces of ferromagnetism are found in the MR curves. Nevertheless, the MR behavior indicates that the implanted Mn is mainly diluted in the GaAs matrix as desired and does not segregate in MnAs clusters.

Although no ferromagnetic DMS nanowires of Mn-doped GaAs were achieved, the results obtained here pave the way for further attempts, as the possible range for implantation parameters and the structural impact of the implantation are identified. In future experiments, a higher activation level of Mn impurities might be reached by optimizing the implantation conditions; temperatures slightly above 250 °C might be beneficial. Furthermore, mild post-implantation annealing (below the destructive temperatures of 500 °C for vacuum and 650 °C for arsine) could reduce the number of donor-type defects, though the likely segregation of MnAs has to be taken into account above 300 °C.

At the moment it is unknown how the implanted Mn ions are incorporated exactly in the GaAs matrix of the nanowire and what fraction of Mn is actually placed on the Ga sites. More information on this can be extracted from photoluminescence (PL) spectroscopy, which should reveal the various impurity types by their energy levels within the band gap. Much lower doping levels are required for PL, because the crystal should have as little damage as possible and because impurities are more easily identified when isolated. At the moment, low dose ion implantations of Mn in GaAs/AlGaAs core/shell nanowires are under way. The AlGaAs shell is necessary to passivate the GaAs surface, which otherwise quenches most of the PL [Dem10]. More detailed knowledge on the Mn incorporation will allow to improve the activation of Mn acceptors and to increase the hole concentration, which will be a further step on the path to ferromagnetic DMS GaAs nanowires.

Chapter 6

Summary and Conclusion

Since it is difficult to dope self-assembled nanowires during growth owing to the complex growth mechanisms, hyperthermal post-growth doping is required to adjust the properties of semiconductor nanowires. This doping can be achieved by ion beam implantation. Ion beam implantation has been a standard tool for doping of flat or bulk semiconductor materials for decades, but ion beam doping of nanostructured materials has only been studied more recently. New effects occur and new problems arise when implanting ions into nanostructured materials as compared to their bulk counterparts.

This thesis reports on how the ions interact with nanostructures as compared to bulk, how the ion beam influences the structure and morphology of the nanowires, how ion beam induced damage in nanowires can be minimized or annealed and additionally how the ion beam implantation into nanostructures can be simulated accurately. The thesis is divided into three parts, addressing the issues raised above.

For the simulation of ion beam implantation into nanostructures, the new Monte Carlo (MC) code *iradina*, based on the binary collision approximation (BCA), was developed. It works in principle similar to other MC codes like TRIM [Zie85], but in contrast, it allows a flexible definition of three-dimensional target geometries and can thus accurately represent nanostructured targets. Furthermore, several fast routines from the open source computer code *corteo* [Sch08] are adapted, accounting for considerable savings in computation time. The basic correct functionality of the code is demonstrated by comparisons of implantation profiles calculated with *iradina* and TRIM. The profiles of implanted ions as well as ion beam induced damage are mostly in good agreement for light as well as heavy ions in the investigated energy range from 10 to 1000 keV.

The calculation of sputter yields is an interesting application of *iradina*, because sputter yields

of nanostructures can differ strongly from bulk values. The influence of the rectangular grid used in *iradina* on the sputter yield was investigated and shown to be a problem for large cell sizes. Therefore, an analytical description of simple nanostructures (spheres and cylinders) was implemented in *iradina*. The sputtering of Au nanoparticles was investigated and the size dependence of the sputter yield was compared to reported values from literature. There was reasonable agreement with molecular dynamic simulations, but some differences between *iradina* results and semi-analytical models occurred. In this context, it was illustrated why it is not possible to simply use bulk simulations and “cut them off” at the nanostructure surface.

Comparison of bulk sputter yields showed reasonable agreement between *iradina* and TRI-DYN [Möl88]. Larger differences occurred to results from TRIM, but the reason could not be clarified, because it is not known how exactly the TRIM calculations work. Currently, the target in *iradina* is static and no dynamic variation of composition or relaxation of densities can be simulated.

The impact of ion beam irradiation on the structure and morphology of semiconductor nanowires was investigated in the context of ion beam induced bending and alignment of GaAs and ZnO nanowires. Nanowires are observed to bend toward or away from the ion beam depending on the ion energy. For both materials, it was shown that the nanowires can roughly be aligned along the incident ion beam direction, which points out another application of ion beams besides doping: since homogeneous ion beam irradiation of wafer-scaled targets is possible, this method may be used to manipulate huge numbers of nanowires in parallel. For example, [111]-oriented nanowires grown with an inclined angle on (100)-oriented substrates, could be erected by ion irradiation to obtain perpendicular nanowires.

In order to study the underlying mechanisms at work during the bending process, ensembles of nanowires were irradiated with different energies in steps of increasing fluence and their curvatures were measured in between. It was observed that low energy irradiation, where the ions only penetrate a small fraction of the nanowire, leads to bending away from the beam, and high energy irradiation, where the ions are implanted deep into the nanowire, leads to bending toward the ion beam. To obtain a more detailed understanding, single nanowires were irradiated with focused ion beams and the curvatures were studied with *in-situ* SEM. However, the limited ion energy restricted the *in-situ* studies to the low-energy case.

The distribution of ion beam induced defects could be identified as the key mechanism for the bending of the nanowires. Defect distributions were obtained from *iradina* simulations and the

bending in both directions could be explained by inhomogeneous distributions of vacancies and interstitials. A simplified linear elastic model of a nanowire was introduced in an attempt to calculate the bending dynamics of a nanowire under ion irradiation. The model is fed with defect distributions obtained from *iradina* simulations. It turned out that it is problematic to convert the damage distribution to stress induced in the nanowire, because the formation volumes of single defects are not well known. Values from theoretical calculations reported in the literature were used; but these values are partly uncertain and in some cases strongly depend on the charge state of the defects, which are uncertain. For the case of ZnO, the calculations within the linear elastic model could reproduce each experimentally observed case of bending individually, but it was not possible to find common parameters to consistently explain all bending results. For the GaAs nanowires, the experimental results could be reproduced only by ignoring the nanowire surface layer, which points out the limited applicability of a static simulation code. In conclusion, it must be said that the proposed linear elastic bending model contains too many approximations and uncertainties to reliably predict the exact bending dynamics of nanowires for arbitrary irradiation parameters.

The crystalline structure of bent ZnO nanowires was studied in detail. The nanowires remain crystalline during irradiation and the c-axis remains parallel to the local nanowire axis and thus changes gradually. The gradual change in crystal axis is achieved by dislocations, which are shown to stabilize the bent state of the nanowire, even against annealing up to 800 °C. This observation demonstrates that the ion beam causes permanent plastic deformation of the nanowires, in contrast to mechanical bending experiments where nanowires are bent elastically by external forces and permanent bending is difficult to achieve because huge elasticities have to be overcome first.

It was shown that the bending of ZnO nanowires is significantly reduced when heating the samples to 800 °C *during* irradiation. The reason is probably the increased defect mobility at higher temperatures, which can balance the inhomogeneous distribution of defects. This is an important result for doping of nanowires when bending is not desired.

Ion beam implantation of Mn into GaAs nanowires was investigated as a possible means to create highly Mn doped GaAs nanowires for possible spintronic applications. Highly Mn doped GaAs can be a diluted magnetic semiconductor, where the Mn provides the unpaired spins as well as the charge carriers to couple the spins. Thin films of highly Mn doped GaAs have been reported to exhibit ferromagnetism [Ohn96]. But when trying to create highly Mn doped

GaAs nanowires, it turns out that sufficient doping cannot be achieved during growth, because Mn has a low solubility in GaAs and segregation of MnAs occurs at the temperatures required for nanowire growth. Therefore, the Mn must be incorporated after growth of the NWs, for example by ion implantation.

In a first approach, GaAs nanowires were implanted at room temperature and subsequently annealed. During implantation, the nanowires were completely amorphized and the annealing up to 400 °C always lead to polycrystalline nanowires of poor quality. Annealing at higher temperature was not successful, because the nanowires either decomposed (in vacuum) or unwanted additional regrowth of GaAs occurred (in AsH₃ atmosphere). Thus, in a second approach, the nanowires were heated *during* irradiation to temperatures ranging from 100 °C to 400 °C. Above about 150 °C, the higher base temperature further enhances the dynamic annealing to such extent that most defects are annealed immediately and the nanowires always remain crystalline. This way it is possible to achieve highly Mn doped, highly crystalline GaAs nanowires. A suitable implantation temperature was determined to about 250 °C, considering the risk of phase segregation above. Energy dispersive X-ray spectroscopy showed that the Mn is indeed incorporated into the NWs and does not diffuse out. Furthermore, the measured Mn content is in good agreement with simulation results from *iradina*, while TRIM results overestimate the concentration, which demonstrates the importance of taking into account the correct target geometry during simulation.

The implanted nanowires were characterized electrically and the influence of a magnetic field on the electrical properties was investigated. The conductivity was greatly enhanced by Mn doping, as Mn is an acceptor when placed on the Ga site. However, the carrier concentration was probably too low to mediate ferromagnetism and the nanowires were paramagnetic. Probably, the acceptors were to some extent compensated by donors (Mn interstitials and As_{Ga} antisites) and Fermi level pinning at the surface may have caused depletion. Even though ferromagnetic GaAs DMS nanowires have not been achieved yet, the results from ion implantation at elevated temperatures are an important step toward creating nanowire-based spintronic devices. The method may also work for other material systems beside Mn doped GaAs. A better understanding about the exact Mn incorporation should be the focus of future experiments, for instance by PL spectroscopy, in order to find ways to increase the acceptor activation.

With the increasing use and applications of nanostructured materials, the necessity to be able to control and manipulate the nanostructures increases. Ion beam implantation / irradiation

is shown as one important method to address this requirement. Apart from doping of semiconductor nanowires, this thesis also illustrates the possibility of using ion beams to control the morphology of nanowires. The reaction of nanostructures to ion irradiation can be quite different from bulk materials, and these differences must be well understood, in order to make use of ion beams for control and manipulation of nanostructures. The results of this thesis demonstrate some of these differences ranging from doping concentrations, defect production and sputtering to different thermal stability and annealing conditions.

The bending experiments as well as the Mn doping showed that it can be very useful to perform ion beam doping of nanowires at elevated temperatures, because the lower thermal stability of the nanowires make “repairing” of structural and morphological changes by post-implantation annealing difficult. Regarding simulations, all the examples presented in this thesis exhibit the necessity to accurately represent the target structure during the simulations in order to obtain reliable results concerning doping profiles, damage profiles and sputter yields. This necessity emphasizes the importance of the newly developed simulation code *iradina*. For the future, it would certainly be interesting to extend *iradina* to allow dynamic changes of target structure during simulations, in order to obtain a better understanding of the dynamic processes the nanostructures undergo during irradiation. Morphological modifications like bending could be calculated more accurately, and changes in doping profiles caused by thinning of nanostructures due to sputtering could be taken into account. Furthermore, dynamic composition variations would open the door to study additional effects like ion beam mixing in nanostructures, which can be important for example when doping nanowires embedded in other materials or nanowires with a core-shell structure.

Bibliography

- [Aga05] R. Agarwal, C. J. Barrelet, and C. M. Lieber. Lasing in single cadmium sulfide nanowire optical cavities. *Nano Letters* **5**, 917 (2005).
- [Aga06] R. Agarwal and C. Lieber. Semiconductor nanowires: optics and optoelectronics. *Applied Physics A* **85**, 209 (2006).
- [Agr08] R. Agrawal, B. Peng, E. E. Gdoutos, and H. D. Espinosa. Elasticity Size Effects in ZnO Nanowires - A Combined Experimental-Computational Approach. *Nano Letters* **8**, 3668 (2008).
- [Bai88] M. N. Baibich, J. M. Broto, A. Fert, F. N. V. Dau, F. Petroff, P. Eitenne, G. Creuzet, A. Friederich, and J. Chazelas. Giant Magnetoresistance of (001)Fe/(001)Cr Magnetic Superlattices. *Physical Review Letters* **61**, 2472 (1988).
- [Ber97] B. Ber, V. Kharlamov, Y. Kudrjavitsev, A. Merkulov, Y. Trushin, and E. Zhurkin. Computer simulation of ion sputtering of polyatomic multilayered targets. *Nuclear Instruments and Methods in Physics Research B* **127/128**, 286 (1997).
- [Bet09] M. Bettge, S. MacLaren, S. Burdin, J.-G. Wen, D. Abraham, I. Petrov, and E. Sammann. Low-temperature vapour-liquid-solid (VLS) growth of vertically aligned silicon oxide nanowires using concurrent ion bombardment. *Nanotechnology* **20**, 115607 (2009).
- [Bie80] J. P. Biersack and L. G. Hagmark. A monte carlo computer program for the transport of energetic ions in amorphous targets. *Nuclear Instruments and Methods* **174**, 257 (1980).
- [Bin89] G. Binasch, P. Grünberg, F. Saurenbach, and W. Zinn. Enhanced magnetoresistance in layered magnetic structures with antiferromagnetic interlayer exchange. *Physical Review B* **39**, 4828 (1989).
- [Boe96] J. D. Boeck, R. Oesterholt, H. Bender, A. V. Esch, C. Bruynseraede, C. V. Hoof, and G. Borghs. Controlled formation of nanoscale MnAs magnetic clusters in GaAs. *Journal of Magnetism and Magnetic Materials* **156**, 148 (1996). Proceedings of the Second International Symposium on Metallic Multilayers.
- [Bor04] M. Borgström, K. Deppert, L. Samuelson, and W. Seifert. Size- and shape-controlled GaAs nano-whiskers grown by MOVPE: a growth study. *Journal of Crystal Growth* **260**, 18 (2004).
- [Bor06] C. Borchers, S. Müller, D. Stichtenoth, D. Schwen, and C. Ronning. Catalyst-Nanostructure Interaction in the Growth of 1-D ZnO Nanostructures. *Journal of Physical Chemistry B* **110**, 1656 (2006).
- [Bor09] C. Borschel, R. Niepelt, S. Geburt, C. Gutsche, I. Regolin, W. Prost, F.-J. Tegude, D. Stichtenoth, D. Schwen, and C. Ronning. Alignment of Semiconductor Nanowires Using Ion Beams. *Small* **5**, 2576 (2009).
- [Bor11a] C. Borschel, M. E. Messing, M. T. Borgström, W. Paschoal, J. Wallentin, S. Kumar, K. Mergenthaler, K. Deppert, C. M. Canali, H. Pettersson, L. Samuelson, and C. Ronning. A New

- Route toward Semiconductor Nanospintronics: Highly Mn-doped GaAs Nanowires Realized by Ion-Implantation under Dynamic Annealing Conditions. *Nano Letters* **11**, 3935 (2011).
- [Bor11b] C. Borschel and C. Ronning. Ion Beam Irradiation of Nanostructures - A New 3D Monte Carlo Simulation Code. *Nuclear Instruments and Methods in Physics Research B* **269**, 2133 (2011).
- [Bor11c] C. Borschel, S. Spindler, D. Lerose, A. Bochmann, S. H. Christiansen, S. Nietzsche, M. Oertel, and C. Ronning. Permanent bending and alignment of ZnO nanowires. *Nanotechnology* **22**, 185307 (2011).
- [Box01] W. Boxleitner and G. Hobler. FIBSIM - dynamic Monte Carlo simulation of compositional and topography changes caused by focused ion beam milling. *Nuclear Instruments and Methods in Physics Research B* **180**, 125 (2001).
- [Bro97] R. A. Brown and J. S. Williams. Critical temperature and ion flux dependence of amorphization in GaAs. *Journal of Applied Physics* **81**, 7681 (1997).
- [Bur99] A. Burenkov, K. Tietzel, A. Hossinger, J. Lorenz, H. Ryssel, and S. Selberherr. A computationally efficient method for three-dimensional simulation of ion implantation. In *Intern. Conf. on Simulation of Semiconductor Processes and Devices, 1999, 6-8 Sept.*, pp. 55–58, doi:10.1109/SISPAD.1999.799258. IEEE (1999). ISBN 4-930813-98-0.
- [Bür09] D. Bürger, S. Zhou, J. Grenzer, H. Reuther, W. Anwand, V. Gottschalch, M. Helm, and H. Schmidt. The influence of annealing on manganese implanted GaAs films. *Nuclear Instruments and Methods in Physics Research B* **267**, 1626 (2009). Proceedings of the 16th International Conference on Ion Beam Modification of Materials.
- [Cao08] B. Q. Cao, M. Lorenz, M. Brandt, H. von Wenckstern, J. Lenzner, G. Biehne, and M. Grundmann. p-type conducting ZnO:P microwires prepared by direct carbothermal growth. *physica status solidi (RRL) - Rapid Research Letters* **2**, 37 (2008).
- [Car08] P. Caroff, K. A. Dick, J. Johansson, M. E. Messing, K. Deppert, and L. Samuelson. Controlled polytypic and twin-plane superlattices in III-V nanowires. *Nature Nanotechnology* **4**, 50 (2008).
- [Che06] C. Q. Chen, Y. Shi, Y. S. Zhang, J. Zhu, and Y. J. Yan. Size Dependence of Young's Modulus in ZnO Nanowires. *Physical Review Letters* **96**, 075505 (2006).
- [Che07a] C. Q. Chen and J. Zhu. Bending strength and flexibility of ZnO nanowires. *Applied Physics Letters* **90**, 043105 (2007).
- [Che07b] L. Chen, T. Niebling, W. Heimbrodtt, D. Stichtenoth, C. Ronning, and P. J. Klar. Dimensional dependence of the dynamics of the Mn $3d^5$ luminescence in (Zn, Mn)S nanowires and nanobelts. *Physical Review B* (2007).
- [Che09] C. Chen, H. Niu, H. Hsieh, C. Cheng, D. Yan, C. Chi, J. Kai, and S. Wu. Fabrication of ferromagnetic (Ga,Mn)As by ion irradiation. *Journal of Magnetism and Magnetic Materials* **321**, 1130 (2009).
- [Che11] R. Chen, Q.-L. Ye, T. C. He, T. Wu, and H. D. Sun. Uniaxial tensile strain and exciton-phonon coupling in bent ZnO nanowires. *Applied Physics Letters* **98**, 241916 (2011).
- [Col08] A. Colli, A. Fasoli, C. Ronning, S. Pisana, S. Piscanec, and A. C. Ferrari. Ion beam doping of silicon nanowires. *Nano Letters* **8**, 2188 (2008).
- [CT10] D. Cohen-Tanugi, A. Akey, and N. Yao. Ultralow Superharmonic Resonance for Functional Nanowires. *Nano Letters* **10**, 852 (2010).

- [Cui03a] Y. Cui, X. Duan, Y. Huang, and C. M. Lieber. Nanowires as Building Blocks for Nanoscale Science and Technology. In Z. L. Wang, editor, *Nanowires and Nanobelts, Vol 1: Metal and Semiconductor Nanowires*, chapter 1. Kluwer Academic Publishers, Norwell, MA (2003).
- [Cui03b] Y. Cui, Z. Zhong, D. Wang, W. U. Wang, and C. M. Lieber. High Performance Silicon Nanowire Field Effect Transistors. *Nano Letters* **3**, 149 (2003).
- [Dat90] S. Datta and B. Das. Electronic analog of the electro-optic modulator. *Applied Physics Letters* **56**, 665 (1990).
- [Dem10] O. Demichel, M. Heiss, J. Bleuse, H. Mariette, and A. F. i Morral. Impact of surfaces on the optical properties of GaAs nanowires. *Applied Physics Letters* **97**, 201907 (2010).
- [DeS82] D. DeSimone, C. E. C. Wood, and C. A. Evans. Manganese incorporation behavior in molecular beam epitaxial gallium arsenide. *Journal of Applied Physics* **53**, 4938 (1982).
- [Dha03] S. Dhara, A. Datta, C. T. Wu, Z. H. Lan, K. H. Chen, Y. L. Wang, L. C. Chen, C. W. Hsu, H. M. Lin, and C. C. Chen. Enhanced dynamic annealing in Ga⁺ ion-implanted GaN nanowires. *Applied Physics Letters* **82**, 451 (2003).
- [Dha07] S. Dhara. Formation, Dynamics, and Characterization of Nanostructures by Ion Beam Irradiation. *Critical Reviews in Solid State and Materials Sciences* **32**, 1 (2007).
- [Die11] C. P. Dietrich, M. Lange, F. J. Klüpfel, H. von Wenckstern, R. Schmidt-Grund, and M. Grundmann. Strain distribution in bent ZnO microwires. *Applied Physics Letters* **98**, 031105 (2011).
- [DK11] P. Das Kanungo, R. Koenigler, N. Zakharov, P. Werner, R. Scholz, and W. Skorupa. Characterization of Structural Changes Associated with Doping Silicon Nanowires by Ion Implantation. *Crystal Growth and Design* **11**, 2690 (2011).
- [Dlu09] P. Dluzewski, J. Sadowski, S. Kret, J. Dabrowski, and K. Sobczak. TEM determination of directions of (Ga,Mn)As nanowires grown by MBE on GaAs(001) substrates. *Journal of Microscopy* **236**, 115 (2009).
- [Eck91] W. Eckstein. *Computer Simulation of Ion-Solid Interactions*. Springer Series in Materials Science. Springer, Berlin, Heidelberg, New York (1991). ISBN 3-540-19057-0.
- [Ell08] R. Elliman, A. Wilkinson, T. Kim, P. Sekhar, and S. Bhansali. Ion beam synthesis and doping of photonic nanostructures. *Nuclear Instruments and Methods in Physics Research B* **266**, 1362 (2008).
- [Erh05] P. Erhart, A. Klein, and K. Albe. First-principles study of the structure and stability of oxygen defects in zinc oxide. *Physical Review B* **72**, 085213 (2005).
- [Erh06] P. Erhart, K. Albe, and A. Klein. First-principles study of intrinsic point defects in ZnO: Role of band structure, volume relaxation, and finite-size effects. *Physical Review B* **73**, 205203 (2006).
- [Esc97] A. V. Esch, J. D. Boeck, L. V. Bockstal, R. Bogaerts, F. Herlach, and G. Borghs. Magnetotransport and magnetization properties of p-type Ga_{1-x}Mn_xAs, a new III - V diluted magnetic semiconductor. *Journal of Physics: Condensed Matter* **9**, L361 (1997).
- [Fey64] R. P. Feynman, R. B. Leighton, and M. Sands. *The Feynman Lectures on Physics*. Addison-Wesley, Reading, Massachusetts (1964). ISBN 0-201-02117-X.
- [Flo11] F. Flory, L. Escoubas, and G. Berginc. Optical properties of nanostructured materials: a review. *Journal of Nanophotonics* **5**, 052502 (2011).

- [Ful08] B. Fultz and J. M. Howe. *Transmission Electron Microscopy and Diffractometry of Materials*. Springer, Berlin, Heidelberg (2008).
- [Fur88] J. K. Furdyna. Diluted magnetic semiconductors. *Journal of Applied Physics* **64**, R29 (1988).
- [Gar09] D. J. Gargas, M. E. Toimil-Molares, and P. Yang. Imaging Single ZnO Vertical Nanowire Laser Cavities Using UV-laser Scanning Confocal Microscopy. *Journal of the American Chemical Society* **131**, 2125 (2009).
- [Geb08a] S. Geburt. *Lanthanoid-dotierte ZnO-Nanodrähte*. Diplomarbeit, Universität Göttingen (2008).
- [Geb08b] S. Geburt, D. Stichtenoth, S. Müller, W. Dewald, C. Ronning, J. Wang, Y. Jiao, Y. Y. Rao, S. K. Hark, and Q. Li. Rare Earth Doped Zinc Oxide Nanowires. *Journal of Nanoscience and Nanotechnology* **8**, 244 (2008).
- [Gna10] M. Gnauck. *Elektrische Kontaktierung von ZnO-Nanostrukturen und deren Verwendung für sensorische Zwecke*. Diplomarbeit, Universität Jena (2010).
- [Got95] S. Gottwald, H. Kästner, and H. Rudolph, editors. *Meyers kleine Enzyklopädie Mathematik*. Meyers Lexikonverlag, Mannheim (1995). ISBN 3-411-07771-9.
- [Gui07] G. Guisbiers and S. Pereira. Theoretical investigation of size and shape effects on the melting temperature of ZnO nanostructures. *Nanotechnology* **18**, 435710 (2007).
- [Gut09] C. Gutsche, I. Regolin, K. Blekker, A. Lysov, W. Prost, and F. J. Tegude. Controllable p-type doping of GaAs nanowires during vapor-liquid-solid growth. *Journal of Applied Physics* **105**, 024305 (2009).
- [Hab99] S. Habenicht, W. Bolse, K. P. Lieb, K. Reimann, and U. Geyer. Nanometer ripple formation and self-affine roughening of ion-beam-eroded graphite surfaces. *Physical Review B* **60**, R2200 (1999).
- [Hai07] P. N. Hai, K. Takahashi, M. Yokoyama, S. Ohya, and M. Tanaka. Magnetic properties of MnAs nanoclusters embedded in a GaAs semiconductor matrix. *Journal of Magnetism and Magnetic Materials* **310**, 1932 (2007). Proceedings of the 17th International Conference on Magnetism, The International Conference on Magnetism.
- [Hai09] P. N. Hai, S. Ohya, M. Tanaka, S. E. Barnes, and S. Maekawa. Electromotive force and huge magnetoresistance in magnetic tunnel junctions. *Nature* **458**, 489 (2009).
- [Hau84] M. Hautala. Nuclear stopping in polycrystalline materials: Range distributions and Doppler-shift attenuation analysis. *Physical Review B* **30**, 5010 (1984).
- [Hob89] G. Hobler and S. Selberherr. Monte Carlo simulation of ion implantation into two- and three-dimensional structures. *IEEE Trans. on Computer-Aided Design of Integrated Circuits and Systems* **8**, 450 (1989).
- [Hob95] G. Hobler. Monte carlo simulation of two-dimensional implanted dopant distributions at mask edges. *Nuclear Instruments and Methods in Physics Research B* **96**, 155 (1995).
- [Hob11] G. Hobler and D. Kovac. Dynamic binary collision simulation of focused ion beam milling of deep trenches. *Nuclear Instruments and Methods in Physics Research B* **269**, 1609 (2011).
- [Hoc10] A. I. Hochbaum and P. Yang. Semiconductor Nanowires for Energy Conversion. *Chemical Reviews* **110**, 527 (2010).
- [Hof92] H. Hofsäss, S. Winter, S. G. Jahn, U. Wahl, and E. Recknagel. Emission channeling studies in semiconductors. *Nuclear Instruments and Methods in Physics Research B* **63**, 83 (1992).

- [Hof98] H. Hofsäss, H. Feldermann, R. Merk, M. Sebastian, and C. Ronning. Cylindrical spike model for the formation of diamondlike thin films by ion deposition. *Applied Physics A* **66**, 153 (1998).
- [Hof06] S. Hoffmann, I. Utke, B. Moser, J. Michler, S. H. Christiansen, V. Schmidt, S. Senz, P. Werner, U. Gösele, and C. Ballif. Measurement of the Bending Strength of Vapor-Liquid-Solid Grown Silicon Nanowires. *Nano Letters* **6**, 622 (2006).
- [Hof09] S. Hoffmann, J. Bauer, C. Ronning, T. Stelzner, J. Michler, C. Ballif, V. Sivakov, and S. H. Christiansen. Axial p-n Junctions Realized in Silicon Nanowires by Ion Implantation. *Nano Letters* **9**, 1341 (2009).
- [Hoi11] S. Hoilijoki, E. Holmström, and K. Nordlund. Enhancement of irradiation-induced defect production in Si nanowires. *Journal of Applied Physics* **110**, 043540 (2011).
- [Hua07] B. Hua, J. Motohisa, Y. Ding, S. Hara, and T. Fukui. Characterization of Fabry-Perot microcavity modes in GaAs nanowires fabricated by selective-area metal organic vapor phase epitaxy. *Applied Physics Letters* **91**, 131112 (2007).
- [Ihn07] S.-G. Ihn, J.-I. Song, Y.-H. Kim, J. Y. Lee, and I.-H. Ahn. Growth of GaAs Nanowires on Si Substrates Using a Molecular Beam Epitaxy. *IEEE Transactions on Nanotechnology* **6**, 384 (2007).
- [Ile75] M. Ilegems, R. Dingle, and L. W. R. Jr. Optical and electrical properties of Mn-doped GaAs grown by molecular-beam epitaxy. *Journal of Applied Physics* **46**, 3059 (1975).
- [Ink04] B. J. Inkson, G. Dehm, and T. Wagner. Thermal stability of Ti and Pt nanowires manufactured by Ga⁺ focused ion beam. *Journal of Microscopy* **214**, 252 (2004).
- [Iye99] Y. Iye, A. Oiwa, A. Endo, S. Katsumoto, F. Matsukura, A. Shen, H. Ohno, and H. Munekata. Metal-insulator transition and magnetotransport in III-V compound diluted magnetic semiconductors. *Materials Science and Engineering B* **63**, 88 (1999).
- [Jär08] T. T. Järvi, J. A. Pakarinen, A. Kuronen, and K. Nordlund. Enhanced sputtering from nanoparticles and thin films: Size effects. *Europhysics Letters* **82**, 26002 (2008).
- [Jeo07] H. C. Jeon, T. W. Kang, T. W. Kim, Y.-J. Yu, W. Jhe, and S. A. Song. Magnetic and optical properties of (Ga_{1-x}Mn_x)As diluted magnetic semiconductor quantum wires with above room ferromagnetic transition temperature. *Journal of Applied Physics* **101**, 023508 (2007).
- [Joh03] J. C. Johnson, H. Yan, P. Yang, and R. J. Saykally. Optical Cavity Effects in ZnO Nanowire Lasers and Waveguides. *Journal of Physical Chemistry B* **107**, 8816 (2003).
- [Jun09] K. Jun, J. Joo, and J. M. Jacobson. Focused ion beam-assisted bending of silicon nanowires for complex three dimensional structures. *Journal of Vacuum Science and Technology B* **27**, 3043 (2009).
- [Kan10] P. D. Kanungo, R. Kögler, P. Werner, U. Gösele, and W. Skorupa. A Novel Method to Fabricate Silicon Nanowire p-n Junctions by a Combination of Ion Implantation and in-situ Doping. *Nanoscale Research Letters* **5**, 243 (2010).
- [Kas79] J. Kasahara, M. Arai, and N. Watanabe. Capless anneal of ion-implanted GaAs in controlled arsenic vapor. *Journal of Applied Physics* **50**, 541 (1979).
- [Kim01] F. Kim, S. Kwan, J. Akana, and P. Yang. Langmuir-Blodgett Nanorod Assembly. *Journal of the American Chemical Society* **123**, 4360 (2001).

- [Kim07] H.-B. Kim, G. Hobler, A. Steiger, A. Lugstein, and E. Bertagnolli. Full three-dimensional simulation of focused ion beam micro/nanofabrication. *Nanotechnology* **18**, 245303 (2007).
- [Kim09] H. S. Kim, Y. J. Cho, K. J. Kong, C. H. Kim, G. B. Chung, J. Park, J.-Y. Kim, J. Yoon, M.-H. Jung, Y. Jo, B. Kim, and J.-P. Ahn. Room-Temperature Ferromagnetic Ga_{1-x}Mn_xAs ($x \leq 0.05$) Nanowires: Dependence of Electronic Structures and Magnetic Properties on Mn Content. *Chemistry of Materials* **21**, 1137 (2009).
- [Kli09] A. Klimmer, P. Ziemann, J. Biskupek, U. Kaiser, and M. Flesch. Size-dependent effect of ion bombardment on Au nanoparticles on top of various substrates: Thermodynamically dominated capillary forces versus sputtering. *Physical Review B* **79**, 155427 (2009).
- [Koh00] A. F. Kohan, G. Ceder, D. Morgan, and C. G. Van de Walle. First-principles study of native point defects in ZnO. *Physical Review B* **61**, 15019 (2000).
- [Koz09] M. Kozlik. *Synthese von Halbleiternanodrähten für die Photonik*. Diplomarbeit, Universität Jena (2009).
- [Kra10] A. V. Krasheninnikov and K. Nordlund. Ion and electron irradiation-induced effects in nanostructured materials. *Journal of Applied Physics* **107**, 071301 (2010).
- [Kuc03] S. O. Kucheyev, J. S. Williams, C. Jagadish, J. Zou, C. Evans, A. J. Nelson, and A. V. Hamza. Ion-beam-produced structural defects in ZnO. *Physical Review B* **67**, 094115 (2003).
- [Kun10] D. Kunder, E. Baer, M. Sekowski, P. Pichler, and M. Rommel. Simulation of focused ion beam etching by coupling a topography simulator and a Monte-Carlo sputtering yield simulator. *Microelectronic Engineering* **87**, 1597 (2010).
- [L'E88] P. L'Ecuyer. Efficient and portable combined random number generators. *Communications of the ACM* **31**, 742 (1988).
- [Lee95] H.-Y. Lee and H.-B. Chung. Three-dimensional Monte Carlo calculation of Ga⁺ ion penetration in an a-Se₇₅Ge₂₅ thin film. *Journal of Applied Physics* **78**, 5975 (1995).
- [Li01] D. Li, G. Wang, Y. Chen, L. Lin, G. Shrivastav, S. Oak, A. Tasch, S. Banerjee, and B. Obradovic. A computationally efficient simulator for three-dimensional Monte Carlo simulation of ion implantation into complex structures. *Nuclear Instruments and Methods in Physics Research B* **184**, 500 (2001).
- [Li07] H.-Y. Li, O. Wunnicke, M. T. Borgström, W. G. G. Immink, M. H. M. van Weert, M. A. Verheijen, and E. P. A. M. Bakkers. Remote p-Doping of InAs Nanowires. *Nano Letters* **7**, 1144 (2007).
- [Loo99] D. C. Look, J. W. Hemsky, and J. R. Sizelove. Residual Native Shallow Donor in ZnO. *Physical Review Letters* **82**, 2552 (1999).
- [Mal07] M.-A. Malouin, F. El-Mellouhi, and N. Mousseau. Gallium self-interstitial relaxation in GaAs: An *ab initio* characterization. *Physical Review B* **76**, 045211 (2007).
- [Man06] B. Mandl, J. Stangl, T. Mårtensson, A. Mikkelsen, J. Eriksson, L. S. Karlsson, G. Bauer, L. Samuelson, and W. Seifert. Au-Free Epitaxial Growth of InAs Nanowires. *Nano Letters* **6**, 1817 (2006).
- [Mar06] F. Martelli, S. Rubini, M. Piccin, G. Bais, F. Jabeen, S. De Franceschi, V. Grillo, E. Carlino, F. D'Acapito, F. Boscherini, S. Cabrini, M. Lazzarino, L. Businaro, F. Romanato, and A. Franciosi. Manganese-Induced Growth of GaAs Nanowires. *Nano Letters* **6**, 2130 (2006).

- [Mau86] A. Mauger and C. Godart. The magnetic, optical, and transport properties of representatives of a class of magnetic semiconductors: The europium chalcogenides. *Physics Reports* **141**, 51 (1986).
- [Mic08] C. Michel, M. T. Elm, B. Goldlücke, S. D. Baranovskii, P. Thomas, W. Heimbrodt, and P. J. Klar. Tailoring the magnetoresistance of MnAs/GaAs:Mn granular hybrid nanostructures. *Applied Physics Letters* **92**, 223119 (2008).
- [Mik04] A. Mikkelsen, N. Sköld, L. Ouattara, M. Borgström, J. N. Andersen, L. Samuelson, W. Seifert, and E. Lundgren. Direct imaging of the atomic structure inside a nanowire by scanning tunnelling microscopy. *Nature Materials* **3**, 519 (2004).
- [Mil10] S. Milz. *Konzepte zur Realisierung von einfachen Nanodrahtbauelementen für die Energiegewinnung*. Diplomarbeit, Universität Jena (2010).
- [Miy04] K. Miyamoto, M. Sano, H. Kato, and T. Yao. High-electron-mobility ZnO epilayers grown by plasma-assisted molecular beam epitaxy. *Journal of Crystal Growth* **265**, 34 (2004).
- [Möl84] W. Möller and W. Eckstein. TRIDYN - a trim simulation code including dynamic composition changes. *Nuclear Instruments and Methods in Physics Research B* **2**, 814 (1984).
- [Möl88] W. Möller, W. Eckstein, and J. P. Biersack. Tridyn binary collision simulation of atomic collisions - and dynamic composition changes in solids. *Computer Physics Communications* **51**, 335 (1988).
- [Möl10] W. Möller and M. Posselt. TRIDYN_FZR User Manual. Technical Report FZR-317, Helmholtz-Zentrum Dresden-Rossendorf (2010).
- [Möl11] W. Möller. Personal communication (2011).
- [Mor03] M. Moreno, B. Jenichen, V. Kaganer, W. Braun, A. Trampert, L. Däweritz, and K. Ploog. MnAs nanoclusters embedded in GaAs studied by x-ray diffuse and coherent scattering. *Physical Review B* **67**, 235206 (2003).
- [Mül05] S. Müller. *Wachstum von ZnO Nanodrähten und deren Dotierung durch Ionenstrahlen*. Diplomarbeit, Universität Göttingen (2005).
- [Nag75] H. M. Naguib and R. Kelly. Criteria for bombardment-induced structural changes in non-metallic solids. *Radiation Effects* **25**, 1 (1975).
- [Naw10] W. Nawrocki. Electrical and thermal properties of nanowires in quantum regime. *Reviews on Advanced Materials Science* **23**, 107 (2010).
- [Nov08] V. Novák, K. Olejník, J. Wunderlich, M. Cukr, K. Výborný, A. W. Rushforth, K. W. Edmonds, R. P. Campion, B. L. Gallagher, J. Sinova, and T. Jungwirth. Curie Point Singularity in the Temperature Derivative of Resistivity in (Ga,Mn)As. *Physical Review Letters* **101**, 077201 (2008).
- [Obr98] B. J. Obradovic, G. Balamurugan, G. Wang, Y. Chen, and A. F. Tasch. Monte Carlo simulation of ion implantation into topographically complex structures. Electron Devices Meeting, 1998. IEDM '98 Technical Digest., International, pp. 513–516 (1998).
- [Ohn96] H. Ohno, A. Shen, F. Matsukura, A. Oiwa, A. Endo, S. Katsumoto, and Y. Iye. (Ga,Mn)As: A new diluted magnetic semiconductor based on GaAs. *Applied Physics Letters* **69**, 363 (1996).
- [Ohn98] H. Ohno. Making Nonmagnetic Semiconductors Ferromagnetic. *Science* **281**, 951 (1998).

- [Ohn99] H. Ohno. Properties of ferromagnetic III-V semiconductors. *Journal of Magnetism and Magnetic Materials* **200**, 110 (1999).
- [Oul08] R. F. Oulton, V. J. Sorger, D. A. Genov, D. F. P. Pile, and X. Zhang. A hybrid plasmonic waveguide for subwavelength confinement and long-range propagation. *Nature Photonics* **2**, 496 (2008).
- [Par02] Y. D. Park, A. T. Hanbicki, S. C. Erwin, C. S. Hellberg, J. M. Sullivan, J. E. Mattson, T. F. Ambrose, A. Wilson, G. Spanos, and B. T. Jonker. A Group-IV Ferromagnetic Semiconductor: Mn_xGe_{1-x} . *Science* **295**, 651 (2002).
- [Pec10] E. F. Pecora, A. Irrera, and F. Priolo. Ion beam-induced bending of silicon nanowires. *Physica E: Low-dimensional Systems and Nanostructures* **In Press**, doi: 10.1016/j.physe.2010.11.001 (2010).
- [Pec11] E. Pecora, A. Irrera, S. Boninelli, L. Romano, C. Spinella, and F. Priolo. Nanoscale amorphization, bending and recrystallization in silicon nanowires. *Applied Physics A* **102**, 13 (2011).
- [Per09] D. E. Perea, E. R. Hemesath, E. J. Schwalbach, J. L. Lensch-Falk, P. W. Voorhees, and J. L. Lauhon. Direct measurement of dopant distribution in an individual vapour-liquid-solid nanowire. *Nature Nanotechnology* **4**, 315 (2009).
- [Pet09] C. H. Peters, A. R. Guichard, A. C. Hryciw, M. L. Brongersma, and M. D. McGehee. Energy transfer in nanowire solar cells with photon-harvesting shells. *Journal of Applied Physics* **105**, 124509 (2009).
- [Pos86] M. Posselt. A Short Overview on Monte Carlo Simulations of Ion Beam Penetration into Amorphous Solids. *Physica Status Solidi A* **94**, 337 (1986).
- [Rei98] L. Reimer. *Scanning Electron Microscopy*. Springer, Berlin, Heidelberg, New York, Tokyo (1998). ISBN 3-540-63976-4.
- [Ria08] M. Riaz, A. Fulati, Q. X. Zhao, O. Nur, M. Willander, and P. Klason. Buckling and mechanical instability of ZnO nanorods grown on different substrates under uniaxial compression. *Nanotechnology* **19**, 415708 (2008).
- [Rom09] L. Romano, N. G. Rudawski, M. R. Holzworth, K. S. Jones, S. G. Choi, and S. T. Picraux. Nanoscale manipulation of Ge nanowires by ion irradiation. *Journal of Applied Physics* **106**, 114316 (2009).
- [Ron10a] C. Ronning, C. Borschel, S. Geburt, and R. Niepelt. Ion beam doping of semiconductor nanowires. *Materials Science and Engineering R* **R 70**, 30 (2010).
- [Ron10b] C. Ronning, C. Borschel, S. Geburt, R. Niepelt, S. Müller, D. Stichtenoth, J.-P. Richters, A. Dev, T. Voss, L. Chen, W. Heimbrod, C. Gutsche, and W. Prost. Tailoring the properties of semiconductor nanowires using ion beams. *Physica status solidi B* **247**, 2329 (2010).
- [Rud09] A. Rudolph, M. Soda, M. Kiessling, T. Wojtowicz, D. Schuh, W. Wegscheider, J. Zweck, C. Back, and E. Reiger. Ferromagnetic GaAs/GaMnAs Core-Shell Nanowires Grown by Molecular Beam Epitaxy. *Nano Letters* **9**, 3860 (2009).
- [Sad02] J. Sadowski, K. Deppert, V. Kanski, J. Ohlsson, A. Persson, and L. Samuelson. Migration enhanced epitaxial growth of (In,Ga,Mn)As magnetic semiconductor nanowhiskers. Proc. of the 7th International Conference on Nanometer-scale Science and Technology, June 24th–28th. Malmö, Sweden (2002).

- [Sad07] J. Sadowski, P. Dluzewski, S. Kret, E. Janik, E. Lusakowska, J. Kanski, A. Presz, F. Terki, S. Charar, and D. Tang. GaAs:Mn Nanowires Grown by Molecular Beam Epitaxy of (Ga,Mn)As at MnAs Segregation Conditions. *Nano Letters* **7**, 2724 (2007).
- [Sca03] M. A. Scarpulla, O. D. Dubon, K. M. Yu, O. Monteiro, M. R. Pillai, M. J. Aziz, and M. C. Ridgway. Ferromagnetic Ga_{1-x}Mn_xAs produced by ion implantation and pulsed-laser melting. *Applied Physics Letters* **82**, 1251 (2003).
- [Sca08] M. A. Scarpulla, R. Farshchi, P. R. Stone, R. V. Chopdekar, K. M. Yu, Y. Suzuki, and O. D. Dubon. Electrical transport and ferromagnetism in Ga_{1-x}MnAs synthesized by ion implantation and pulsed-laser melting. *Journal of Applied Physics* **103**, 073913 (2008).
- [Sch07] F. Schiettekatte. *Some notes on Corteo*, available from www.lps.umontreal.ca/~schiette/index.php?n=Recherche.Corteo (2007).
- [Sch08] F. Schiettekatte. Fast Monte Carlo for ion beam analysis simulations. *Nuclear Instruments and Methods in Physics Research B* **266**, 1880 (2008).
- [Sch09a] P. A. Schultz and O. A. von Lilienfeld. Simple intrinsic defects in gallium arsenide. *Modelling and Simulation in Materials Science and Engineering* **17**, 084007 (2009).
- [Sch09b] D. Schwen, M. Huang, P. Bellon, and R. S. Averback. Molecular dynamics simulation of intragranular Xe bubble re-resolution in UO₂. *Journal of Nuclear Materials* **392**, 35 (2009).
- [Sch10] F. Schiettekatte. Personal communication (2010).
- [Sci94] Scientific Group Thermodata Europe. SGTE Alloy Database, http://www.sgte.org/fact/phase_diagram.php?file=As-Ga.jpg&dir=SGTE (1994).
- [Seo95] H. Seong and L. J. Lewis. Tight-binding molecular-dynamics study of point defects in GaAs. *Physical Review B* **52**, 5675 (1995).
- [Seo04] S. S. A. Seo, T. W. Noh, Y.-W. Kim, J. D. Lim, Y. D. Park, Y. S. Kim, Z. G. Khim, H. C. Jeon, T. W. Kang, and S. J. Pearton. Nondestructive spectroscopic method to detect MnAs metallic nanocrystals in annealed GaAs:Mn. *Journal of Applied Physics* **95**, 8172 (2004).
- [She10] Y. Shen, J.-I. Hong, S. Xu, S. Lin, H. Fang, S. Zhang, Y. Ding, R. L. Snyder, and Z. L. Wang. A General Approach for Fabricating Arc-Shaped Composite Nanowire Arrays by Pulsed Laser Deposition. *Advanced Functional Materials* **20**, 703 (2010).
- [Skö07] N. Sköld and C. Ronning. Personal communication (2007).
- [Slu07] T. Slupinski, J. Caban, and K. Moskalik. Hole Transport in Impurity Band and Valence Bands Studied in Moderately Doped GaAs:Mn Single Crystal. *Acta Physica Polonica A* **112**, 325 (2007).
- [Smi00] P. A. Smith, C. D. Nordquist, T. N. Jackson, T. S. Mayer, B. R. Martin, J. Mbindyo, and T. E. Mallouk. Electric-field assisted assembly and alignment of metallic nanowires. *Applied Physics Letters* **77**, 1399 (2000).
- [Sno00] E. Snoeks, A. van Blaaderen, T. van Dillen, C. M. van Kats, M. L. Brongersma, and A. Polman. Colloidal Ellipsoids with Continuously Variable Shape. *Advanced Materials* **12**, 1511 (2000).
- [Spi11] S. Spindler. *Morphologieänderungen und Ausrichtung von Halbleiternanodrähten durch Ionenbeschuss*. Diplomarbeit, Universität Jena (2011).

- [Sta01] T. E. M. Staab, R. M. Nieminen, J. Gebauer, R. Krause-Rehberg, M. Luysberg, M. Haugk, and T. Frauenheim. Do Arsenic Interstitials Really Exist in As-Rich GaAs? *Physical Review Letters* **87**, 045504 (2001).
- [Sti90] M. D. Stiles and D. R. Hamann. Electron transmission through silicon stacking faults. *Physical Review B* **41**, 5280 (1990).
- [Sti93] H. Stippel and S. Selberherr. Three dimensional monte carlo simulation of ion implantation with octree based point location. in *Proceedings of VPAD* pp. 122–123 (1993).
- [Sti05] D. Stichtenoth. *Wachstum und Modifikation von Halbleiternanodrähten*. Diplomarbeit, Universität Göttingen (2005).
- [Sti07] D. Stichtenoth, C. Ronning, T. Niermann, L. Wischmeier, T. Voss, C.-J. Chien, P.-C. Chang, and J. G. Lu. Optical size effects in ultrathin ZnO nanowires. *Nanotechnology* **18**, 435701 (2007).
- [Sti08a] D. Stichtenoth. *Dimensionseffekte in Halbleiternanodrähten*. Dissertation, Universität Göttingen (2008).
- [Sti08b] D. Stichtenoth, K. Wegener, C. Gutsche, I. Regolin, F. J. Tegude, W. Prost, M. Seibt, and C. Ronning. P-type doping of GaAs nanowires. *Applied Physics Letters* **92**, 163107 (2008).
- [Sug10] S. Sugahara and J. Nitta. Spin-Transistor Electronics: An Overview and Outlook. *Proceedings of the IEEE* **98**, 2124 (2010).
- [Tan10] T. Tanaka, K. Tomioka, S. Hara, J. Motohisa, E. Sano, and T. Fukui. Vertical Surrounding Gate Transistors Using Single InAs Nanowires Grown on Si Substrates. *Applied Physics Express* **3**, 025003 (2010).
- [Tri95] H. Trinkaus and A. I. Ryazanov. Viscoelastic Model for the Plastic Flow of Amorphous Solids under Energetic Ion Bombardment. *Physical Review Letters* **74**, 5072 (1995).
- [Tub09] V. Tuboltsev and J. Raisanen. Sculpturing Nanowires with Ion Beams. *Small* **5**, 2687 (2009).
- [Tuo05] F. Tuomisto, K. Saarinen, D. C. Look, and G. C. Farlow. Introduction and recovery of point defects in electron-irradiated ZnO. *Physical Review B* **72**, 085206 (2005).
- [Vos07] T. Voss, G. T. Svacha, E. Mazur, S. Müller, C. Ronning, D. Konjhodzic, and F. Marlow. High-Order Waveguide Modes in ZnO Nanowires. *Nano Letters* **7**, 3675 (2007).
- [Wac09] B. A. Wacaser, K. A. Dick, J. Johansson, M. T. Borgström, K. Deppert, and L. Samuelson. Preferential Interface Nucleation: An Expansion of the VLS Growth Mechanism for Nanowires. *Advanced Materials* **21**, 153 (2009).
- [Wag64] R. S. Wagner and W. C. Ellis. Vapor-liquid-solid mechanism of single crystal growth. *Applied Physics Letters* **4**, 89 (1964).
- [Wan08] D. D. Wang, J. H. Yang, L. L. Yang, Y. J. Zhang, J. H. Lang, and M. Gao. Morphology and photoluminescence properties of ZnO nanostructures fabricated with different given time of Ar. *Crystal Research and Technology* **43**, 1041 (2008).
- [Wan09] Y. Wan, J. Sha, B. Chen, Y. Fang, Z. Wang, and Y. Wang. Nanodevices Based on Silicon Nanowires. *Recent Patents on Nanotechnology* **3**, 1 (2009).
- [Wan11] Y.-B. Wang, L.-F. Wang, H. J. Joyce, Q. Gao, X.-Z. Liao, Y.-W. Mai, H. H. Tan, J. Zou, S. P. Ringer, H.-J. Gao, and C. Jagadish. Super Deformability and Young’s Modulus of GaAs Nanowires. *Advanced Materials* **23**, 1356 (2011).

- [Weh08] R. Wehrspohn. Powered by Nanowires. *Chemistry & Sustainability* **1**, 173 (2008).
- [Wei07] D. Weissenberger, M. Dürschnabel, D. Gerthsen, F. Perez-Willard, A. Reiser, G. M. Prinz, M. Feneberg, K. Thonke, and R. Sauer. Conductivity of single ZnO nanorods after Ga implantation in a focused-ion-beam system. *Applied Physics Letters* **91**, 132110 (2007).
- [Wel97] P. Wellmann, J. Garcia, J.-L. Feng, and P. Petroff. Formation of nanoscale ferromagnetic MnAs crystallites in low-temperature grown GaAs. *Applied Physics Letters* **71**, 2532 (1997).
- [Wen09] E. Wendler, O. Bilani, K. Gärtner, W. Wesch, M. Hayes, F. Auret, K. Lorenz, and E. Alves. Radiation damage in ZnO ion implanted at 15 K. *Nuclear Instruments and Methods in Physics Research B* **267**, 2708 (2009).
- [Wes92] W. Wesch. Ion implantation in III-V compounds. *Nuclear Instruments and Methods in Physics Research B* **68**, 342 (1992).
- [Wha07] S.-J. Whang, S. Lee, D.-Z. Chi, W.-F. Yang, B.-J. Cho, Y.-F. Liew, and D.-L. Kwong. B-doping of vapour-liquid-solid grown Au-catalysed and Al-catalysed Si nanowires: effects of B₂H₆ gas during Si nanowire growth and B-doping by a post-synthesis in situ plasma process. *Nanotechnology* **18**, 275302 (2007).
- [Wil96] D. B. Williams and C. B. Carter. *Transmission electron microscopy: a textbook for materials science*. Plenum Press, New York (1996).
- [Wil09] M. Willander, O. Nur, Q. X. Zhao, L. L. Yang, M. Lorenz, B. Q. Cao, J. Z. Perez, C. Czekalla, G. Zimmermann, M. Grundmann, A. Bakin, A. Behrends, M. Al-Suleiman, A. El-Shaer, A. C. Mofor, B. Postels, A. Waag, N. Boukos, A. Travlos, H. S. Kwack, J. Guinard, and D. L. S. Dang. Zinc oxide nanorod based photonic devices: recent progress in growth, light emitting diodes and lasers. *Nanotechnology* **20**, 332001 (2009).
- [Wit88] A. Witzmann. Experimental Equipment. In G. Götz and K. Gärtner, editors, *High Energy Ion Beam Analysis of Solids*, chapter 2. Akademie-Verlag, Berlin (1988).
- [Wol11] M. Wolff, D. Görlitz, K. Nielsch, M. Messing, and K. Deppert. Synthesis and magnetic characterization of MnAs nanoparticles via nanoparticle conversion. *Nanotechnology* **22**, 055602 (2011).
- [Xie09] P. Xie, Y. Hu, Y. Fang, J. Huang, and C. M. Lieber. Diameter-dependent dopant location in silicon and germanium nanowires. *Proceedings of the National Academy of Sciences of the USA* **106**, 15254 (2009).
- [Yan91] Q. Yang, D. J. O'Connor, and Z. Wang. Empirical formulae for energy loss straggling of ions in matter. *Nuclear Instruments and Methods in Physics Research B* **61**, 149 (1991).
- [Yan08] Y. Yang, X. W. Sun, B. K. Tay, G. F. You, S. T. Tan, and K. L. Teo. A p-n homojunction ZnO nanorod light-emitting diode formed by As ion implantation. *Applied Physics Letters* **93**, 253107 (2008).
- [Yeh09] P.-H. Yeh, Z. Li, and Z. Wang. Schottky-Gated Probe-Free ZnO Nanowire Biosensor. *Advanced Materials* **21**, 4975 (2009).
- [Yon09] I. Yonenaga, Y. Ohno, T. Taishi, and Y. Tokumoto. Recent knowledge of strength and dislocation mobility in wide band-gap semiconductors. *Physica B* **404**, 4999 (2009).
- [Yos57] K. Yosida. Magnetic Properties of Cu-Mn Alloys. *Physical Review* **106**, 893 (1957).
- [Yu08] G. Yu, X. Li, C. M. Lieber, and A. Cao. Nanomaterial-incorporated blown bubble films for large-area, aligned nanostructures. *Journal of Materials Chemistry* **18**, 728 (2008).

- [Yua93] B. Yuan, F. Yu, and S. Tang. A database method for binary atomic scattering angle calculation. *Nuclear Instruments and Methods in Physics Research B* **83**, 413 (1993).
- [Zha00] J. Zhan, X. Yang, S. Li, D. Wang, Y. Xie, and Y. Qian. A chemical solution transport mechanism for one-dimensional growth of CdS nanowires. *Journal of Crystal Growth* **220**, 231 (2000).
- [Zha09] Z. H. Zhang, X. Wang, J. Xu, S. Müller, C. Ronning, and Q. Li. Evidence of intrinsic ferromagnetism in individual dilute magnetic semiconducting nanostructures. *Nature Nanotechnology* **4**, 523 (2009).
- [Zie85] J. F. Ziegler, J. P. Biersack, and U. Littmark. *Stopping and Range of Ions in Solids*. Pergamon, New York (1985). ISBN 0-08-021603-X.
- [Zie92] J. F. Ziegler, editor. *Handbook of Ion Beam Implantation Technology*. North-Holland, Amsterdam, London, New York (1992). ISBN 0-444-89735-6.
- [Zie11] J. F. Ziegler, J. P. Biersack, and U. Littmark. <http://www.srim.org> (2011).
- [Zim08] M. A. Zimmler, J. Bao, F. Capasso, S. Müller, and C. Ronning. Laser action in nanowires: Observation of the transition from amplified spontaneous emission to laser oscillation. *Applied Physics Letters* **93**, 051101 (2008).
- [Zim10] M. A. Zimmler, S. Müller, C. Ronning, and F. Capasso. Optically pumped nanowire lasers: invited review. *Semiconductor Science and Technology* **25**, 024001 (2010).
- [Zol07] G. Zollo and F. Gala. Stability of I_3 complexes in III-V compound semiconductors by tight-binding molecular dynamics. *Physical Review B* **75**, 115205 (2007).

Appendix A

List of Publications

Publications directly related to this thesis

Alignment of Semiconductor Nanowires Using Ion Beams

C. Borschel, R. Niepelt, S. Geburt, Ch. Gutsche, I. Regolin, W. Prost, F.-J. Tegude, D. Stichtenoth, D. Schwen and C. Ronning
SMALL **5**, 2576–2580, (2009)

Tailoring the properties of semiconductor nanowires using ion beams

C. Ronning, **C. Borschel**, S. Geburt, R. Niepelt, S. Müller, D. Stichtenoth, J.-P. Richters, A. Dev, T. Voss, L. Chen, W. Heimbrod, Ch. Gutsche and W. Prost
PHYSICA STATUS SOLIDI B **247**, 2329, (2010)

Ion beam doping of semiconductor nanowires

C. Ronning, **C. Borschel**, S. Geburt and R. Niepelt
MATERIAL SCIENCE AND ENGINEERING R **70**, 30, (2010)

Permanent Bending of ZnO Nanowires

C. Borschel, S. Spindler, D. Lerose, A. Bochmann, S. H. Christiansen, S. Nietzsche, M. Oertel and C. Ronning
NANOTECHNOLOGY **22**, 185307, (2011)

Ion beam irradiation of nanostructures - A 3D Monte Carlo simulation code

C. Borschel and C. Ronning
NUCLEAR INSTRUMENTS AND METHODS B **269**, 2133, (2011)

A New Route toward Semiconductor Nanospintronics: Highly Mn-Doped GaAs Nanowires Realized by Ion-Implantation under Dynamic Annealing Conditions

C. Borschel, M. E. Messing, M. T. Borgström, W. Paschoal Jr., J. Wallentin, S. Kumar, K. Mergenthaler, K. Deppert, C. M. Canali, H. Pettersson, L. Samuelson, and C. Ronning
NANO LETTERS **11**, 3935, (2011)

Other publications

Magnetic coupling in Gd/Ni bilayers

A. Barth, F. Treubel, M. Marszalek, W. Evenson, O. Hellwig, **C. Borschel**, M. Albrecht and G. Schatz

JOURNAL OF PHYSICS: CONDENSED MATTER **20**, 395232 (6pp), (2008)

Structure and defects of epitaxial Si(111) layers on Y₂O₃(111)/Si(111) support systems

C. Borschel, C. Ronning, H. Hofsäss, A. Giussani, P. Zaumseil, Ch. Wenger, P. Storck, and T. Schroeder

JOURNAL OF VACUUM SCIENCE AND TECHNOLOGY B **27**, 305, (2009)

Simulation and Fitting of High Resolution RBS spectra

C. Borschel, M. Schnell, C. Ronning, and H. Hofsäss

NUCLEAR INSTRUMENTS AND METHODS B **267**, 1737-1739, (2009)

Influence of metallic coatings on the photoluminescence properties of ZnO nanowires

J.-P. Richters, A. Dev, S. Müller, R. Niepelt, **C. Borschel**, C. Ronning, and T. Voss

PHYSICA STATUS SOLIDI - RAPID RESEARCH LETTERS **3**, 166-168, (2009)

Phase diagram of Si nanowire growth by disproportionation of SiO

W. Dewald, **C. Borschel**, D. Stichtenoth, T. Niermann and C. Ronning

JOURNAL OF CRYSTAL GROWTH AND DESIGN **312**, 1751–1754, (2010)

Self-organized nanostructuring of composite coatings at high temperatures for drag reduction and self-cleaning

P. Schaaf, S. Günschmann, M. Hopfeld, J. Wilden, V. Drescher, **C. Borschel** and C. Ronning

THIN SOLID FILMS **205**, 1584, (2010)

Hexagonal Boron Nitride Nanowalls Synthesized by Unbalanced RF Magnetron Sputtering

B. BenMoussa, J. D'Haen, **C. Borschel**, M. Saitner, A. Soltani, V. Mortet, C. Ronning, M. D'Olieslaeger, H.-G. Boyen and K. Haenen

MRS PROCEEDINGS **1307**, mrsf10-1307-cc06-09, (2011)

Composition and texture of barium silicate crystals in fresnoite glass-ceramics by various scanning electron microscopic techniques

M. Nagel, W. Wisniewski, G. Völksch, **C. Borschel**, C. Ronning and C. Rüssel

CRYSTENGCOMM **13**, 3383, (2011)

Strong Molecular Fluorescence inside a Nanoscale Waveguide Gap

V. Sorger, O. Pholchai, E. Cubukcu, R. Oulton, P. Kolchin, **C. Borschel**, M. Gnauck, C. Ronning, X. Zhang

NANO LETTERS, **11**, 4907, (2011)

Appendix B

Details Regarding The MC Simulations

B.1 The database method for scattering angles

Tables (the “database”) of precalculated scattering angles θ_{CM} (CM : center-of-mass system) can be used to avoid the lengthy calculation of the scattering angles during the simulation. *Iradina* uses the data base from *corteo*, details in [Sch07]. The basic table does not store θ_{CM} itself, but rather $\sin^2(\theta_{CM}/2)$, because this value is required in the calculations. The two dimensional table contains values as a function of reduced energy $\varepsilon = E \cdot a / (Z_1 Z_2 e^2)$ and of reduced impact parameter $b = p/a$, with E : energy in center-of-mass system, Z_1, Z_2 : proton numbers of projectile and target, p : impact parameter, $a = 0.8853 \cdot a_0 / (Z_1^{0.23} + Z_2^{0.23})$: screening length, and a_0 : Bohr radius. These reduced quantities allow to use one general table independent of projectile and target masses.

It is useful to scale the table logarithmically in order to cover a large range of ε and b without making the table too large. This requires calculating the logarithms of ε and b whenever the table is accessed. The calculation of a logarithm takes a lot of time compared to other operations or memory access. In order to avoid this calculation, a neat indexing mechanism was proposed by Yuan *et al.* [Yua93] and improved by Schiettekatte [Sch07]: computers represent non-integer numbers in an exponential form anyway; thus, a good approximation of the dual logarithm can directly be extracted from the 32 bits of a floating point number. The *corteo* database uses the 8 exponent bits plus the first four mantissa bits as the index to access entries in the table, for details see [Sch07].

Using just the basic table with values for $\sin^2(\theta_{CM}/2)$ still requires conversion to the laboratory frame of reference, which involves several calculations of trigonometric functions. This can be avoided if sufficient memory is available: On startup, the program creates tables of $\sin(\theta)$ and $\cos(\theta)$ as a function ε and b for each possible combination of projectile and target nucleus (≈ 2.6 MByte per combination). These calculations take up a few seconds on startup, but then the calculations of trigonometric functions can almost be completely avoided during simulation, regardless of the numbers of projectiles to simulate.

It may be noted that this database methods is useful because the required amounts of memory are easily available on every computer nowadays (typical simulations shown in this thesis required up to about 100 MByte). This is in contrast to the earlier days of simulating ion implantation in the 1980’s, when memory was far more expensive and the MAGIC algorithm was a great achievement to save computing time.

Naturally, approximation errors occur when accessing a table with a limited number of entries. According to [Sch07] the accuracy of the database is within 5%. The MAGIC algorithm is implemented in *iradina* as well for comparison. No deviations were observed when comparing implantation profiles calculated with the database and the MAGIC algorithm. Figure B.1 compares values for $\sin^2(\theta_{CM}/2)$ calculated with MAGIC and the database for different ε and b .

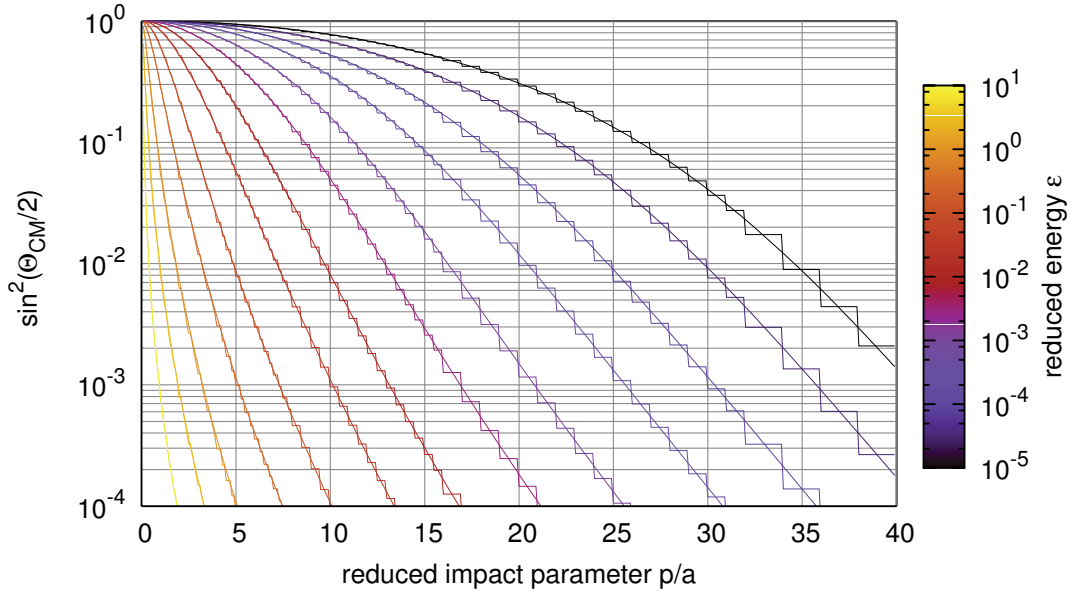


Figure B.1: Comparison of the database method (adapted from *corteo* [Sch08]) to the MAGIC formula [Bie80], both for the universal potential. $\sin^2(\theta_{CM}/2)$ is shown as a function of the reduced impact parameter p/a for different reduced energies ϵ (color-coded). The smooth lines are calculated using the MAGIC algorithm, the “stepped” lines are calculated using *corteo*’s database method. Compare with [Zie85, p.59]. The calculations were done using the implementations in the *iradina* code for both algorithms.

The approximation errors become visible as “steps”, but are distributed to both sides and are thus assumed to average out.

B.2 Computing flow of ion transport

The computing flow of the transport function is illustrated schematically in figure B.2. Note, that the current implementation of *iradina* varies a little: The fractional calculations of stopping are not performed for the sake of simplicity and computation time. Since flight paths are chosen to be short (no long extended flight lengths as in TRIM), this is a good approximation. Note that collision partners are searched for in multiple cylinders of different radii. This is important to calculate sputtering accurately, because a projectile flying in vacuum may interact with surface atoms not being within in the first cylinder of radius p_{max} . For details, see [Eck91, p.92ff].

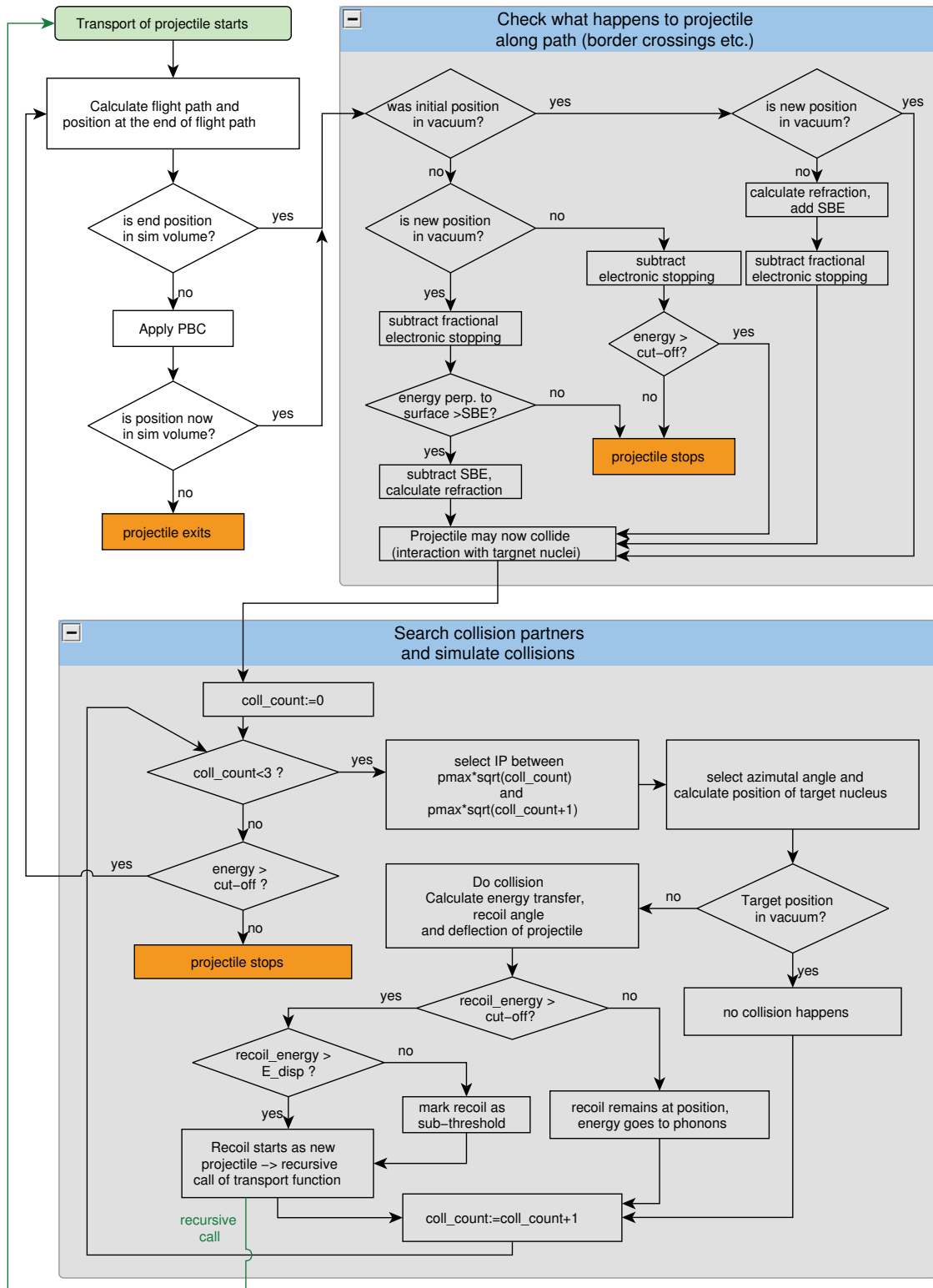


Figure B.2: Simplified illustration of computing flow of the transport function. PBC: periodic boundary conditions, SBE: Surface binding energy, Coll_count: Collision counter.

B.3 Additional comparisons between *iradina* and TRIM

The implantation of different elements (atomic masses 1, 6, 107, 207) into bulk Si with different energies was simulated with *iradina* and TRIM. For *iradina* simulations, the full transport algorithm was used, not the simplified fast one. TRIM simulations were done with program version SRIM 2008.03 and the mode “Detailed Calculation with Full Damage Cascades” was selected (except for high energy hydrogen, where “Monolayer collision steps” were used to avoid anomalous peaks, as recommended by SRIM manual). Figure B.3 shows the resulting depth distributions of implanted ions for *iradina* and TRIM. They are mostly in good agreement. Small deviations occur for hydrogen ions.

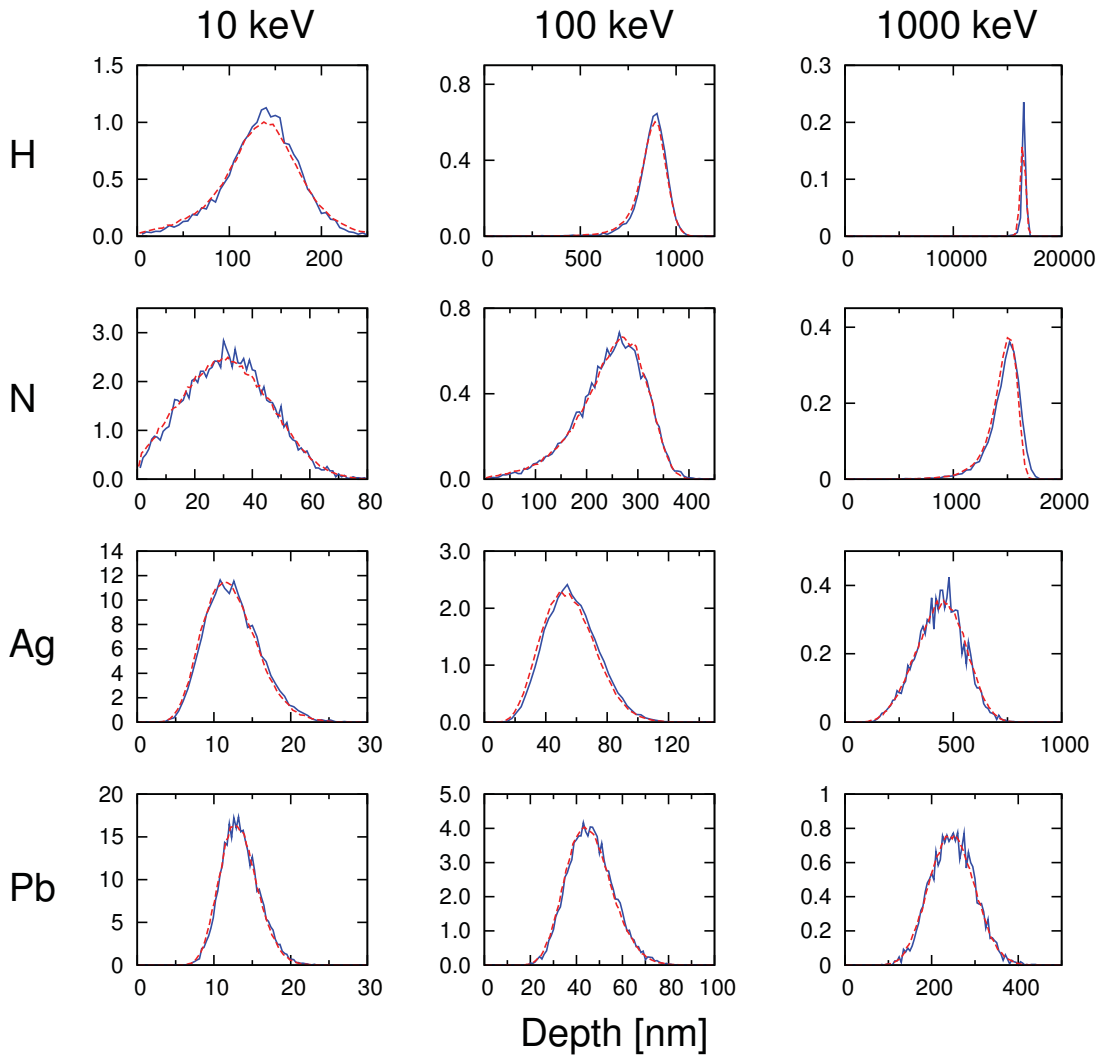


Figure B.3: Comparison of simulation results from *iradina* (--) and TRIM (—). The depth distribution of different elements implanted into bulk Si at perpendicular incidence with different energies is shown in units of $10^5/\text{cm}^3$ per ions/ cm^2 .

B.4 Distribution of single ion sputter yields

Figure B.4 shows the distribution of the number of sputtered target atoms per each individual ion for different sizes of Au nanoparticles. Simulations were done with *iradina*; Ga ions with 25 keV were used. The number of sputtered particles per ion scatters greatly for individual ion impacts.

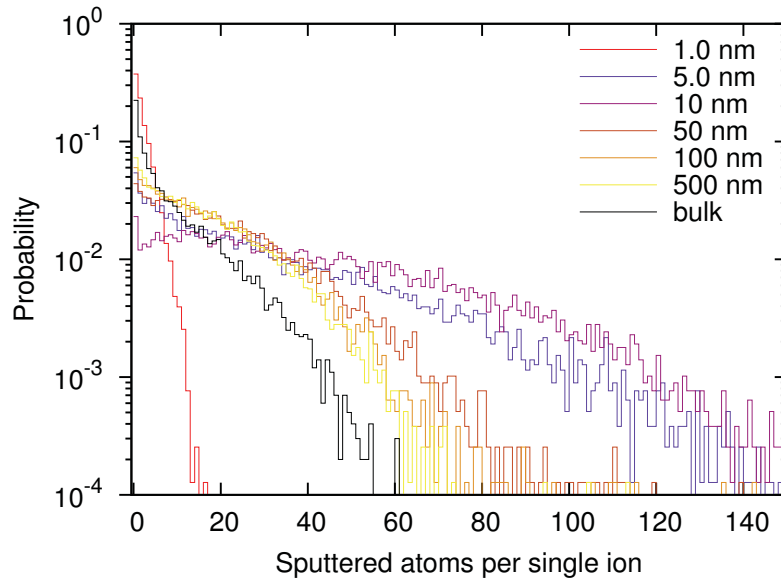


Figure B.4: *Distribution of the number of sputtered atoms per incoming ion for different NP diameters as noted in the figure key.*

Appendix C

Details for the dynamic bending calculation

Derivation of the conditions for minimum strain energy of a segment

By basic geometrical considerations, one finds that the total strain energy E_s of a segment s can be expressed by

$$E_s = \sum_{j,k} Y_{jk}^c \cdot (l_s^m - l_{sjk}^r - j \cdot \Delta x \cdot \tan \alpha_s - k \cdot \Delta y \cdot \tan \beta_s)^2.$$

Necessary condition for minimum energy is that the partial derivatives of E_s with respect to l_s^m , α_s and β_s vanish, from which the three equations (4.1) follow:

$$\begin{aligned} 0 &\stackrel{!}{=} \frac{\partial E_s}{\partial l_s^m} = \sum_{j,k} 2 \cdot Y_{jk}^c \cdot (l_s^m - l_{sjk}^r - j \cdot \Delta x \cdot \tan \alpha_s - k \cdot \Delta y \cdot \tan \beta_s) \\ 0 &\stackrel{!}{=} \frac{\partial E_s}{\partial \alpha_s} = \sum_{j,k} 2 \cdot Y_{jk}^c \cdot (l_s^m - l_{sjk}^r - j \cdot \Delta x \cdot \tan \alpha_s - k \cdot \Delta y \cdot \tan \beta_s) \cdot j \cdot \Delta x \cdot (1 + \tan^2 \alpha_s) \end{aligned}$$

Since $(1 + \tan^2 \alpha_s) > 0$ for all α_s

$$\Rightarrow 0 \stackrel{!}{=} \sum_{j,k} Y_{jk}^c \cdot (l_s^m - l_{sjk}^r - j \cdot \Delta x \cdot \tan \alpha_s - k \cdot \Delta y \cdot \tan \beta_s) \cdot j.$$

(C.1)

The derivative with respect to β_s is similar to the one with respect to α_s .

Although these conditions are not sufficient for minimum energy, it is unlikely that the global minimum is not found, because the functions are approximately linear for not too large angles.

Newton's method

Newton's method can be used to solve a set of equations $\underline{f}(\underline{x}) = 0$ numerically [Got95, p.695]. An initial solution \underline{x}_0 is guessed and then improved iteratively using the following recursive formula:

$$\underline{x}_{n+1} = \underline{x}_n - \underline{\underline{J}}_f^{-1}(\underline{x}_n) \cdot \underline{f}(\underline{x}_n)$$

where $\underline{\underline{J}}_f^{-1}$ is the inverse Jacobi matrix of \underline{f} .

For the case of equations (4.1), the solution vector has three components: $\underline{x}_n = (l_n^m, \alpha_n, \beta_n)$.

The initial guess uses the old segment length (from the last irradiation step) and vanishing tilt angles (horizontal end-plane). The Jacobi matrix of \underline{f} is

$$\underline{\underline{J}} = \underset{j,k}{Y_{jk}^c} \cdot \begin{pmatrix} 1 & -j \cdot \Delta x \cdot (1 + \tan^2 \alpha_s) & -k \cdot \Delta y \cdot (1 + \tan^2 \beta_s) \\ j & -j^2 \cdot \Delta x \cdot (1 + \tan^2 \alpha_s) & -j \cdot k \cdot \Delta y \cdot (1 + \tan^2 \beta_s) \\ k & -j \cdot k \cdot \Delta x \cdot (1 + \tan^2 \alpha_s) & -k^2 \cdot \Delta y \cdot (1 + \tan^2 \beta_s) \end{pmatrix}.$$

The required matrix inversion is performed numerically by Gauss-Jordan elimination [Got95, p.681]. This inversion method is slow [complexity $\mathcal{O}(n^3)$] but it is relatively simple to implement and fast enough for inverting a 3×3 matrix.

Usually, a good solution is found quickly after a few iteration steps, where a “good” solution means: $\frac{\alpha_{n+1} - \alpha_n}{\alpha_n} < 10^{-7}$. The reason for the quick convergence in this case is that the system is approximately linear for small angles α_s and β_s .

When a nanowire is irradiated from one side, it should be sufficient for the calculation to use only one bending angle α . Nevertheless, β was included in the implementation to conserve generality, but the calculations show that β remains practically 0 during bending.

Formation volumes of defects

Defects in ZnO

Erhart *et al.* performed first-principle studies of intrinsic defects in ZnO using density functional theory (DFT) calculations [Erh06]. Apart from transition levels and formation enthalpies, their calculations also allow to determine formation volumes. Since only small volumes with up to about 100 atoms were possible to simulate, the formation volumes had to be extrapolated to obtain bulk values. Their results are listed in table C.1. For illustration of the various defect types, see [Erh05].

The transition levels of the various defect types are illustrated in figure C.1. The charge states of the defects can be determined, depending on the position of the Fermi energy level.

Table C.1: Formation volumes of different intrinsic point defects in ZnO, values taken from [Erh06], units are relative volumes with respect for ZnO formula unit. int: interstitial, vac: vacancy, oct: on octahedral site, db: dumbbell interstitial, db-rot: rotated dumbbell interstitial

Defect type	charge state				
	-2	-1	0	+1	+2
Zn int,oct			0.81	0.28	-0.30
O vac			-0.26	-0.18	-0.32
O int,db			0.47	0.13	-0.26
O int,db-rot	1.15	0.76	0.43	0.08	-0.32
O int,oct	1.05	0.68	0.33	-0.05	-0.46
Zn vac	0.81	0.45	0.05		

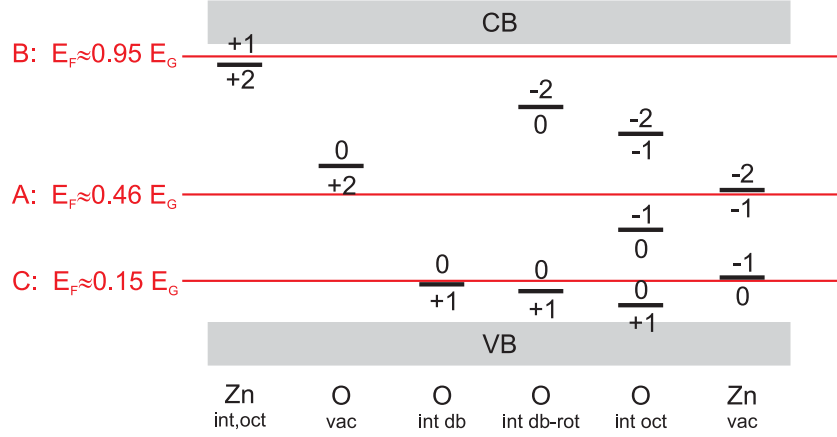


Figure C.1: Illustration of transition levels of the intrinsic defects of ZnO within its band gap, data taken from [Erh06]. The charge state of the defects depends on the Fermi level; the three energy levels used in this work are shown.

Defects in GaAs

No values for the formation volumes of intrinsic defects in GaAs were found in the literature. Reported measurements of positron annihilation times yield the open volumes of defects but not the formation volumes. Several ab-initio studies of intrinsic defects in GaAs with different methods (tight-binding, density-functional theory) are reported; however, they do not report formation volumes, but they do report the relaxation of bond-lengths or of tetraeder volumes V_{tetra} , which can be used as a rough measure for the volume expansion or reduction ΔV caused by defects. The dependence on charge state is less pronounced compared to ZnO, because GaAs is less ionic. In cases where the volume depends on charge states, the charge states were selected for a Fermi energy approximately in the middle of the band gap (see [Sch09a]). The values used for the dynamic bending calculation in section 4.6.5 are listed in table C.2. It should be noted that somewhat contradicting values were found for the As_{Ga} antisite, see [Sta01, Seo95] and that defect complexes are ignored [Zol07].

Table C.2: Relative and absolute expansion or reduction of tetraeder volume around various intrinsic defects in GaAs. *int:* interstitials, *vac:* vacancy

Defect type	$\Delta V/V_{\text{tetra}}$	$\Delta V [\text{\AA}^3]$	Source
Ga int	33%	2.4	calculated from average bond length increase for different types of Ga ints [Mal07], charge state 0
Ga vac	-34%	-2.5	from [Seo95], charge state -2
As int	15%	1.1	twice as much as As_{Ga} antisite [Sta01]
As vac	19%	1.4	from [Seo95], charge state -1
Ga_{As} antisite	5.5%	0.41	from [Seo95], charge state -1
As_{Ga} antisite	7.8%	0.56	from [Seo95], charge state 0

Danksagung

Als erstes bedanke ich mich bei Carsten Ronning für die hervorragende Betreuung meiner Doktorarbeit, viele spannende Diskussionen, Lehre, die Freiräume eigene Ideen umzusetzen, die vielen Möglichkeiten auswärts zu arbeiten (insbesondere Lund und Harvard!), die lockere Arbeitsatmosphäre, ein stets offenes Ohr für alles mögliche, Motivation zu interessanten Projekten, viele (internationale) Konferenzbesuche, die Einbindung in die zukünftige Forschergruppe, und nicht zuletzt die legendären Semesterabschlusspartys.

Meinen Kollegen danke ich für die tolle Zusammenarbeit, viele anregende Diskussion, gemeinsame Experimente, eine tolle Arbeitsgruppenatmosphäre aber auch viel Spaß außerhalb der Physik, wobei ein besonderer Dank meinen langjährigen “Büromitbewohnern” Jana Sommerfeld, Raphael Niepelt und Sebastian Geburt gebührt!

Weiterhin danke ich den Diplomanden, Bachelorstudenten, Studienarbeitern und Praktikanten, die ich mit betreuen durfte und die somit direkt oder indirekt auch zum Gelingen dieser Arbeit beigetragen haben: Michael Kozlik, Amanda McDonnell, Julian Kühnel, Moritz Laubscher, Anne Nathanael und ganz besonders Susann Spindler für Ihre hervorragenden Experimente zur Verbiegung von ZnO-Nanodrähten und die tolle Zusammenarbeit!

Weiterhin danke ich auch allen anderen Mitgliedern der “Nanogruppe” am IFK für die schöne Zusammenarbeit, viele lustige Grillabende, gemeinsame Lauf-Wettkämpfe, Stickstoffeis, Poolpartys und “Störstellen”; unter Anderem danke ich dafür Martin Gnauck, Steffen Milz, Maria Fravventura, Gabriele Bulgarini, Jessica Hönig, Ulrich Schröder, Yaser Haj Hmeidi, Christian Müller, Stefan Weidner, Andreas Johannes, Andreas Thielmann, Franziska Riedel, Irma Slowik, Henry Holland-Moritz, Davide Cammi und Robert Röder.

Für weitere tolle Zusammenarbeit im Institut, Diskussionen und gemeinsame Frühstücksrunden bedanke ich mich unter Anderem bei Werner Wesch, Jacob Haarstrich, Matthias Hädrich, Jura Rendsberg, Christoph Heisler, Christian Kraft, Michael Oertel, Elke Wendler und Claudia Schnohr.

Herrn Wolfhard Möller aus Rossendorf danke ich für eine Einladung zum HZDR, für sehr aufschlussreiche und interessante Diskussionen über Monte-Carlo-Simulationen von Ionenbestrahlung und für die Bereitschaft meine Arbeit zu begutachten!

Weiterhin möchte ich mich bei den vielen Kollaborationspartnern bedanken, mit denen es sehr viel Spaß gemacht hat zusammen zu arbeiten und zu diskutieren: Martin Seyring, Jürgen Hempel und Markus Rettenmayer vom IMT in Jena danke ich für Hilfe beim TEM und für die Zusammenarbeit an Ni-katalysierten Si-NW. Bei Marcus Nagel und Günter Völksch vom Otto-Schott-Institut aus Jena bedanke ich mich für die Zusammenarbeit an Fresnoit-Glas-Keramiken. Für den Zugang und Hilfe zum FIB des IPHT (Jena) danke ich Damiana Lerose, Arne Bochmann und Silke Christiansen. Weiterhin bedanke ich mich bei Sabine Günschmann und Peter Schaaf von der TU Ilmenau für die Zusammenarbeit über nanostrukturierte Komposit-Beschichtungen. Christoph Gutsche und Werner Prost aus Duisburg danke ich für die tolle Zusammenarbeit bei der Ionenbestrahlung von GaAs-Nanodrähten und mehrere sehr lustige Abende in Duisburg und Jena. Holger von Wenckstern aus Leipzig danke ich für die Zusammenarbeit über ionenstrahl-dotiertes ZnO. Bei Wilma Dewald aus Göttin-

gen (dann Braunschweig) bedanke ich mich für die Zusammenarbeit über das Wachstum von Si-Nanodrähten. Daniel Stichtenoth aus Göttingen (dann Erfurt) danke ich für die Kollaboration über Bestrahlung von GaAs-NW. Bei Sven Müller und Hans Hofsäss aus Göttingen bedanke ich mich für diverse Implantationen, wenn der Beschleuniger in Jena mal nicht funktionierte. Weiterhin danke ich Herrn Hofsäss auch für die Einführung in die Physik der Ionen-Festkörper-Wechselwirkung und eine spannende Diplomarbeitszeit, die eine gute Vorbereitung zur Doktorarbeit war! Weiterhin danke ich Jan-Peter Richters und Tobias Voss aus Bremen für die Zusammenarbeit über den Einfluss der Oberflächenbeschichtung auf ZnO-Nanodrähte. Bei Thomas Schröder, Christian Wenger und Alessandro Giussani aus Frankfurt(Oder) (und dann Berlin) bedanke ich mich für die Zusammenarbeit über epitaktische Schichtsysteme und mehrere Einladungen nach Frankfurt(Oder). Alois Lugstein aus Wien danke ich für die Zusammenarbeit an Si-Nanodrähten. Bei Boumediene Benmoussa aus Hasselt bedanke ich mich für die Kollaboration über hBN-nanowalls. Für die interessante Zusammenarbeit über hoch Mn-dotierte GaAs-Nanodrähte bedanke ich mich bei Håkan Petterson aus Halmstadt, Maria Messing, Waldomiro Paschoal, Sandeep Kumar, Knut Deppert, Magnus Borgström, Kilian Mergenthaler, Jesper Wallentin und Lars Samuelson aus Lund und Carlo Canali aus Kalmar. Weiterhin danke ich Maria für Einladung zur tollen PhD-Party sowie Carlo für die Einladung zum Nanospintronics-Workshop nach Enköping. Kristen Sunter und Federico Capasso aus Harvard danke ich für die Zusammenarbeit über CdS-Nanodrähte und zwei spannende Monate in Cambridge (MA). Bei Daniel Schwen aus Illinois bedanke ich mich für Simulationen von Ionenbestrahlung von Nanodrähten und Diskussion über deren Verbiegung. Ertugrul Cubukcu, Volker Sorger und Rupert Oulton aus Berkeley (dann London) danke ich für die Zusammenarbeit über nanoskalige Wellenleiter.

Für allerlei Hilfe bei technischen Fragen und Problemen, sowie eine große Anzahl schneller Ionen, verflüssigte Gase, Computerprogramme und reparierte PCs danke ich Uta Bornkessel, Frank Jehn, Ulli Barth, Gerald Lenk, Lutz Föllmer, Carmen Voigt und Ralf Neubert sowie den Mechanik- und Elektrowerkstätten der PAF. Für die kompetente Hilfe bei allen verwaltungstechnischen Fragen danke ich Anja Mittelstädt und Uta Bornkessel.

Die Arbeit an der Doktorarbeit hätte kaum so viel Spaß gemacht, wenn es nicht auch die nötige Abwechslung dazu gegeben hätte in Form von Wandern, Laufen, Skilaufen, Klettern, Tanzen, Grillen, Kartenspielen . . . , wofür ich mich an dieser Stelle bei meinen Freunden aus Hamburg, Göttingen, Jena und anderen Orten bedanken möchte: Alex, Andreas, Anna-Lena, Anne, Bene, David, Dilei, Dirk, Franzi, Georg, Jacob, Janina, Johannes, Jochen, Jolle, Karin, Karsten, Kathi, Kristin, Kristina, Mark, Markus, Martin, Martin, Myriam, Patrick, Rudolf, Sören, Steffi, Swante und Tim.

Schließlich bedanke ich mich bei meiner Familie für die stetige Unterstützung. Besonders möchte ich meinem Großvater danken: Vielen Dank, dass Du mich zur Physik motiviert hast, und dass Du Dich immer für mein Studium und die Arbeit begeistern konntest, obwohl das “Astro” vor der “Physik” fehlt. Und ganz besonders danke ich meinen Eltern: Vielen Dank für . . . einfach alles! Ohne Euch wäre ich bestimmt nicht bis hierher gekommen!

Ehrenwörtliche Erklärung

Ich erkläre hiermit ehrenwörtlich, dass ich die vorliegende Arbeit selbstständig, ohne unzulässige Hilfe Dritter und ohne Benutzung anderer als der angegebenen Hilfsmittel und Literatur angefertigt habe. Die aus anderen Quellen direkt oder indirekt übernommenen Daten und Konzepte sind unter Angabe der Quelle gekennzeichnet.

Bei der Auswahl und Auswertung folgenden Materials haben mir die nachstehend aufgeführten Personen in der jeweils beschriebenen Weise unentgeltlich geholfen:

1. Bei der Auswertung der Daten zur Verbiegung der GaAs-Nanodraht-Ensembles haben mir Raphael Niepelt und Sebastian Geburt geholfen.
2. Die Bestrahlungsexperimente zur Verbiegung einzelner GaAs-Nanodrähte im FIB wurden zusammen mit Damiana Lerosé durchgeführt.
3. Die Verbiegungsexperimente an ZnO-Nanodrähten und die Auswertung der Daten erfolgte gemeinsam mit Susann Spindler.
4. Einige TEM-Aufnahmen der Mn-dotierten GaAs-Nanodrähte wurden von Maria Messing in Lund angefertigt. Die Auswertung der Kristallstruktur geschah in Zusammenarbeit mit Maria Messing.
5. Die elektrischen und Magnetotransport-Messungen an Mn-dotierten GaAs-Nanodrähten wurden von Waldomiro Paschoal Jr. und Sandeep Kumar in Lund durchgeführt. Die Interpretation erfolgte weiterhin in Zusammenarbeit mit Håkan Pettersson und Carlo Canali.
6. Im Übrigen waren jeweils die Koautoren der angeführten Veröffentlichungen (siehe Anhang A) an der Interpretation der Ergebnisse beteiligt.

Weitere Personen waren an der inhaltlich-materiellen Erstellung der vorliegenden Arbeit nicht beteiligt. Insbesondere habe ich hierfür nicht die entgeltliche Hilfe von Vermittlungs- bzw. Beratungsdiensten (Promotionsberater oder andere Personen) in Anspruch genommen. Niemand hat von mir unmittelbar oder mittelbar geldwerte Leistungen für Arbeiten erhalten, die im Zusammenhang mit dem Inhalt der vorgelegten Dissertation stehen.

Die Arbeit wurde bisher weder im In- noch im Ausland in gleicher oder ähnlicher Form einer anderen Prüfungsbehörde vorgelegt.

Die geltende Promotionsordnung der Physikalisch-Astronomischen Fakultät ist mir bekannt.

Ich versichere ehrenwörtlich, dass ich nach bestem Wissen die reine Wahrheit gesagt und nichts verschwiegen habe.

Jena